Politecnico di Milano
Dipartimento di Energia
Doctoral Program in
Energy and Nuclear Science and Technology

Advances in Target Normal Sheath Acceleration with traditional and nanostructured targets

Doctoral Dissertation of:
Lorenzo Cialfi

Supervisors:
Prof. Matteo Passoni, Dr. Luca Fedeli

Tutor:
Prof. Lelio Luzzi

The Chair of the Doctoral Program:
Prof. Carlo Enrico Bottani

Year 2017 – Cycle XXIX

A Giulia

Abstract

The development of high power laser facilities disclosed new research opportunities. Among the potential fields, laser-based accelerators stand out due to appealing features such as compactness and cheapness with respect to traditional ones. In this PhD work we dedicated our study to the promising ion acceleration technique represented by Target Normal Sheath Acceleration (TNSA) which has been suggested for applications such as: radiotherapy, isotopes production, fusion fast ignition schemes and proton imaging. However, much improvements are still needed in order to gain a more robust mastery of the technique. A proper knowledge of the influence of the many experimental parameters on TNSA can arguably disclose the most efficient operating conditions as well as outline strategies to further evolve the technique. In particular, laser-induced electron heating is on of the fundamental physical processes which ultimately determines TNSA. Despite its acknowledged importance, at the state of the art it is much unexplored, also due to the complex physics involved.

This PhD thesis is aimed at acquiring a greater insight of TNSA, with a particular interest on the laser-plasma coupling that drives ion acceleration. The first part of this work dedicated on the data analysis of two recent experimental campaigns, carried out in collaboration with the GIST institute (South Korea), which allowed to understand the role of important experimental parameters on TNSA with both traditional flat foils and novel multi-layered targets. The experimental conditions analyzed also represented the core of our theoretical and numerical investigation.

In order to understand the physics of laser induced electron heating, we

provided simple theoretical model in order to predict the hot electron temperature resulting from the interaction of an ultra-intense (I>$10^{18} W/\text{cm}^2$), ultra-short (tens of fs) laser pulse with a flat micrometric target, usually adopted in TNSA experiments. This study will be also extended to the case of novel multi-layered targets which have recently proposed to achieve an evolution of the acceleration technique. The analytical work is supported by dedicated numerical simulations which represent a powerful tool to investigate the rich physical system. Our results are then combined with an existing model for TNSA to offer an evolution to the latter. At this point the theoretical predictions will be tested against the ample experimental data we analyzed in the first part of this PhD.

Contents

Introduction

THe advent of laser technology marked a crucial milestone in science, providing a reliable source of monochromatic, coherent radiation which proved to be an essential tool in a wide range of applications. The development of Q-switch and Mode-locking allowed to deliver the laser energy through short pulses, down to femtosecond durations with Ti:Sapphire lasers, characterized by high peak intensities that could exceed $10^{10} W/\mathrm{cm}^2$. Around 1970 the increase in performances significantly slowed down. Indeed, large amplifications volumes were required in order to avoid damages in the gain mediums. In 1985 the development of Chirped Pulse Amplification allowed to overcome this limitation and marked the advent of Terawatt and, later, Petawatt facilities worldwide. Such laser systems provide sources of electromagnetic pulses, characterized by durations spacing from few femtoseconds to picoseconds, focal spots of few $\mu\mathrm{m}^2$ which deliver energies from few mJs to hundreds of J. As a result, these lasers can reach powers up to PW and peak intensities greater than $10^{20} W/\mathrm{cm}^2$. These pulses are associated to intense electromagnetic fields ($\sim 10^{10}$ V/cm) which boost electrons up to relativistic energies. In this scenario a material irradiated by such beams is promptly ionized in the first laser cycles, turning into plasma state. Ultra-intense laser-plasma interaction, characterized by a collection of relativistic and non linear effects, not only represent a challenging and novel branch of physics but it is also of utmost interest for its appealing potential applications. Indeed, TW/PW laser systems can be exploited to provide compact sources of secondary radiation. In the last decades, laser-plasma interaction was exploited to produce bunches of energetic electrons (up to GeVs) as well as bursts of x and γ rays. Moreover, laser-based ion accelerators proved to be reliable sources of highly collimated, multi-MeV particles. These accelerators can also be used as an indirect source of pulsed neutron beams through induced nuclear reactions such as (γ, n) and (p,n). Besides, ultra-intense laser plasma interaction can also be exploited to reproduce in controlled tabletop experiments physical conditions similar (in terms of pressures, densities and temperatures) to those of astrophysical objects, providing an essential tool to test theoretical predictions.

Among the above described applications, in the present PhD work the specific case of laser-driven ion acceleration is considered. This topic acquired a significant interest in early 2000s due to three independent works which measured multi-MeV protons after the interaction of short ($\sim$ ps) intense ($> 10^{18} W/\mathrm{cm}^2$) pulses with micrometric thick foils (SLT). Energetic ions were measured in the direction normal to the target and were characterized by low divergence ($\leq 20°$), ps beam duration, high number of particles per bunch ($\sim 10^{13}$) and a thermal spectrum with a high energy cutoff. Such accelerators could provide compact and potentially cheaper (with respect to traditional ones) sources of energetic ions which can find application in radiotherapy, isotopes production, high resolution imaging, electromagnetic field probing, material investigation and fast ignition inertial fusion.

At the state of the art the so-called Target Normal Sheath Acceleration (TNSA) mechanism is able to interpret most of experimental measurements. In TNSA an ultra-intense laser irradiates a micrometric target, the electromagnetic wave couples with the electrons, heating them to relativistic energies. These expand into the target due to their strong thermal pressure and a charge separation is generated at the target surfaces. A strong electrostatic field (up to TV/m), perpendicular to the solid-vacuum interface, is set up and accelerates ions along its direction. In this framework the most efficiently accelerated ions are protons or light ions coming from the hydrocarbon impurities usually present at the surfaces. However, heavier ions as well as bulk ones can also be accelerated to relevant energies.

Despite its appealing features, a much more robust control over TNSA is still required for most of the above described applications. One example is the broad spectrum of accelerated ions which is already exploited for temporal resolved electromagnetic fields probing, some applications require a monochromatic beam and, as a consequence, the TNSA spectrum must be somehow tailored.

In addition, TNSA offers a source of energetic ions with a tunable cut-off energy. At the state of the art, however, an increase of performances is desired in several scenarios.

A greater insight of the acceleration process as well as its optimization can be achieved through experimental campaigns. Indeed, experiments performed in the last decades proved strong dependencies of TNSA on both laser and target parameters. It is widely accepted that laser intensity is a fundamental quantity in laser induced ion acceleration, with higher performances being expected with more intense beams. However, other laser features such as the energy, focal spot, duration, polarization and incidence angle, influence the physics of the interaction but are still poorly surveyed by experiments. Indeed, at fixed laser intensity, different combinations can lead to remarkably distinct results that must be studied and controlled in order to outline the most efficient conditions.

A natural strategy in order to boost TNSA would be to use more intense beams, nevertheless at the state of the art it is not trivial. Indeed, further improvements are slowed down due to current limitations on the laser technology. However, in the next years the advent of multi-PW laser facilities should allow to reach higher performances at the price of higher costs and dimensions. As a consequence, some of the above presented appealing features of laser-based accelerators (compactness and cheapness) are reduced. Therefore, a parallel approach to the problem is to adopt advanced target configurations which provide competitive features at already available laser facilities. Among the innovative solutions that have been proposed in the latest years, an interesting concept is given by multi-layered targets (MLT), formed by a foam layer deposited onto a solid substrate. The basic principle of this novel strategy is to exploit an efficient laser plasma coupling in the low density plasma formed in the foam to effectively boost ion acceleration in an enhanced TNSA-like scenario.

As complement of the experimental activity, simplified analytical models can provide an invaluable tool to interpret and support experiments as well as to guide future research. Theoretical descriptions are able to capture the most fundamental traits of the physical process and, as a results, offer reliable predictions of the most important features of the ion beam, given the initial conditions of both the laser and the target. In latest years these models allowed to understand the role of many quantities which affect the onset of TNSA, such as beam intensity, energy and target thickness. Nonetheless, a lot of effort is still required to gain a sufficient degree of knowledge even in the most investigated case of SLT. Furthermore, analytical modeling must be extended to novel targets concepts.

At this point it must be highlighted how the intrinsic complexity of TNSA, where ultra-intense electromagnetic radiation couples with charged particles to give rise to strongly non-linear effects and possibly plasma instabilities, makes analytical models remarkably hard to be developed. In this framework, numerical simulations are suitable tools to achieve a better understanding of the physical processes at play. These are able to reproduce some of the most important aspects of plasma-physics by the numerical solution of Maxwell-Vlasov equations. In particular, Particle In Cells (PIC) codes are largely exploited in order to investigate TNSA and to support both analytical and experimental works. PIC codes sample the whole plasma into macro-particles whose dynamics are self-consistently determined by Maxwell equations. Numerical simulations are largely exploited due to the fact that they can reliably reproduce the physical system and thus predict the possible outcomes of experiments, which is appealing to guide the activity. Moreover, they also allow to probe some features of the fundamental physics of TNSA which are not directly accessible in experiments (e.g. spatially and time resolved fields, particles phase spaces). As a result, PIC simulations can naturally complement the theoretical activity, providing a benchmark for the analytical models.

Motivations and Aim of the thesis

The fundamental goal of this work is to provide a theoretical description of laser induced electron heating suitable for both SLTs and MLTs which is supported by both numerical simulations and experimental results.
Indeed, the first part of my activity was dedicated to the data analysis of two ample experimental campaigns performed in 2014 and 2015 which tested SLTs and MLTs at different operating conditions. As far as SLTs are considered, the investigation allowed to further extend the comprehension of the influence of laser properties (i.e. intensity and polarization) on TNSA. Moreover, experiments regarding innovative MLTs proved the feasibility of this enhanced acceleration scheme and suggested proper target configurations in order to maximize its efficiency. This analysis was exploited in this PhD in order to test theoretical models, as will be later discussed.
According to the TNSA scheme, the electron heating resulting from laser-plasma coupling is a fundamental physical process which determines ion acceleration. A fine control over this can arguably lead to an optimization of the technique. Our work presents an improvement, with respect

to existing literature, of the modeling of electron heating in scenarios particularly relevant for ion acceleration. Several theoretical works have addressed this issue, providing estimations of the electron temperature as simple functions of the laser intensity. However, it is well known that, even in the simplest case of SLTs, many other relevant parameters, such as laser incidence angle and pulse polarization, deeply influence laser-plasma coupling. Moreover, these simplified approaches are not suitable for novel MLTs. In this work we aim to overcome these limitations, proposing a simple law to predict the electron temperature for SLTs irradiated in a wide range of laser parameters. We also approach the modeling of the electron heating for MLTs, additionally addressing the role of target nanostructure in laser-plasma coupling. Our assumptions are supported by an extensive 2D and 3D numerical campaign at different laser and target configurations. It is extremely challenging to obtain a direct experimental measurement for a fs time resolved electron temperature. However, the latter is a crucial parameter in many scenarios of intense laser-plasma interaction, such as laser-plasma particle acceleration. Therefore, to benchmark our models we relied on TNSA experimental data analyzed in the first part of this PhD. Combing our estimations with an existing model for ion acceleration, we compared its results with those obtained in the recent experimental campaigns. These results are relevant for scenarios that require efficient laser-plasma coupling (e.g. laser-driven ion acceleration, studies on electron transport, etc.). Moreover, our proposed scaling laws can allow to extend all TNSA analytical models which rely on estimations of the electron temperature.

Structure of the thesis

The PhD thesis is organized as follows:

- **Chapter 1**. In the first thesis chapter we offer a brief outlook over the evolution of laser technology with a particular emphasis on high power laser facilities which provide beams suitable for ion acceleration. We will then treat the crucial topic of relativistic laser-matter interaction. Starting from a single particle approach we will introduce the concept of *ponderomotive force*, a non-linear effect relevant in this physical scenario. Ultra-intense laser beams can promptly ionize matter, in this framework it is useful to provide some basics of plasma physics. We finally introduce some of the most appealing applications of ultra-intense laser-plasma interaction.

- **Chapter 2**. The second chapter is dedicated to the main subject of this PhD work, namely laser-induced ion acceleration. We describe the state of the art regarding this topic, with a particular interest on the most studied acceleration mechanism of TNSA, from the first experimental observations to the description of a simplified physical picture. At this regard, we then focus our attention into electron heating, a physical phenomenon critical in ion acceleration. We provide a description of some of the most important mechanisms as well as non-linear effects that can deeply influence laser-plasma interaction. Finally, we present some advanced-TNSA strategies which can arguably overcome current limitations of the technique.

- **Chapter 3**. This chapter is dedicated to the description of non-experimental approaches to the study of TNSA. We review some of the most relevant and used analytical models of TNSA which allow the estimation of quantities of great interest such as the ion cut-off energy. We then introduce numerical simulations which are largely exploited in this work to support the theoretical activity as well as to interpret experimental results. Finally, the objectives of this PhD will be extensively discussed.

- **Chapter 4**. In the fourth chapter we describe the two experimental campaigns performed in 2014 and 2015 in collaboration with the GIST institute in South Korea. A relevant part of this PhD was dedicated on the data analysis of such experiments which allowed to achieve a greater insight of TNSA with both flat foils and multi-layered targets. We present the influence of several crucial experimental parameters on laser induced ion acceleration, such as laser intensity and polarization as well as different target configurations. We also demonstrate how innovative foam attached targets can be successfully exploited in order to enhance TNSA over a broad range of laser intensities.
  The large and controlled data set obtained was used to support the theoretical and numerical activity as will be discussed in chapter 5.

- **Chapter 5**. In this chapter we study laser-plasma coupling, under physical conditions suitable for ion acceleration with both SLTs and MLTs, through a combined analytical and numerical approach. We derive simple yet predictive scaling laws to predict the temperature of laser-heated electrons over a wider collection of experimental parameters with respect to existing models. The theoretical work is supported by dedicated numerical aigns which led to a better comprehension of the physics beneath the process. Moreover, the electron temperature was evaluated under different operating conditions and these data were essential to calibrate our scaling laws. In order to benchmark our results we finally combine the new laws for the electron temperature with an existing TNSA model comparing its results with experiments in Chapter 4.

- **Chapter 6**. In the last chapter the conclusions of this PhD work will be drawn. This also allows to outline the path for future research

Publications and research activity

The content of this thesis were published in the following peer reviewed papers:

- **L Cialfi**, L Fedeli and M Passoni, âĂIJElectron heating in subpicosecond laser interaction with over-dense and near-critical plasmasâĂİ, Physical Review E **19**, 061301 (2016).
- M Passoni, A Sgattoni, I Prencipe, L Fedeli, D Dellasega, **L Cialfi**, Il Woo Choi, I Jong Kim, KA Janulewicz, Hwang Woon Lee et al., âĂIJToward high-energy laserdriven ion beams: Nanostructured double-layer targets,âĂİ Physical Review Accelerators and Beams **19**, 061301 (2016).
- I Prencipe, A Sgattoni, M Passoni , L Fedeli, D Dellasega, **L Cialfi**, Il Woo Choi, I Jong Kim, KA Janulewicz, Hwang Woon Lee et al., âĂIJDevelopment of foam-based layered targets for laser-driven ion beam production,âĂİ Plasma Physics and Controlled Fusion **58**, 034019 (2016).

During my PhD I have attended these conferences and schools:

- **Oral contribution** at “The 3rd International Conference on High Energy Density Physics (ICHEDP2016)” (Shenzhen 23-26 September 2016).
- **Poster presented** at the “Summer School Atoms and Plasmas in Super-Intense Laser fields”. (Erice, 12-22 July 2015).
- Conference Complex Plasma Phenomena in the Laboratory and in The Universe. (Rome, 19-20 January 2015).

- Course held by CINECA Introduction to Parallel Computing with MPI and OpenMP. (Bologna, 9-11 December 2014).

During my PhD I have been the P.I. of the ISCRA C 10^6 CPU hours project “LIonFAT” at CINECA (Italy).

1

Intense laser-matter interaction

This first chapter offers an overview of an appealing topic of both theoretical and experimental research: ultra-intense laser-matter interaction.
At this purpose 1.1 overlooks the evolution of the laser technology from its first theorization to the recent advent of Petawatt laser facilities. Section 1.2 covers the rich topic of ultra-intense laser-matter interaction, from a single particle approach to a short overview of plasma physics. Finally 1.3 presents some of the most appealing applications of this fertile research field.

1.1 Introduction to high power laser technology

The first theoretical basis for the advent of the laser technology were given by Albert Einstein in the well-known paper of 1917 "Zur Quantentheorie der Strahlung" [1] that led to the construction of the first laser in 1960 [2]. Ever since, research interest on this technology grew at a tremendous rate due to the possibility of generating electromagnetic pulses with unique features: monochromaticity, high spatial and temporal coherence. Moreover, they proved to be a reliable source of short (down to fs) and intense radiation (I>10^{20} W/cm^2).
The early evolution of the laser technology was marked by two techniques that enabled to increase the achievable intensity to over 10^{10} W/cm^2: Q-switch [3] and Mode-locking [4]. The first relies on a variable attenuator inside the resonant cavity which allows to control its Quality factor. The laser medium is pumped when the Q-factor is low (high losses per roundtrip) preventing the lasing and, thus, enabling strong population in-

version. The Q-factor, is then, abruptly increased and the large amount of energy stored in the gain medium is released in the form of an intense laser pulse. Modelocking on the other hand relies on a fixed phase relation between the longitudinal modes on the resonant cavity in order to generate, by the effect of interference, a train of high intensity short pulses (down to fs duration).

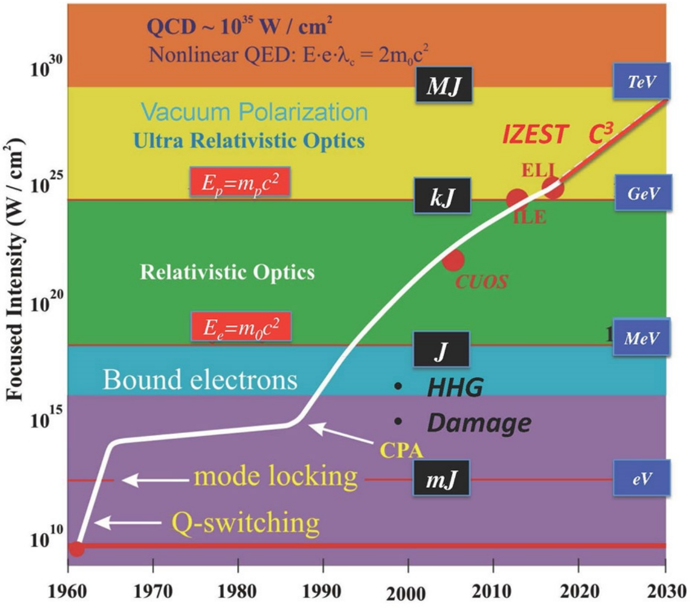

Figure 1.1: *Evolution of the laser technology*

Laser intensity can be further enhanced through several amplification stages. Indeed, an excited active medium (e.g. a doped optical fiber) interacting with a laser can produce coherent radiation. However, at higher intensities non-linear effects in the gain medium, such as self-focusing and high-harmonic generation, become increasingly important [5]. The first, in particular, leads to a strong amplification of the input laser beam to intensities (> GW/cm^2) beyond the damaging threshold of solid amplifiers. This condition can be easily reached with ultra-short pulses (<ps) and hampered the development of high power lasers, especially in femtosecond class, for over a decade (see figure 1.1).

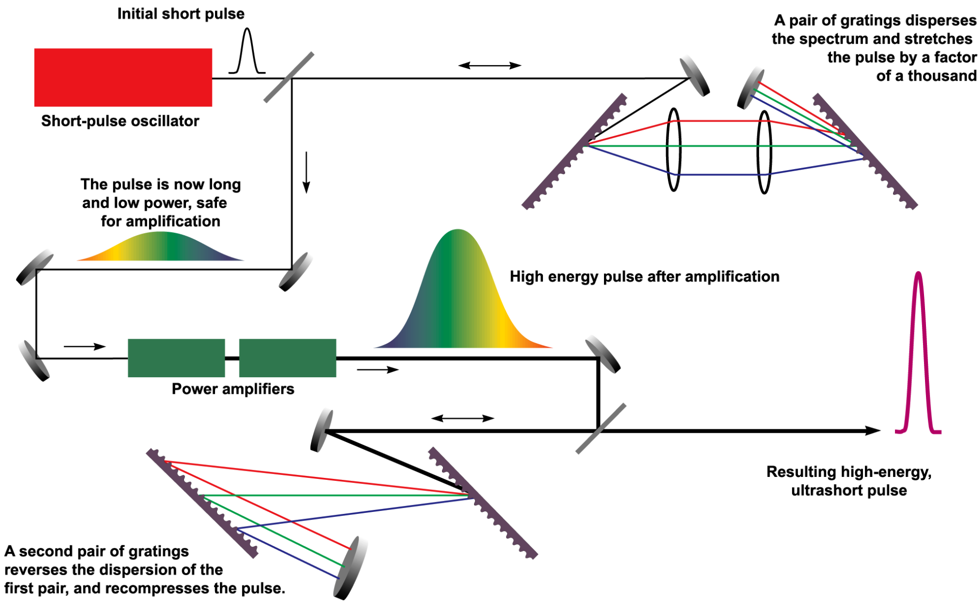

Figure 1.2: *Typical Chirped Pulse Amplification system*

In 1985 it was firstly proposed a technique to overcome this limitation: Chirped Pulse Amplification (CPA) [6]. In the typical CPA system presented in figure 1.2 a short (<ns) laser pulse with low energy ($\sim$ nJ) is stretched to nanosecond length using a pair of gratings or an optical fiber [7]. The basic principle of this technique is to obtain a frequency dependent phase-shift which leads to a pulse stretch and a time-dependent frequency. The so-called *chirped* pulse is *up-chirped* (figure 1.3) when the low-frequencies travel ahead the higher ones, *down-chirped* in the opposite case. The main advantage of pulse-stretching is that the output pulse is characterized by a lower peak intensity which can prevent damages in the gain mediums retaining the same energy of the input seed.

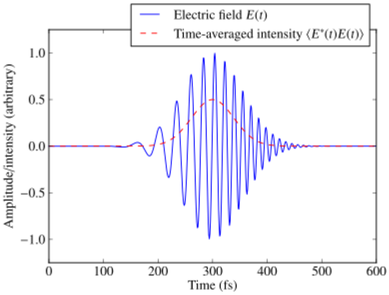

Figure 1.3: *Electric field of an up-chirped pulse, where the instantaneous frequency grows with time.*

As presented in figure 1.2, the laser beam travels through the amplification stages, acquiring energies of the order of the J (or higher) and, finally, is compressed back to a short duration, typically by optical gratings.
A further problem to be addressed, particularly relevant in high-power laser facilities, are the intense pre-pulses in temporal scales of ps-ns before the main beam. These pre-pulses, capable of matter ionization, are typically noxious in most experiments with thin or nanostructured targets and must be attenuated. Plasma-mirrors [8] are usually optically transparent solids which absorb or transmit most of the pre-pulse. This interaction generates a dense plasma which acts like a mirror, reflecting the main pulse. Double plasma mirror configurations can be adopted to reach high contrasts above 10^{10} at the price of ~ 50 % pulse energy depletion. CPA marked a crucial milestone for the advent of high power laser facilities in the last decades which can provide laser beams with power exceeding 100 TW, intensities above 10^{18} W/cm^2 and energies on target up to 10^2 J in sub ps durations.

1.1.1 High Power Laser Facilities

In ref. [9] are reviewed some of the most advanced high-power laser facilities (>100 TW) worldwide. Three main laser technologies proved to be suitable for achieving such powers allowing ultra-short pulse durations (<ps) combined with CPA: Ti:Sapphire [10], CO_2 [11] and Nd-based [12] lasers. The physical constraint on pulse duration is given by the well known TimeâĂŞbandwidth Product of the pulse duration and the laser bandwidth ($\Delta\tau \cdot \Delta\omega$). Due to the large bandwidth of Ti:Sapphire lasers, this technology can provide pulses down to $\sim$ 10 fs, while Nd-based and CO_2 lower limits are set in the $\sim$ 100 fs and $\sim$ ps range, respectively. Ultra-short durations are of extreme interest in laser-matter interaction,

also including sub-micrometric and nanostructured targets, the main topic of this work.

At the state of the art the outer reach for Ti:Sapphire and Nd-based laser technology is represented by PW-class facilities [13, 14], while the CO_2 systems approaching the 100 TW milestone [15].

High power beams, focused into few μm^2, can deliver extreme intensities ($I > 10^{20}$ W/cm^2), with the current world record set at $2.2 \cdot 10^{22}$ W/cm^2 at the 300 TW HERCULES laser facility [16].

In the latest years several ongoing projects are aimed at overcoming current limitations of PW facilities, in order to break into the 10 PW range. We here give some examples of recent projects which are predicted to be operative in the short term ($\sim$ 1-2 years). The PULSER laser system at the GIST institute (South Korea) is being upgraded from the current 2 PW peak power to 4 PW and is planned to be operative by the end of 2016 [17]. CLF-RAL facility has outlined an upgrade of VULCAN to reach 10 PW [18]. At the state the first stage of the project has been completed, including the Optical Parametric Chirped-pulse Amplification (OPCA) system, also adopted in several high power laser facilities [19–22]. The European funded ELI-Beamlines facility [23] in the Czech Republic is under construction and is expected to be operative in 2018. Its design project promises two outstanding operation modes: a *high energy mode* with a peak power of 10 PW with 1.5 kJ pulse energy delivered in 150 fs. The *high intensity mode* will provide up to 30 J laser pulses in 25 fs duration, resulting in intensities on target above 10^{22} W/cm^2. Finally, the French user facility Apollon [24, 25] has the objective of creating a laser beam with an extreme peak intensity ($I > 10^{22}$ W/cm^2), 150 J pulse energy and 15 fs duration with 1 shot/minute repetition rate. Apollon is expected to be the first laser to reach the peak power of 5 PW by the end of 2016, with a release design of 10 PW.

1.2 Intense laser matter interaction

The fast development of the laser technology enabled the study of interaction of charged particles with high intensity fields. Despite being an extensively studied topic over the last decades, it is still far from being fully understood due to the extreme richness of the physics characterizing this interaction regime. In this section, several key notions will be given to the reader, starting from single particle interaction in 1.2.1. In 1.2.2 the concept of *Ponderomotive force* will be introduced, while 1.2.3 will be dedicated to presenting several laser-induced ionization mechanisms. Finally in 1.2.4 laser-plasma interaction will be presented, as well as several of the most important quantities relevant in this thesis. For a more exhaustive description of the subject we recommend [26–28].

1.2.1 Single particle interaction

We here study the dynamic of a charged particle under the effect of a monochromatic plane wave traveling in $\hat{z}$ direction, described by the vector potential (in vacuum):

$$\begin{aligned} \mathbf{A} &= A_0 Re\left\{e^{-i(\omega t - kz)}\right\}\hat{e}_{xy}, \\ \mathbf{E} &= -\frac{1}{c}\frac{\partial \mathbf{A}}{\partial t}, \end{aligned} \tag{1.1}$$

being ω and $\mathbf{k}$ the frequency and the wave vector. In the non-relativistic limit, also ignoring the magnetic field, the particle motion is simply given by oscillations along the electric field with a quiver velocity of:

$$\frac{\mathbf{v}}{c} = \frac{q\mathbf{E}_0}{m\omega c}\sin(\omega t - kz) = \frac{q\mathbf{A}_0}{mc^2}\sin(\omega t - kz), \tag{1.2}$$

where q and m are the charge and the mass of the particle respectively. The solution suggests the definition of the dimensionless laser amplitude

$$a_0 \equiv \frac{qA_0}{mc^2} \equiv \frac{v_q}{c}, \tag{1.3}$$

which represents a key quantity in intense laser-matter interaction, weighting the importance of relativistic effects on the particle motion. From eq. 1.3 it follows that, for $a_0 \ll 1$ relativistic corrections can be neglected, while for $a_0 \geq 1$ a fully relativistic description must be considered. The dimensionless vector potential can be also directly linked to the laser irradiance via the modulus of the Poynting vector, using eq. 1.1:

$$I\lambda^2 = 1.37 \cdot 10^{18} a_0^2 \left[\frac{W\mu m^2}{\mathrm{cm}^2}\right] \times \begin{cases} 1, & \text{for linear polarization} \\ 2, & \text{for circular polarization.} \end{cases} \tag{1.4}$$

To describe the fully relativistic motion of a charged particle interacting with a monochromatic plane wave we start from the relativistic Lagragian of the system:

$$L(\mathbf{r}, \mathbf{v}, t) = -mc^2\sqrt{1 - \frac{v^2}{c^2}} + \frac{q}{c}\mathbf{v}\cdot\mathbf{A} - q\phi. \tag{1.5}$$

The equation of the motion can be found solving the Eulero-Lagrange equation:

$$\frac{d}{dt}\frac{\partial L}{\partial \mathbf{v}} = \frac{\partial L}{\partial \mathbf{r}}. \tag{1.6}$$

Leading to the well-known equation:

$$\frac{\partial \mathbf{p}}{\partial t} = q\left(\mathbf{E} + \frac{\mathbf{v}}{c} \times \mathbf{B}\right). \tag{1.7}$$

We can define the canonical momentum $\mathbf{P}$ as it follows:

$$\mathbf{P} = \frac{\partial L}{\partial \mathbf{v}} = \mathbf{p} + \frac{q}{c}\mathbf{A}, \tag{1.8}$$

being $\mathbf{p} = \gamma m \mathbf{v}$ the relativistic linear momentum and $\gamma = 1/\sqrt{1 - v^2/c^2}$ the Lorentz gamma factor.

The condition of monochromatic plane wave greatly simplifies the problem, allowing an analytical solution otherwise impossible to be retrieved in the general case. This condition also implies the existence of invariant quantities of the system. First of all, a plane wave depends only on the spatial coordinate defining its propagation direction (we assumed to be $\hat{z}$). The Lagrangian of the system is, thus, constant in the plane orthogonal to $\mathbf{k}$ ($\hat{x}\hat{y}$). $\partial L/\partial \mathbf{r}_\perp$=0 leads to:

$$\frac{d}{dt}\frac{\partial L}{\partial \mathbf{v}_\perp} = \frac{d}{dt}\mathbf{P}_\perp = 0 \longrightarrow \mathbf{P}_\perp = \mathbf{p}_\perp + \frac{q}{c}\mathbf{A}_\perp = cost. \tag{1.9}$$

Another invariant quantity follows from the assumption of plane wave in vacuum. The vector potential must be then dependent only to the coordinate $\tau = t - kz$. We can then write the partial time derivative of the Lagrangian $\frac{\partial L}{\partial t} = -c\frac{\partial L}{\partial z}$. Using this relation with 1.6 and reminding that for a plane wave in vacuum $A_z = 0$, we obtain:

$$\frac{dE}{dt} = c\frac{\partial L}{\partial z} = c\frac{d}{dt}\frac{\partial L}{\partial v_z} = c\frac{dP_z}{dt} = c\frac{d(p_z + qA_z)}{dt} \tag{1.10}$$

where $E = E_k + mc^2$ is the particle total energy. It can be easily found the second invariant of the system:

$$E - cp_z = cost = mc^2, \tag{1.11}$$

if the motion of a charged particle initially at rest is considered, the actual value of the constant must be equal to its rest energy mc^2. Equation 1.11

allows to obtain the following relation for the longitudinal component of the linear momentum p_z.

$$p_z = mc(\gamma - 1). \tag{1.12}$$

Combining this relation with the expression for the relativistic energy $E = \gamma mc^2 = \sqrt{(mc^2)^2 + (p_z c)^2 + (p_\perp c)^2}$ we obtain a direct link between the longitudinal and transverse component of the linear momentum.

$$2mp_z c = p_\perp^2 \tag{1.13}$$

Defining these normalized quantities $\hat{\mathbf{p}} = \frac{\mathbf{p}}{mc}$, $\mathbf{a} = \frac{e\mathbf{A}}{mc^2}$ and assuming the vector potential along $\hat{y}$ axis, the linear momentum equation can now be easily written:

$$\begin{aligned} \hat{p_z} &= \frac{\gamma}{c}\frac{dz}{dt} = \frac{a^2}{2}. \\ \hat{p_y} &= \frac{\gamma}{c}\frac{dy}{dt} = a_y. \end{aligned} \tag{1.14}$$

Combining eq. 1.13 with eq. 1.14 we obtain:

$$\begin{aligned} \frac{\hat{v_z}}{c} &= \frac{a^2}{2(1 + a^2/2)}. \\ \frac{\hat{v_y}}{c} &= \frac{a_y}{(1 + a^2/2)}. \end{aligned} \tag{1.15}$$

We can solve the equation of motion in terms of $\tau = t - kz$:

$$\begin{cases} z(\tau) = \frac{ca_0^2}{a_0^2+4}\left[\tau + (2\omega)^{-1} sin(2\omega\tau)\right] \\ y(\tau) = \frac{ca_0}{\omega} sin(\omega\tau) \end{cases} \tag{1.16}$$

In figure 5.5 we report three representative trajectories at different field amplitudes. If $a \ll 1$ the motion is given mostly by a traverse quiver and the non relativistic limit is then retrieved. Non linear, relativistic effects become relevant at higher intensities: if $a \gg 1$ the motion is dominated by the longitudinal component. We highlight how, from eq. 1.16, the longitudinal motion is given by a constant-velocity drift $v_d = \frac{ca_0^2}{a_0^2+4}$ coupled with oscillations at 2ω.
If circular polarization is considered similar results can be obtained. The main difference is the absence of the longitudinal oscillations and particles move in an helicoidal trajectories.

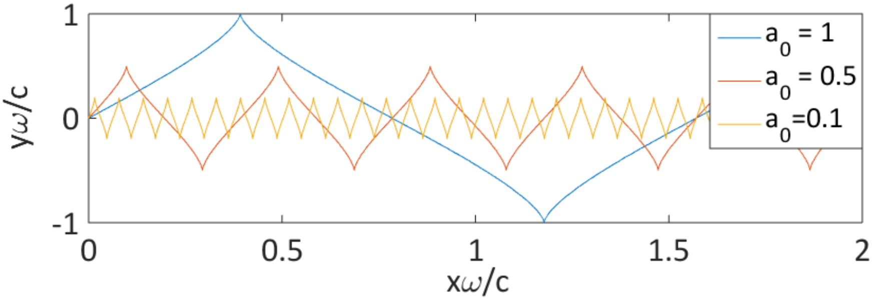

Figure 1.4: *Representative electron trajectories under different normalized field amplitudes:* $a_0 = 1$ *(blue),* $a_0 = 0.5$ *(red) and* $a0 = 0.1$ *(orange)*

A fundamental result of this analysis is to prove that, under ultra-intense electromagnetic fields conditions, the longitudinal and transverse components of charged particle motion are strictly linked due to the onset of non-linear effects.

1.2.2 Ponderomotive force

Another non-linear effect crucial in laser-plasma interaction is known as *Ponderomotive force*, experienced by a charged particle moving in an inhomogeneous electromagnetic field. The exact solution can not be analytically found, however, a simple form of this force can be obtained in the framework of a perturbative, non relativistic single particle interaction with quasi-monochromatic electromagnetic field given by:

$$\begin{cases} \mathbf{E}(\mathbf{r}, t) = \mathbf{E}_0(\mathbf{r}) cos(\omega t - \mathbf{k} \cdot \mathbf{r}) \\ \frac{\nabla \mathbf{E}_0}{\mathbf{E}_0 \mathbf{k}} \ll 1 \end{cases} \tag{1.17}$$

The particle motion is simply given by the Lorentz force:

$$m\ddot{\mathbf{r}} = q\left(\mathbf{E} + \frac{\mathbf{v}}{c} \times \mathbf{B}\right) \tag{1.18}$$

this equation can be solved again, expanding the fields around the initial particle position r_i:

$$\mathbf{E}(\mathbf{r}) = \mathbf{E}(\mathbf{r}_i) + (\delta\mathbf{r} \cdot \nabla)\mathbf{E}(\mathbf{r}_i) + o[\delta\mathbf{r}^2] \tag{1.19}$$

where $\delta\mathbf{r} = \mathbf{r} - \mathbf{r}_i$. At the 0-th order the dynamic is a simple quiver motion around the initial position:

$$\ddot{\mathbf{r}}^{(0)} = \frac{q}{m}[\mathbf{E}(\mathbf{r}_i)] \tag{1.20}$$

that can be solved retrieving the well known result:

$$\begin{cases} \mathbf{r}^{(0)} = \mathbf{r}_i - \frac{v_q}{\omega} cos(\omega t - \mathbf{k}\cdot\mathbf{r}) \\ \dot{\mathbf{r}}^{(0)} = -v_q sin(\omega t - \mathbf{k}\cdot\mathbf{r}) = -v_q sin(\tau) \end{cases} \tag{1.21}$$

where v_q is the already defined quiver velocity. If eq. 1.21 is subtracted to eq. 1.18 and the result is linearized, we obtain this equation for the 1-st order dynamics:

$$\ddot{\mathbf{r}}^{(1)} = -\frac{q}{m}\left[\left(\delta\mathbf{r}^{(0)}\cdot\nabla\right)\mathbf{E}(\mathbf{r}_i) + \frac{\dot{\mathbf{r}}^{(0)}}{c}\times\mathbf{B}\right] \tag{1.22}$$

The magnetic field is determined by Faraday's law:

$$-\frac{1}{c}\frac{\partial\mathbf{B}}{\partial t} = \nabla\times\mathbf{E} \rightarrow \mathbf{B} = \frac{c}{\omega}sin(\tau)(\nabla\times\mathbf{E}_0) + \frac{c\mathbf{k}}{\omega}\times\mathbf{E}_0 cos(\tau) \tag{1.23}$$

If we use this relation with eq. 1.22 we finally find:

$$\ddot{\mathbf{r}}^{(1)} = -\left(\frac{q}{m\omega}\right)^2 [(\mathbf{E}_0\cdot\nabla)\mathbf{E}_0 cos^2(\tau) + \mathbf{E}_0\times(\nabla\times\mathbf{E}_0)sin^2(\tau) + \mathbf{E}_0\times(\mathbf{k}\times\mathbf{E}_0)sin(2\tau)]. \tag{1.24}$$

We remark how the perturbed particle motion is characterized by components dependent to the non-uniformity of the electromagnetic field as well as a longitudinal force at double the wave frequency (in accord with the previous section results). In order to study the slowly varying part of the motion, we time average eq. 1.24 during a field period. If we then exploit vector identities we finally reach this important result:

$$m\ddot{\mathbf{r}} = -\nabla\left(\frac{q^2}{4m\omega^2}|\mathbf{E}_0|^2\right) = -\nabla U_p = \mathbf{f}_p. \tag{1.25}$$

The particle motion can be interpreted as perturbed by the effect of the *Ponderomotive potential* U_p and the related *Ponderomotive force* f_p *Ponderomotive force.* These quantities are connected to the energy density of the electromagnetic field or, more precisely, to the isotropic component of the Maxwell stress tensor. The net effect of this force is to push charged particles from high energy density regions to lower ones. Finally we underline how the ponderomotive force is inversely proportional to the particle mass, its action is thus more efficient with low mass particles such as electrons than heavy ions.

We finally remark how a more refined derivation of the ponderomotive force in a fully relativistic framework is provided in ref. [29].

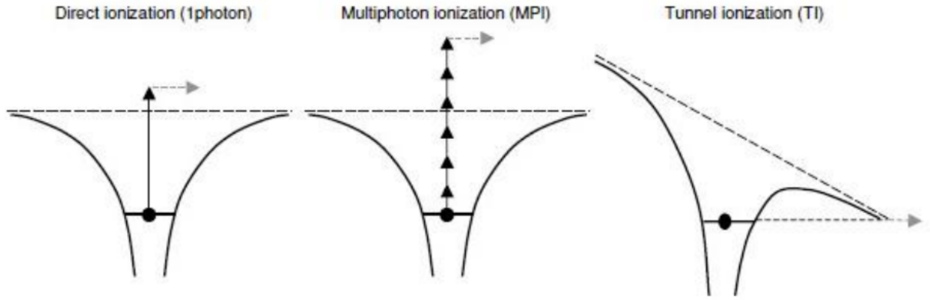

Figure 1.5: *Schematic representation of the single particle ionization mechanisms. a) single photon ionization b) multi-photon ionization (MPI) and c) tunnel ionization (TI)*

1.2.3 Ionization of matter

The single particle approach is a very basic and useful starting point to understand some crucial aspects of particle interactions with electromagnetic field. However, this method displays clear limitations considering that in most of experiments a large collection of atoms and molecules is involved. These can be ionized by intense laser beams, leading to the creation of a population of free charge carriers which can mutually interact. It is, indeed, worth to dedicate this section to briefly present some basic features of laser-induced ionization, starting from the simple case of single-atom.
Atom ionization happens if an electron is promoted from its bound state to a continuum free level. This can be either achieved by photo-electric effect if a high-frequency photon is absorbed or multi-photon absorption of lower frequency photons if sufficient intensity and, thus, photons are provided (see figure 1.5). In this framework, it is necessary to define an *intense* laser beam. In this context, the *atomic intensity* is defined as the laser intensity at which the electric field of the laser beam matches the binding electric field felt by the electron in the atom which can be estimated by means of the Bhor electric field:

$$E_a = \frac{e}{a_b^2} \simeq 5.1 \cdot 10^9 V/m \tag{1.26}$$

where $a_b = \frac{\hbar^2}{me^2}$ is the Bohr radius. The *atomic intensity* is simply given by this relation:

$$I_a = \frac{cE_a^2}{8\pi} \simeq 3.5 \cdot 10^{16} W/\mathrm{cm}^2. \tag{1.27}$$

If $I_L > I_a$ almost complete target ionization is guaranteed. However, even at lower laser intensity ionization can occur by either *multi-photon* (MPI) or *tunnel-ionization* (TI). In the former an electron can be promoted to the free state by multiple kicks given by low frequency photons. The emission rate (R_n) due to this mechanism can be evaluated with a perturbative theory:

$$R_n = \sigma_n I_L \tag{1.28}$$

where σ_n is the n-th photon emission cross section. Even thought σ_n decreases for high n, if enough laser intensity is provided ($I_L > 10^{10} W/\mathrm{cm}^2$) this process can occur [30].
Matter ionization below the *atomic intensity* threshold can be achieved via another mechanism, competitive with MPI: *tunnel ionization*(TI). A basic assumption for MPI modeling is that the atomic binding potential is not perturbed by the laser field which does not hold for high intensities. As presented in fig. 1.5.b, if the electric field of the beam is sufficiently strong, the potential felt by a bound electrons is bended, creating a well. Electron may tunnel through this potential barrier, leading to atom ionization.
The relative weights of MPI and TI mechanisms in atom ionization can be estimated through the *Keldysh parameter* [31]:

$$\gamma_k \sim \sqrt{\frac{E_{ion}}{U_p}} \tag{1.29}$$

where U_p is the ponderomotive potential defined in 1.25 and E_{ion} is ionization energy . If γ_k<1 (long wavelengths and strong fields) the ponderomotive potential is strong enough to bend the binding potential and tunnel ionization dominates over MPI, if $\gamma_k > 1$ the opposite holds.
Due to MPI and TI, complete atom ionization can occur at intensities orders of magnitude lower than the atomic intensity (I $\sim 10^{14}$ W/cm^2). These mechanisms have been studied for a single atom-interaction but can be still extended to low density material ionization. If solid-like density targets are considered, multi-particle interactions must be taken into account leading to a complex and still fertile topic of research [32]. In particular, interaction of short pulses with solid targets leads to the generation of a thin ionized layer at the vacuum-solid interface where the thermal equilibrium is not established during the interaction. Non-equilibrium models must be considered in order to estimate the ionization degree of the material and have been presented elsewhere [33]. In conclusion, regardless the ionization process taking place, in physical conditions relevant for our

work (sub-picosecond, ultra-intense laser pulses), targets can be rightfully expected to be fully ionized before the interaction with the lases pulse peak intensity takes place.

1.2.4 Electromagnetic waves interaction with plasma

A plasma can be defined as the particular state of matter in which a significant fraction of charge carriers is in an unbound state and collective interactions overshadow binary ones.

Due to the purposes of this work, some basic but crucial quantities in plasma physics will be here presented.

First of all, charged particles in a plasma are in an unbound state having their dynamics governed by electromagnetic interactions. If a globally neutral plasma is considered, its collective response acts to restore this condition if a perturbation is applied. Indeed, charge separation effects can be observed only under a well defined spatial scale. The electrostatic potential generated by an external charge can be easily demonstrated being:

$$\begin{cases} \phi(\mathbf{r}) = \frac{q}{r} e^{-\frac{\mathbf{r}}{\lambda_D}} \\ \lambda_D = \left(4\pi e^2 \sum_j \frac{n_j Z_j^2}{T_j}\right)^{-1/2} \end{cases} \tag{1.30}$$

where q is the charge of the external particle, the j index refers to the j-th particle population in the plasma and n_j, Z_j and T_j its density, atomic number and temperature, respectively. [1] The *Debye length* λ_D is a quantity of utmost importance in plasma physics as it states the distance over which significant charge separation can occur.

This definition arises from the solution of a simplified electrostatic problem. In order to properly study the collective response of a plasma to an electromagnetic wave the solution of the coupled system of Maxwell and particle motion equations should be required. This, however can not be achieved either analytically or numerically, the problem must be then treated by statistical means. The most fundamental approach is given by kinetic models which study the evolution of distribution functions of plasma particles. This is achieved in the most general case coupling Boltzmann and Maxwell equations. Simplified approaches, given by Vlasov or Fokker-Plank equations, are able to reduce some of the intrinsic complexity of the collisional term in the Boltzmann equation by completely neglecting this term (Vlasov) or considering small deflections collisions

---

[1] In this work we define “temperature” as the product of the actual temperature and the Boltzman constant K_b, so that $T \equiv K_b T$.

(Fokker-Plank). As it will be later discussed, the Vlasov approach can be extremely useful in the specific context of this PhD work.
A different approach is given by two fluid models, obtained by integration of Boltzmann equations in the velocity space. The plasma can be pictured as composed by two charged fluids, electrons and ions, which electromagnetically interact. These models omit some important physical processes but represent a fundamental starting point in many analytical works.
Indeed, the basic physical picture of a non-relativistic, linearized, cold (i.e. thermal effects are not considered) two fluid plasma allows to define some quantities of crucial importance. In such scenario the dispersion relation can be written in this compact form:

$$\epsilon\left(\frac{k^2c^2}{\omega^2}-\epsilon\right)=0 \tag{1.31}$$

where ϵ is the dielectric tensor which is, in our description, a scalar that can be expressed as:

$$\epsilon=1-\frac{4\pi}{\omega^2}\sum_j\frac{q_j^2n_{0j}}{m_j} \tag{1.32}$$

the j subscript refers to the j-th charged particles population in the plasma. We can then define a fundamental quantity in laser-plasma interaction, the plasma frequency of the j-th component which reads as follows:

$$\omega_{pj}=\sqrt{\frac{4\pi q_j^2n_{0j}}{m_j}}. \tag{1.33}$$

The total plasma frequency $\omega_p^2=\sum_j\omega_{pj}^2$ can be approximated to the electron component due to the higher charge over mass ratio with respect to ions. The dielectric coefficient can be finally written as:

$$\epsilon=1-\frac{\omega_p^2}{\omega^2}\simeq 1-\frac{\omega_{pe}^2}{\omega^2}. \tag{1.34}$$

If this relation is combined with 1.31 the expression for the longitudinal ($\omega=\omega_{pe}$) and the transverse modes can be found. In particular, the latter can be expressed as:

$$\omega^2=\omega_{pe}^2+k^2c^2. \tag{1.35}$$

According to eq. 1.35, electromagnetic waves can propagate through the plasma if their frequencies exceed ω_{pe}. The propagation condition can be also written in terms of the plasma density combining eq 1.35 with eq.

1.33. The critical density is defined as the plasma density at which the wave and the plasma frequencies are matched:

$$n_{cr} = \frac{m_e \omega^2}{4\pi e^2}. \tag{1.36}$$

If the electron density n_e is greater than this value the plasma is *over-dense*, electromagnetic waves are reflected back in a skin depth layer ($\lambda_{sd} = c/\omega_{pe}$), typically in the order of tens of nanometers for solid density plasmas ($n_e \gg 100 n_c$). On the other hand plasmas with $n_e < n_{cr}$ are called *under-dense* and laser pulses can propagate through their entire volumes. Finally, the condition $n_e \sim n_{cr}$ define the *near-critical* zone. This latter regime is a challenging topic of research, particularly interesting in plasmas created by low density material irradiation (e.g. nanostructured materials). Due to its relevance in this thesis work, a more detailed description of laser-plasma coupling will be provided in 2.1.3.
In the high intensity regime, non-linear relativistic effects must be taken into account. We now present the impact of these in the framework of a hydrodynamical description of a cold, non collisional relativistic plasma. We start from the relativistic linear momentum balance equation of the j-th population of the plasma:

$$\left(\frac{\partial}{\partial t} + \mathbf{u}_j \cdot \nabla\right) \mathbf{p}_j = q_j \left[-\frac{1}{c}\frac{\partial \mathbf{A}}{\partial t} - \nabla\phi + \frac{\mathbf{u}_j}{c} \times (\nabla \times \mathbf{A})\right] \tag{1.37}$$

Introducing these normalized quantities:

$$\frac{\mathbf{u}}{c} = \hat{\mathbf{u}}, \ \frac{\mathbf{p}}{mc} = \hat{\mathbf{p}}, \ \frac{q\mathbf{A}}{mc^2} = \mathbf{a}, \ \frac{q\phi}{mc^2} = \hat{\phi} \tag{1.38}$$

eq. 1.37 can be written in this compact form:

$$\frac{\partial}{\partial t}(\hat{\mathbf{p}} - \mathbf{a}) - \hat{\mathbf{u}} \times [\nabla \times (\hat{\mathbf{p}} - \mathbf{a})] = \nabla\phi - \nabla(\gamma - 1). \tag{1.39}$$

If a fluid initially at rest is considered, eq. 1.39 can be separated in perpendicular and parallel components with respect to the wave vector.

$$\begin{cases} \hat{\mathbf{p}}_\perp = \mathbf{a} \\ \frac{1}{c}\frac{\partial}{\partial t}\hat{\mathbf{p}}_\parallel = \nabla\hat{\phi} - \nabla(\gamma - 1) \end{cases} \tag{1.40}$$

with $\gamma = \sqrt{1 + \hat{\mathbf{p}}_\parallel^2 + \hat{\mathbf{p}}_\perp^2} \simeq \sqrt{1 + \mathbf{a}^2}$. We are here approximating the Lorentz factor with the transverse quiver which holds for a weak non-linearity. The $\nabla(\gamma - 1)$ term of system 1.40 can be associated to an effective force pushing longitudinally the plasma fluid in the form of:

$$f_p = -mc^2\nabla\left(\sqrt{1-\mathbf{a}^2}-1\right) = -\nabla U_p. \tag{1.41}$$

The relation just found is similar to the results of a single particle interaction in eq. 1.25.
If eq. 1.37 is linearized and coupled with Maxwell equations, the relativistic correct formulation of eq. 1.35 is obtained:

$$\omega^2 = \frac{\omega_{pe}^2}{\gamma} + k^2c^2 \tag{1.42}$$

where $\gamma = \sqrt{1+p^2+a^2}$ is the Lorentz-factor and p is the normalized plasma fluid momentum and a the normalized laser amplitude defined in 1.3. The definition of the critical density must also be modified:

$$n_{cr} = \gamma\frac{m_e\omega^2}{4\pi e^2}. \tag{1.43}$$

If we finally study a plasma at rest and we time-average 1.43, in the high intensity regime ($a_0 > 1$) we can approximate the relation as:

$$n_{cr} = \sqrt{1+a_0^2/2}\frac{m_e\omega^2}{4\pi e^2} \simeq \frac{a_0}{\sqrt{2}}\frac{m_e\omega^2}{4\pi e^2} \tag{1.44}$$

For high-intensity laser beams $I > 10^{20}W/\text{cm}^2$ the critical density can grow several times due to relativistic effects. In such condition ultra-intense radiation can still propagate in plasma densities defined as *over-dense* at lower intensities. In conclusion, the longitudinal and transverse plasma dynamics are tied by non-linear effects and the inhomogeneities of electromagnetic fields lead to the generation of an effective force pushing charged particles to regions of lower radiation pressure. If a fully non-linear description is considered the analysis gets even more complex, i.e. the ponderomotive force may shape the density profile changing the dispersion relation and thus affecting the propagation of the wave itself.

1.3 Potential applications

Ultra-intense laser interaction with plasmas is a fertile topic of both theoretical and experimental research. In this section we will cover some of the most important applications regarding this field.

Plasma Wake Acceleration (PWA)

One of the most challenging and promising application of laser-plasma interaction is wake-field acceleration of charged particles, firstly proposed in [34]. The basic principle of this technique is to excite plasma waves in an under-dense plasma. These waves are associated to strong longitudinal electric fields (GeV/cm) that can effectively accelerate charged particles. Collective plasma modes can be excited with different seeds:

- The ponderomotive force associated to an intense laser field. This mechanism is called *Laser Wake-Field Acceleration* (LWFA) and is the most experimentally studied at the state of the art [35].
- Energetic electron or proton bunches. This mechanism is called *Plasma Wake-Field Acceleration* (PWFA) and is promising for the possibility to create longer and more stable plasma wakes [36].
- Other schemes such as *Laser Beat-Wave Acceleration* (LBWA). The wake-field is excited by the beat-wave generated by two different laser wavelengths [37]

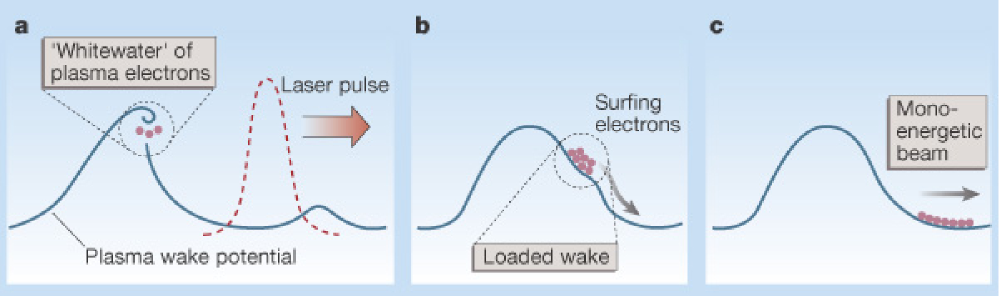

Figure 1.6: *Representation of electron plasma-wake acceleration. a) The excited plasma waves grows steepening its profile until the wave-break occurs. Electrons in the white-water (in analogy of wave-breaking of water waves) overcomes the plasma wave and are accelerated. b) Electrons deform the plasma wave, starting to slow down and trapping more electrons c) electrons reach the bottom of the wake and moves coherently with the phase velocity of the wave (figure taken from [38]).*

As pictured in figure 1.6, due to an external force the plasma wave can grow, leading to strong electron oscillations and, when wave breaking occurs, energetic trapped electrons (or ions) are expelled from the plasma. These accelerators are potentially appealing for their compactness and cheapness with respect to traditional ones. For instance 1 GeV electrons have been accelerated at the Lawrence Berkeley National Laboratory with

a centimeter-scale accelerator [39] while similar energies can be achieved with traditional techniques with tens of meters long machines. The current world record has been achieved in 2014 with a 40 fs long Ti:Sapphire laser pulse, delivering up to 16 J to an under-dense wave-guided plasma and producing electron bunches with energies up to 4.2 GeV [40].
In the latest years the outer reach of Plasma Wake electron Acceleration is represented by multi-stages LWFA in which electrons bunches accelerated by a plasma-wake are further boosted in followings wake-fields. This research is aimed at providing energies comparable to regular accelerators, although hundreds of stages are required in principle [41].
Another possible evolution of wake-field accelerators can be achieved with ion-driven PWFA. Due to the higher energy and mass, proton bunches can drive wake-fields over much longer plasma lengths than other drivers. Reaching the TeV-electrons milestone would be of extreme interest in the context of fundamental physics. Indeed a future electronâĂŞpositron collider would have the potential for new physical research as well for the precise measurement of phenomena already discovered at the Large Hadron Collider. The energies required, however, are not likely to be obtained with linear accelerators or synchrotrons due to the required 10 km lengths of the former and 100 km radii of the latter. A step forward could be made with PWFA and is the aim of the recent AWAKE project at CERN [42].
Due to the higher inertia of ions most of the originally proposed schemes ignored their possible motion. The technique should be indeed ineffective in ion acceleration. However, as presented in 1.2.1, when $a_0 > 1$ electrons inertia effectively grows due to relativistic effects, eventually becoming comparable with that of background ions. As suggested by Bulanov et al. in [43] ion motion may become relevant for laser amplitudes $a_0 > \sqrt{m_i/m_e} \sim 40$ which can be achieved at intensities already available (I$>2.5 \cdot 10^{21} W/\text{cm}^2$). Accordingly to [44], ions can be accelerated by the plasma wake to energies comparable or higher than electrons suitable for different applications.

X-ray and photons sources

Electrons produced by PWA can be used as a compact source of secondary X-ray radiation due to *bremsstrahlung* effect [45]. In [46] the authors proved the feasibility of PWA combined with oscillators in order to generate visible synchrotron radiation. The emitted wavelength scales with the energy of accelerated electrons and is characterized by

a narrow-bandwidth spectra. Moreover the short duration of electron bunches ($\sim$ 10 fs) results in a very high peak brilliance of the order of $6.5 \cdot 10^{16}$ photons/s/mrad^2/mm^2/0.1%bandwidth. These features make them appealing and versatile sources of radiation from the infrared to X-ray energies.
As a final remark, PWA-photons of energies exceeding 10 MeV have already proved suitable for nuclear physics applications such as (γ,n) [47] and photo-fission [48].

Laboratory Astrophysics

Astrophysical research has traditionally been divided into observations and theoretical modeling. A component missing was a benchmark tool to test theories in an experimental controlled environment. Intense lasers allowed to bring matter to such extreme conditions of both temperature (10^8 K) and density (up to 10^2 g/cm^{-3}) and strong pressures ($\sim$ Gbar), suitable for astrophysics. Regardless the gargantuan time and spatial scales, astrophysical phenomena can be experimentally reproduced in laboratory if similarity conditions among physical quantities are met [49]. Two main types of similarities can be reproduced in laboratory. In *sameness* experiments thermodynamical conditions (e.g. temperature and pressure) identical to those of the astrophysical media must be reproduced. With this approach the equation of state, emissivity, opacity, or other properties of the hot and dense material can be studied. For instance opacity measurement of a controlled iron plasma were performed in the NOVA laser facility at the Lawrence Livermore National Laboratory and these results were of particular interest in radiative transfer modeling in astrophysics [50]. In the *similarity* approach, astrophysical processes can be reproduced in laboratory if the equations governing their evolutions retain the same form if correctly rescaled [49]. With this method astrophysical shock waves [51, 52], magnetic recombination [53] and Rayleigh-Taylor instabilities [54] can be successfully studied in a tabletop experiment.

Atto-second Pulses generation

Ultra-intense laser plasma interaction could allow the production of atto-second pulses which could be of extreme interest in the framework of ultra-fast measurements. One of the most studied mechanisms is called *Relativistic Oscillating Mirrors* [55, 56]. The strong radiation pressure of an ultra-intense fs laser pulse can drive relativistic oscillation of a plasma

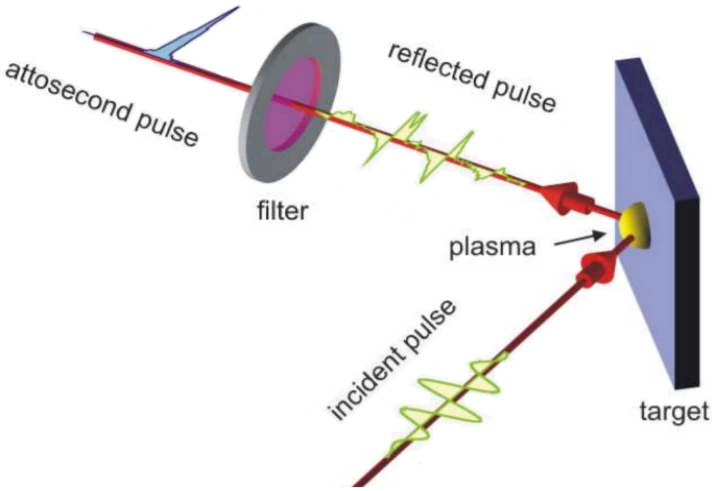

Figure 1.7: *Attosecond pulse generation with Relativistic Oscillating Mirrors [55]*

mirror. An electromagnetic wave interacting with a moving mirror experiences a Doppler-shift which can rise its frequency up to a factor $4\gamma^2$ when the phase match with the surface-oscillation is met [57]. As presented in figure 1.7 an atto-second burst (or a train of burst, depending on the seed pulse duration) can be obtained if a proper filtering of the pulse is performed.

Laser induced ion acceleration

Intense electromagnetic fields and radiation pressures may induce strong charge separations in irradiated plasmas and can be exploited to induce ion acceleration. Indeed, laser-driven ion acceleration is an active research topic, which has attracted significant theoretical and experimental efforts in the last decades [58, 59]. Research activity in this field aims at providing compact ultra-short sources of high energy ions for a variety of potential applications such as hadron-therapy [60], neutron and radionuclides production [61–63] and proton fast ignition [64]. Moreover, besides these foreseen applications, laser-driven ion sources already find use in experiments as a tool to investigate the time-resolved structure of electromagnetic fields [65].
The first investigated and observed mechanism is called Target Normal Sheath Acceleration (TNSA) [66–68], presented in fig. 1.8. This accel-

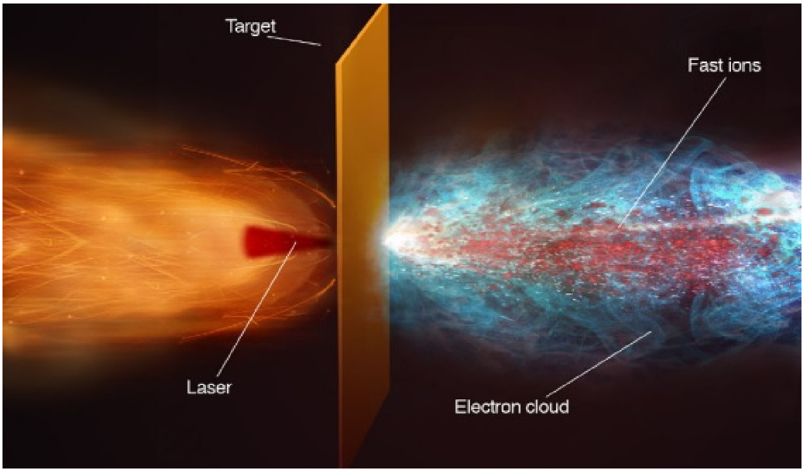

Figure 1.8: *Artistic representation of laser induced ion acceleration resulting from the interaction of an intense laser beam with a solid foil (image from [58]).*

eration scheme stands out for its robustness [63, 69, 70] and for its far less demanding experimental requirements. TNSA is arguably the most natural acceleration scheme, to the point that, not infrequently, it must be suppressed in order to observe other acceleration mechanisms such as shock waves, as reported in [51].

In TNSA, a laser beam is focused into a typically flat solid target, creating a greatly over-dense ($n_e \gg 100n_c$) plasma. The laser induced electron heating creates a population of hot electrons which expand through the target. As they cross the rear surface a strong electrostatic field (TV/m) is formed due to charge separation. This leads to the acceleration of ions from the rear surface to energies exceeding tens of MeV [71] and characterized by an exponential-like spectrum. TNSA ions are typically originated from hydrocarbon contaminants of the rear surface, but they can come also from the bulk of the target or from a specifically prepared coating layer [58, 59].

Another acceleration scheme largely investigated is called Radiation Pressure Acceleration (RPA). In order to discern RPA from TNSA electron heating must be suppressed and this condition is typically achieved using circularly polarized laser pulses at normal incidence [72]. This acceleration mechanism relies on the charge separation at the front surface due to the radiation pressure pushing electrons inside the target. A capacitor-like charge distribution is formed, accelerating ions. The advantage of RPA with respect to TNSA lies in the possibility to produce mono-energetic, high energy ions which can be in principle more suitable for most of the foreseen applications of laser-induced ion acceleration. However it is more experimentally challenging, since higher intensities ($I > 10^{22}$ W/cm^2) are required to provide enough radiation pressure to induce a strong charge separation, moreover, RPA ion spectra is not straightforward to be isolated from other competitive acceleration mechanism simultaneously taking place (like TNSA). It must be remarked how a recent work [73] proved that, exploiting the relativistic self-focusing and pulse steepening in a near-critical layer over a solid substrate, laser intensity could be enhanced, enabling the experimental observation of RPA at lower beam intensities ($I \sim 10^{20} W/\mathrm{cm}^2$) than traditional schemes. A more detailed description of laser induced ion acceleration will be provided in the chapter 2.

2

Laser induced ion acceleration

Since the first experimental observations of multi-MeV protons accelerated by intense laser beams in early years 2000 [66–68], laser induced ion acceleration has attracted significant experimental and theoretical interest [58, 59]. As anticipated in 1.3, laser-based accelerators could be a compact source of high-energy, spatially and temporally collimated ion beams. Due to these features, they are appealing for a number of practical applications. At the state of the art, laser-driven proton radiography already allowed to map electric and magnetic fields in plasmas with very high spatial and temporal resolution [65]. Laser accelerated protons can be exploited as a source of beamed neutron [62, 63] suitable for fast neutron radiography [74] and studies of impulsive damage of matter [75]. Due to its compactness and cheapness with respect to traditional techniques, a tabletop laser-induced accelerator could be of extreme interest in hospitals for in-situ production of PET isotopes or radio-pharmaceuticals [61]. Moreover, it could be exploited in Hadrontherapy [60]. However, it must be remarked that major improvements must be achieved. First of all, tunable 70-400 MeV/nucleon are required in radiotherapy. Even thought the current record is approaching the desired range (85 MeV protons were measured in [71]), the laser systems that can provide such extreme laser conditions are still rare and not suitable for “non research” applications. Besides, most of laser-induced acceleration techniques produce a broad spectrum and with a small fraction of the total charge accelerated to higher energies ($E \sim E_{max}$). A post processing of the beam would be required for most of the foreseen applications to obtain a narrower energy distribution.

In this chapter we offer a review of laser-induced ion acceleration, start-

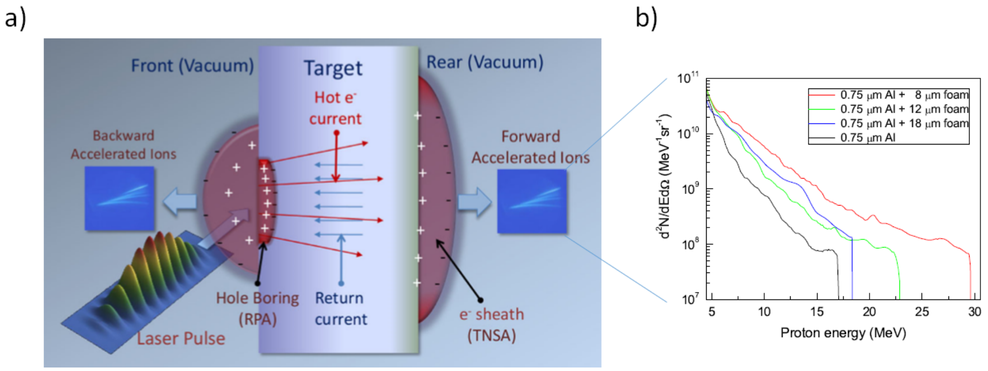

Figure 2.1: *a) Schematic representation of Target Normal Sheath Acceleration (TNSA) and Radiation Pressure Acceleration (RPA) (image from [58]). b) Typical ion spectrum of TNSA-ions.*

ing from the most studied and observed scheme called Target Normal Sheath Acceleration (TNSA) in section 2.1. In section 2.2 we provided an overview on emerging advanced TNSA techniques as well as alternative acceleration mechanisms.

2.1 Target Normal Sheath Acceleration (TNSA)

The first ion acceleration mechanism introduced is called *Target Normal Sheath Acceleration* (TNSA), proposed in 2001 by Wilks [76] to interpret the measurements in [66–68]. At the state of the art, it is the most studied and is the dominant acceleration scheme in experiments with intense lasers 10^{18} W/cm^2<I<10^{21} W/cm^2 interacting with micrometric (10^{-1}-10^{1} μm) solid targets. This topic of research is the central core of this PhD work, a detailed description is thus required. In subsection 2.1.1 we present the most iconic features of TNSA, identified in all experiments, as well as its most accepted parametric dependencies. The physical interpretation acknowledged to be accurate on the description of the physics at play is given in subsection 2.1.2. Finally, in 2.1.3 we provide a summary of laser induced electron heating which is proved to be fundamental on the onset on TNSA mechanism.

2.1.1 Experimental observations

In the typical TNSA experiment (fig. 2.1) an ultra-intense laser pulse is focused on a micrometric flat foil, usually at oblique incidence angle to avoid back-reflections which could damage the system. The laser beam couples with the formed plasma and induces the acceleration of ion bunches from both the front irradiated surface and the rear one.

The accelerated ions are typically collected with stacks of radiochromic films (RCF) or Thompson parabolae (TPS). The former are solid state detectors which exploit induced modifications of the crystalline structure to detect radiation. In particular, the polymerization results in a visible chromatic change. With stacks of RCFs the beam divergence, spot characterization and total accelerated charge can be sampled at different energies and the total spectrum can be reconstructed by interpolation. Thompson parabolae on the other hand use stationary electric and magnetic fields to split trajectories of ions with different charge over mass ratios. The signal can be then analyzed with a combination of CR39 films and CCD cameras, obtaining the energy spectrum. The coupled system TPS-CCD will be described with more detail in chapter 4.

The main advantage of RCF is that they offer an actual image of the ion beam transverse section, moreover it is easier to determine their maximum energy (the one related to the last impressed film). The major drawback is that the real spectrum can be only sampled at specific energies and different accelerated ion species can not be discriminated.

These diagnostics allow to detected accelerated ions, which can be measured from both the front [77–79] and the rear surface [80, 81]. However, better performances in terms of both energies and total accelerated charge are usually achieved at the non-irradiated one. In agreement with ref. [82], surfaces light-ions are more efficiently boosted than the bulk ones. Indeed, authors measured a strong proton signal using gold foils which significantly dropped after the removal of the hydrocarbons contaminants, usually present at the surfaces. Early 2000 experiments observed highly collimated ions ($\leq 20^\circ$ divergence angle) along the direction normal to the rear surface which formed bunches characterized by a near-circular spot, as seen in figure 2.2.a. Furthermore, all spectral analysis revealed a quasi-exponential spectra characterized by a sharp high energy cut-off. This is well shown in fig. 2.1, 2.2 and 2.4.b and is widely accepted to be a trademark of this acceleration scheme.

In latest years a lot of experimental efforts have been spent to link technique performances (e.g. the cut-off energy) to laser features such as intensity, energy, duration and spot size. A proper parametric scan is however a non trivial task due to the fact that in actual experiments these can not be varied independently.

The most natural strategy to investigate the role of the laser intensity,

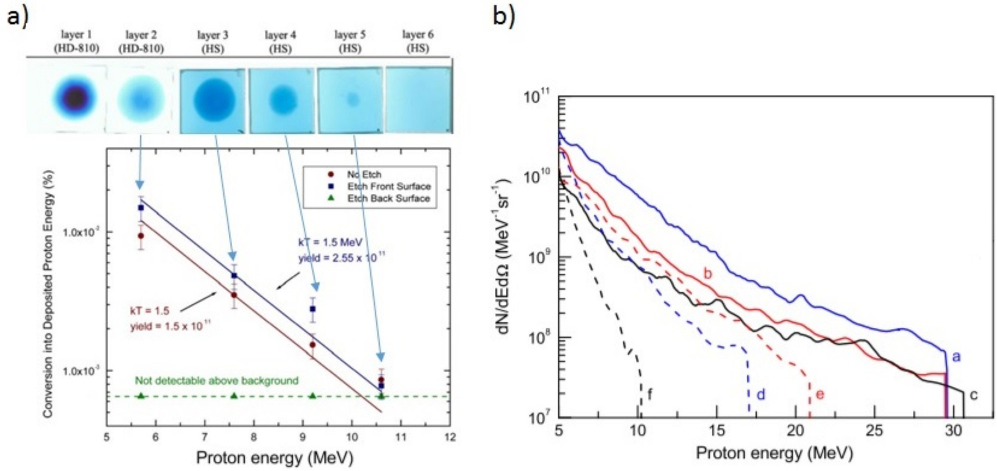

Figure 2.2: *a) Typical ion traces on a stack of radiochromic films and the reconstructed spectrum reported in [82]. b) Quasi-exponential spectra measured in TNSA experiments with Thompson parabole*

which is known to strongly influence ion acceleration, is to increase the beam energy, keeping fixed durations and focal spots. In references [83,84] a large collection of experimental results are reported. These have been obtained in a broad spectrum of laser intensities with $\mu\mathrm{m}^2$ spot sizes and pulse durations ranging from 40fs to ps.

As presented in figure 2.3.a, at high intensities (I>10^{17} W/cm^2) and 300fs-ps laser durations, the ion maximum energy scales as $\sqrt{I\lambda^2}$ ($I\lambda^2$ is laser irradiance), proportional to the well known ponderomotive scaling used to estimate the electron temperature that will be defined in section 2.1.3. Under these conditions, up to 10 % of the laser beam energy can be converted into fast ions. On the other hand, with shorter beams (tens of fs) the scaling is more favorable, being proportional to $I\lambda^2$, while the energy transfer is less efficient ($\sim$ 1%). The laser-to-ion energy conversion efficiency is indeed one of the most relevant drawbacks of TNSA with micrometric solid targets. To overcome this limitation, in the latest years a lot of theoretical an experimental efforts have been focused on the optimization of TNSA in terms of both efficiency and maximum energies achievable. Section 2.2 will cover some of the most recently proposed advances in TNSA.

Despite its unquestionable relevance in TNSA, the coupled laser intensity-energy parametric scan offers only a partial view of the acceleration process. Indeed, as seen in fig. 2.3.b, at a given laser power (or intensity) different results are expected with different pulse durations. As anticipated, this also reflects into a different scaling of the cut-off energy to the laser power itself. We also remark that, despite higher performances, $\sim$ ps and 10^2 J laser systems offer low repetition rates (few shots per day) and are extremely expensive. Indeed, shorter durations are more suitable in scenarios where higher repetition rates ($\sim$ Hz) are required.

In reference [85] a different path with respect to previous parametric campaigns have been adopted. The laser energy was kept fixed at 150 J, tuning the intensity by a fine control over the spot size (4-40 μm). Authors showed how the latter parameter is important in TNSA over wide conditions: higher maximum energies and total accelerated charge have been obtained with larger spot sizes (40μm), compared to the same intensity provided by more focused (8μm) and less energetic (3 J) beams.

Besides the above mentioned features, laser polarization as well as incidence angle are known to influence laser-plasma coupling and this reflects to TNSA performances [86–88]. As seen in figure 2.4.a, in experiments with flat foils, better results are achieved in P polarization (P-pol). It is generally accepted that this is due to the fact that in such interaction regime the normal to the surface component of the electric field leads to an efficient electron heating (see 2.1.3) and thus ion acceleration. This claim is also supported by the fact that in P-pol higher energies are measured at higher incidence angles (see figure 2.4.b).

It must be finally remarked that despite the efforts spent in the last decade a more solid experimental base is required in order to have a clear knowledge of actual parametric dependencies of TNSA. This would lead to a better control over the technique and arguably to advances in laser driven ion acceleration.

2.1.2 The acceleration scheme

The Target Normal Acceleration scheme in [76] provides a simple physical picture that allows to explain most of the observed features of laser induced ion acceleration with solid foils. Taking fig. 2.1.a as reference, an intense laser beam interacts with the target ionizing its surface. The beam couples with surface electrons heating them to energies up to MeVs. These so called *hot electrons* are injected into the target and generate strong current densities that can reach as high as $j_h = n_h v_h \simeq n_h c \sim 10^{12} A/\text{cm}^2$, being n_h and v_h the hot electron density and velocity.

This hot stream would generate strong electromagnetic fields that would ultimately hold back the electron flow. This noxious phenomenon can be

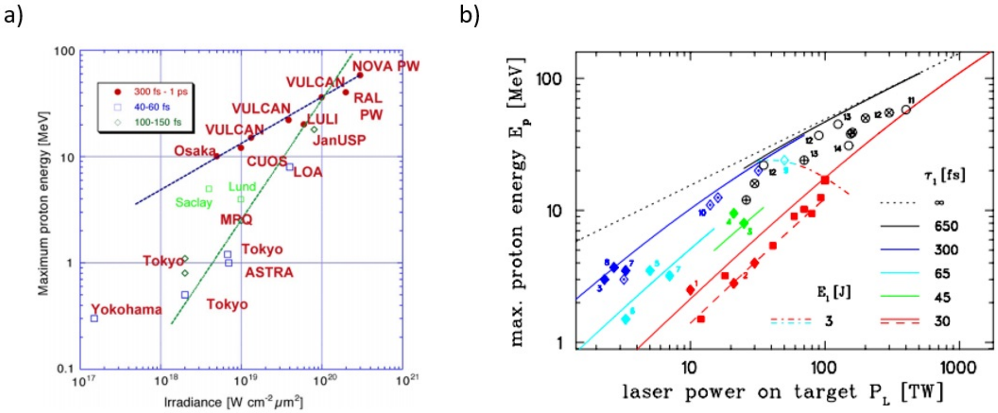

Figure 2.3: *a) Proton cut off energy as a function of the laser irradiance, adapted from [83]. b) Scaling law of the maximum proton energy with the laser power and pulse duration (color scale). Red squares refer to experimental results obtained at the Draco laser facilities. Filled diamonds stand for experiments performed with Ti:sapphire lasers of around 1 J energy while the open diamond represents a 5 J experiment at Janusp. The dotted diamonds show the results of an energy scan applying up to 10 J on the target and at LULI. Finally, the open circles are single shot results obtained at different Nd:glass laser facilities. (image from [89])*

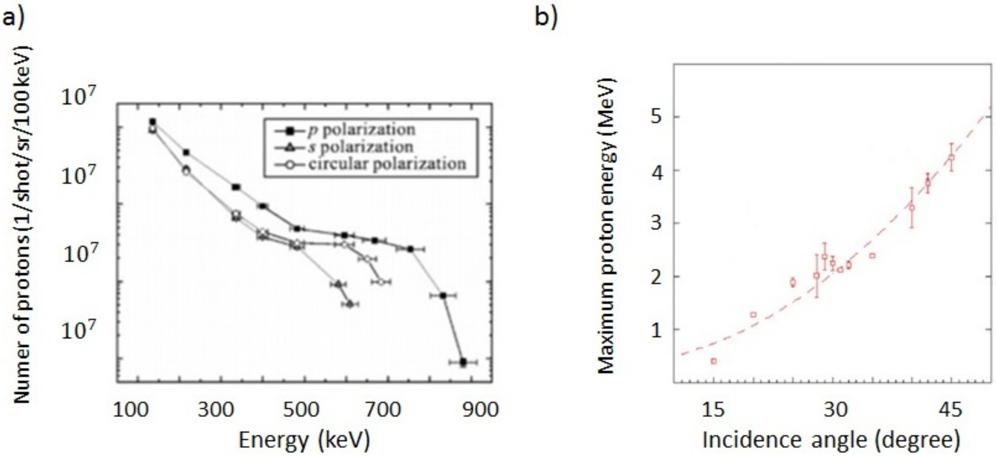

Figure 2.4: *a) Proton spectra for P-,S- and C- polarizations are shown (from [86]). b) Proton cut off energies at different incidence angles. The other laser parameters are kept fixed and the laser beam was P polarized (from [87]).*

prevented if a neutralizing return current is provided. The latter can be either be given by electrons in the conduction band in metals or by free electrons if the target is sufficiently ionized (condition easily fulfilled in laser-acceleration experiments). Typically only a small fraction of total electrons interacts directly with the laser beam (few %), the hot electron density is thus much lower than the back ground one ($n_h \ll n_c$). If we combine this condition with the total flow neutralization ($n_h v_h = n_c v_c$) it also follows that the return electrons are much less energetic that the hot ones ($v_c \ll v_h$) and are thus called *cold electrons*. Within tens of fs after the interaction electrons reach a quasi-equilibrium state, resulting in the typical spectra reported in fig. 2.5: a cold background electron population with a high energy maxwellian tail. In this work we define as "electron temperature" (T_h) the mean kinetic energy of the high-energy electrons.

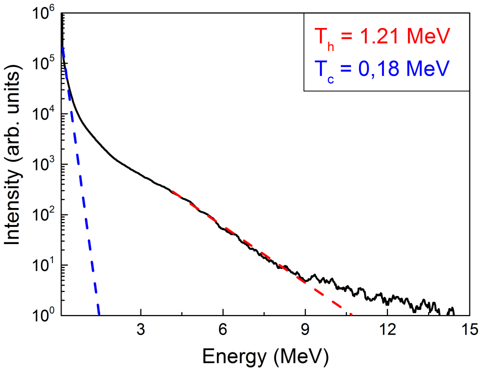

Figure 2.5: *Typical electron energy spectra obtained by numerical simulations. The distribution is approximated by two superimposed Maxwellian curves characterized by two distinct temperatures.*

Laser-heated electrons travel through the target and eventually expand in vacuum by thermal effects. A strong electrostatic (up to TV/m) field arises from the charge imbalance, holding most of escaping electrons which can be also reflected back into the target and further interact with the laser beam [90]. This sheath field is by construction peaked at the target-vacuum interfaces, being to a good approximation normal to them. A TV/m electrostatic field is able to ionize the target and is responsible of the ion acceleration. Light ions on the surfaces are in the most favorable position to be efficiently boosted.

The TNSA scheme is also able to explain the exponential spectrum with an energy cut-off observed in most of experiments. The most relevant drawback of TNSA with traditional micrometric solid targets is the low laser-to-ion energy conversion efficiency of 1-5 %. In the latest years a lot of theoretical an experimental efforts have been focused into the optimization of TNSA in terms of both efficiency and maximum energies achievable, section 2.2 will cover some of the proposed strategies.

In accord with the physical picture presented, TNSA can be divided in four sub-processes of utmost importance: electron heating, electron transport, sheath field generation and ion acceleration. In particular, a crucial part of this work is dedicated to the study of the fundamental link between electron heating and ion acceleration. Indeed, the sheath field must be strong enough to hold back hot electrons and can thus be determined with:

$$eE_s \simeq \frac{T_h}{L_s} \tag{2.1}$$

where T_h is the hot electron temperature and L_s the extension of the electron cloud. The latter can be approximated with the electronic Debye length $\left(\lambda_{De} = \sqrt{\frac{T_h}{4\pi n_h e^2}}\right)$, typically of the order of micrometers in TNSA experiments. We can finally roughly estimate the energy acquired by an ion in the sheath field as:

$$E_{ion} \simeq ZeE_s\lambda_D \propto T_h. \tag{2.2}$$

Eq. 2.2 allows us to introduce the importance of the hot electron temperature T_h in TNSA. This quantity is still subject of major theoretical and experimental discussions and is determined by the vast collection of heating mechanisms that can take place at different laser and plasma parameters. In 2.1.3 we will cover some physical scenarios relevant in TNSA experiments. It must be also remarked how electron density and divergence [59] as well as target properties [91, 92] are also crucial in TNSA. Finally we underline how the over-simplified model of Eq. 2.2 does not capture most of the physics involved. A review of more advanced and accurate theoretical models of TNSA is presented in chapter 3.

2.1.3 Electron heating

As anticipated in the 2.1.2, electron heating resulting from laser-plasma coupling is a fundamental stage in TNSA, affecting its performances. A better control and enhancement of this process would be of great interest also in the framework of TNSA optimization. Unfortunately, despite being an extensively studied topic, it is far from being sufficiently understood due to the extreme richness of laser-plasma physics. It is however certain

that different and possibly competing processes affect electron heating and their relative weights depend on experimental conditions.
It is accepted that target density as well as laser intensity are specially relevant to define different heating schemes. In particular, the critical density introduced in Eq. 1.43 determines three interaction regimes: *over dense*, *under dense* and *near critical.* We cover some of the main features of laser-plasma coupling relevant in laser ion acceleration applications.

Over-dense plasmas

This interaction regime is the most relevant for the typical TNSA scheme. Indeed, targets originally proposed for TNSA were flat foils which turn into strongly over-dense ($\gg 10^2\ n_c$) plasmas when interacting with intense laser beams. As demonstrated in section 1.2.4, electromagnetic waves can not propagate in over dense target and are reflected back. The interaction is thus confined in a small skin-layer ($\lambda_{sd} = \gamma c/\omega_{pe}$) at the irradiated surface. However, this is strictly true just in sharp edged plasmas. This condition is not always fulfilled since the temporal envelope of the laser beam may significantly alter the structure of the target [93]. Indeed, actual laser pulses exhibits complicated structures including pre-pulses and pedestal components which ionize the target and form the so-called *pre plasma.* The latter expands in vacuum at the sound speed $c_s = \sqrt{\frac{\gamma_i T_i + \gamma_e \gamma_e}{m_i}}$ due to thermal pressure, assuming an exponential density profile. Its typical scale length $L = c_s \tau_L$ (τ_L is the pulse duration) is relevant if long pulse durations ($\sim$ ps) or low contrast laser pulses are considered.
In this framework intense electromagnetic waves can propagate through the preplasma by relativistic transparency leading to a volumetric coupling [94].
Different dissipative mechanisms can take place at different experimental conditions, we here review some of the most relevant in TNSA with over-dense flat targets.

Collisional Heating

Charged particles oscillating in the electromagnetic field can undergo Coulomb collisions that may lead to a net energy depletion of the incident pulse energy. However some of these interactions can be ignored: ion-to-ion collisions occur on picosecond time scale and will not be considered in this work while electron-to-electron ones lead to the thermalization of their distribution function. In order to study the damping of an electromagnetic wave due to electron-ion collision we start from the non-relativistic linear momentum balance equation of the electronic fluid:

$$\begin{gathered} n_e\left(\frac{\partial \mathbf{v}_e}{\partial t}+\mathbf{v}_e\cdot\nabla\mathbf{v}_e\right)= \\ n_e\frac{e}{m_e}\left(\mathbf{E}+\frac{\mathbf{v}_e}{c}\times\mathbf{B}\right)-\frac{1}{m_e}\nabla P-\frac{\partial}{\partial t}n_e\mathbf{v}_e\bigg|_{ei,coll} \end{gathered} \tag{2.3}$$

the last term describes the evolution of the electron fluid momentum due to electron-ion collisions. In first approximation we can express it as:

$$\frac{\partial}{\partial t}n_e\mathbf{v}_e\bigg|_{ei,coll}=\nu_{ei}n_e\mathbf{v}_e \tag{2.4}$$

where ν_{ei} is the collision frequency. If we linearize Eq. 2.3 we obtain:

$$\frac{\partial \mathbf{v}_e}{\partial t}=-\frac{e}{m}\mathbf{E}-\nu_{ei}\mathbf{v}_e \tag{2.5}$$

Without loss of generality, we consider a harmonic perturbation and we finally find:

$$\mathbf{v}_e=-\frac{ie\mathbf{E}}{m(\omega+i\nu_{ei})} \tag{2.6}$$

The plasma current density can be easily expressed as:

$$\mathbf{J}=-en_e\mathbf{v}_e=\frac{i\omega_{pe}^2}{4\pi(\omega+i\nu_{ei})}\mathbf{E} \tag{2.7}$$

In a linear theory the current density **J** and the electric field **E** are linked by the conductivity σ by Ohm's law $\mathbf{J}=\sigma\mathbf{E}$. We can then use Maxwell equations to retrieve the dispersion relation:

$$\omega^2=k^2c^2+\omega_{pe}^2\left(1-\frac{i\nu_{ei}}{\omega}\right) \tag{2.8}$$

In Eq. 2.8 a damping term ν_{ei}/ω is introduced. It is indeed fundamental to estimate the collision frequency in order to evaluate the energy losses of electromagnetic waves due to e-i collisions. However, ν_{ei} depends on the distribution functions of both ions and electrons and thus it is dependent to the system evolution itself.

In the framework of a classical scattering theory this frequency can be expressed as:

$$\nu_{ei}\simeq 4\pi Zn_e\frac{(eq_i)^2}{m_e^2v^3}ln\Lambda\propto n_eT_e^{-3/2}ln\Lambda \tag{2.9}$$

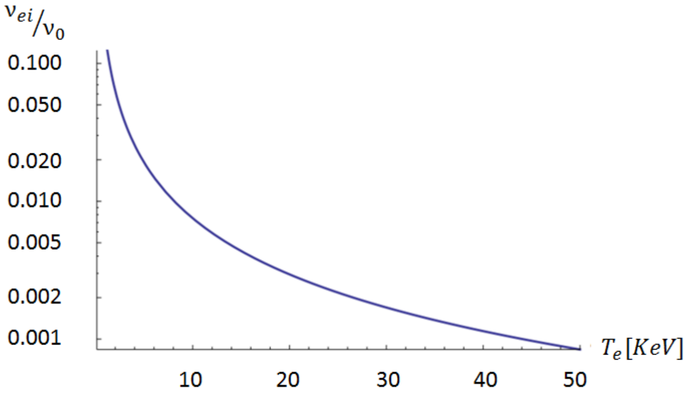

Figure 2.6: *Electron to ion collision frequency (ν_{ei}) normalized to the wave frequency ν_0 as a function of the electron temperature.*

where q_i and Z are the ion charge and atomic number, n_e is the electron density. The Coulomb logarithm $ln\Lambda$ takes into account the minimum and maximum impact distances [95].

$$ln\Lambda = ln\left(\frac{b_{max}}{b_{min}}\right) = ln\left(\frac{\lambda_{De}T_e}{q_i e}\right). \tag{2.10}$$

We remind that λ_{De} is the electronic Debye length already defined. In figure 2.6 is represented Eq. 2.6 as function of the electron temperature. As the latter grows collisional heating becomes less effective. In typical experiments with intense laser ($I > 10^{18}$) the mean collision time ($\propto 1/\nu_{ei}$) is order of magnitudes larger than the actual pulse duration. In this framework non-collisional mechanisms must thus be taken into account.

Resonance absorption

Resonance absorption is a heating effect which can take place if a sufficiently long under-dense pre plasma ($L \geq \lambda_L$) is provided. As presented in figure 2.7, the electromagnetic wave propagates through the pre plasma and is reflected back as it reaches the electron density $n_e = n_c cos^2\theta$ (θ is the incidence angle). Most of the wave is then back-reflected except for a small exponentially-evanescent component. If a component of the latter oscillates along the direction of the density gradient ($\mathbf{E} \cdot \nabla n_e \neq 0$), plasma waves at the critical density can be excited. These collective modes can be consequently damped by collisions, Landau-damping or wave-breaking. The analytical model described in [96, 97] was proven to be in good

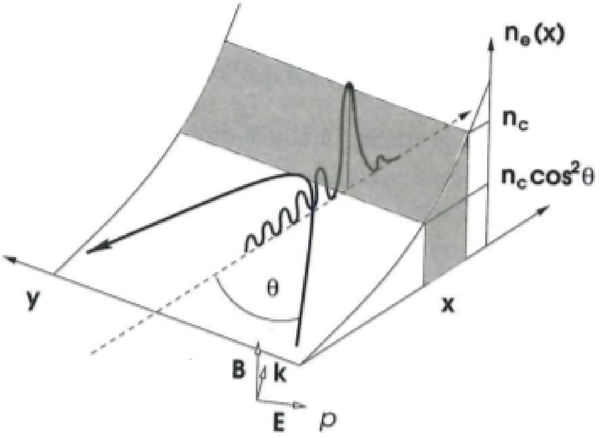

Figure 2.7: *A plane wave interacting with an exponentially shaped pre plasma. The $\hat{x}$ component of the electric field excites a plasma wave at the critical density which gives rise to a strong electrostatic field E_x [26].*

agreement to numerical simulations ([97–99]) which reported a dependence of the electron temperature to the laser irradiance scaling as: $T_e \propto (I\lambda_L^2)^{0.3-0.4}$. This heating mechanism efficiently takes place with long laser pulses (>ps) and long plasma gradients ($> \mu$m). However, numerical results presented in [100] suggested how resonance absorption could be relevant also at high laser intensity ($I > 10^{18} W/\mathrm{cm}^2$) with longer laser pulses and thinner pre plasmas.

Brunel Effect

Plasma waves can not be resonantly excited when the oscillation amplitude exceeds the pre plasma length ($v_{osc}/\omega > L$), a condition easily reached with ultra-intense short pulses interacting with flat targets. Firstly discussed by Brunel in 1987 [101] and extensively studied in the last decade [26, 102, 103], *Brunel effect* is one of the dominant heating mechanisms in ultra intense laser interaction with micrometric plain solid targets (SLT). The physical picture is rather straightforward: electrons in the skin layer are extracted in the vacuum in the first quarter of the laser cycle. Half of them (see [102]) fall back in the first half period due to the electrostatic field generated by charge displacement against the pulling force of the laser field. Most of the remaining electrons are ef-

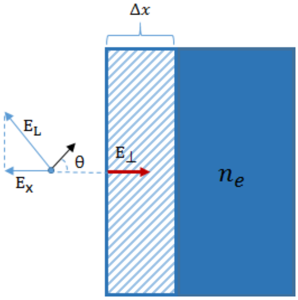

Figure 2.8: *Schematic representation of the capacitor-like model used in the Brunel description.*

fectively boosted and re-injected by the combined effect of the laser and electrostatic field. Due to the vanishing electromagnetic field inside the target, electrons cannot be further dragged back in the vacuum and this leads to a net energy transfer. It is evident that a strong normal electric field is required for an effective Brunel heating which is thus suppressed at normal incidence and in S-polarization. The capacitor-like model represented in figure 2.8 assumes a charge sheet which oscillates by the effect of the normal component of the laser electric field (magnetic fields are not included). If we consider an electromagnetic wave interacting with a perfectly reflecting flat surface the normal component of the electric field will be:

$$E_\perp = 2E_L sin\theta \tag{2.11}$$

where θ is the incidence angle. Electrons will be dragged into the vacuum while the electrostatic field generated by charge separation matches $E_\perp$. In the framework of a moving capacitor plate, this relation will hold:

$$E = E_\perp = 4\pi 3\sigma_e \ \rightarrow \ \sigma_e = \frac{2E_L sin\theta}{4\pi e} \tag{2.12}$$

having defined $\sigma_e = n_e \delta x$ as the surface charge density. If we assume that electrons re-injected in the target at $v = 2v_{osc} sin\theta$ are lost as they cross the surface, the absorption efficiency will be:

$$\eta_a = \frac{I_{abs}}{I_L} = \frac{4}{\pi} a_0 \frac{sin^3\theta}{cos\theta} \tag{2.13}$$

If the electron are assumed to be injected at the perpendicular quiver velocity, the electron temperature can be estimated:

$$T_e(Brunel) = mv_{osc}^2 sin^2(\theta) \propto I\lambda^2 \tag{2.14}$$

This relation however greatly overestimates the scaling of the electron temperature to the laser intensity measured in experiments and in numerical simulations [26].

If a relativistic description and a non perfect reflective foil are considered we obtain this more general relation for the interaction efficiency:

$$\eta_a = \frac{1}{\pi a_0} f \left[\left(1 + f^2 a_0^2 sin^2\theta \right)^{1/2} - 1 \right] \frac{sin\theta}{cos\theta} \tag{2.15}$$

where f is the field amplification factor (f = 2 for perfect reflection on a flat surface). Eq. 2.15 will be discussed with more detail in chapter 5.

$\mathbf{j} \times \mathbf{B}$ heating

Another heating mechanism relevant with intense laser beams is described by the $\mathbf{j} \times \mathbf{B}$ model [104–106]. Similarly to Brunel, electrons are directly accelerated by an electromagnetic field incident on a sharp-edged solid target. The basic difference is that the the driving force is given by the oscillating component of the $\mathbf{j} \times \mathbf{B}$ force:

$$e\frac{\mathbf{v}}{c} \times \mathbf{B} = \frac{e^2 \nabla_x A^2(x)}{4 m_e \gamma c^2} \left(1 + \frac{1-\epsilon^2}{1+\epsilon^2} cos2\omega t \right) \tag{2.16}$$

where ϵ is the eccentricity of the elliptically polarized wave ($\epsilon = 0$ linear polarization $\epsilon = 1$ circular polarization). The right hand side of Eq. 2.16 exhibits two terms: a secular and an oscillating component. The latter is responsible in electron heating and is suppressed in circular polarization (i.e. ϵ=1 in C-pol). Indeed, $\mathbf{j} \times \mathbf{B}$ is predicted to be negligible for circularly polarized laser pulses. Moreover, since this heating effect is due to the *non-linear* term of Lorentz force, it is expected to be dominant at higher intensities (I > 10^{18} W/cm^2).

If we recall results in Eq. 1.40, the longitudinal dynamics is influenced by the ponderomotive potential. The net effect of this potential can be associated to an effective temperature, given by:

$$T_e = mc^2(\gamma - 1) = m_e c^2 \left(\sqrt{1 + a_0^2/2} - 1 \right). \tag{2.17}$$

This *Ponderomotive scaling*, firstly proposed by Wilks in [105] is a widely used scaling law in laser-plasma interaction.

Other heating mechanisms

In an overdense plasma the electric field decays over distances of the order of the skin depth ($L_s = c/\omega_{pe}$), however, it can be still intense enough to induce the electron quiver that can be damped by Coulomb collisions.
We define $\lambda_{Te} = v_{Te}\omega$ as the electron excursion distance in a laser period due to the thermal velocity which can give an estimation of the distance required to thermalize oscillations due to the electric field. At the beginning of the laser-plasma interaction $L_s \gg \lambda_{Te}$, thus, the formed plasma is locally thermalized. When the electron temperature rises, the collision frequency ν_{ei} drops and electrons can oscillate in the skin layer without undergoing collisions. In this framework two interaction mechanisms can be highlighted. If $\lambda_{Te} \gg L_s$ oscillating electrons can escape the skin layer leading to an energy transfer from the laser beam to the electronic population. This physical phenomena is called **Anomalous skin effect** [107]. In the opposite limit $\lambda_{Te} \ll L_s$ the electrons are trapped in the skin depth, however, can be still accelerated by the ponderomotive force or by the surface charge separation, this is called **Sheath inverse bremsstrahlung** [108].

Under-dense and near-critical plasmas

Laser interaction with under-dense and near-critical plasmas covers an extremely vast and still unexplored topic of research. Low-density plasmas can be typically created from gas-jets or low density material ionization. Intense laser beams can propagate through their volumes, exciting different collective modes and giving birth to complex non-linear effects that can lead to efficient plasma heating. Collective waves can be induced by the effect of the ponderomotive force as anticipated in 1.2.4: the ponderomotive force couples with charge density fluctuations to effective pump plasma waves.
A basic approach to the problem is to consider a relativistic, non collisional, cold two fluids plasma. Indeed, a rich variety of physical phenomena can be studied coupling the continuity equation, linear momentum Eq. 1.37 and Maxwell relations.

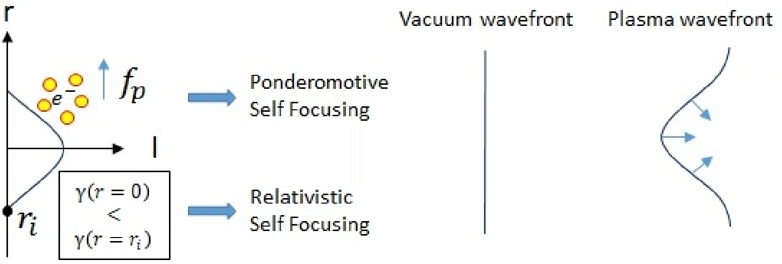

Figure 2.9: *Relativistic and ponderomotive self focusing in an underdense plasma.*

We here start from the **Self focusing**, a non-linear effect which, despite not being a heating mechanism, is extremely relevant in plasma physics [109–112]. Taking fig. 2.9 as reference, as an intense laser pulse propagates into a plasma it modifies its refractive index, causing a higher value in the center of the laser beam, where the laser intensity is peaked, inducing a feedback loop that focuses the laser even more. In a plasma there are three types of self-focusing: relativistic, ponderomotive and thermal. The latter requires the hydrodynamical expansion of the plasma which occurs on picosecond time scales. This last scenario will not be covered in this work, since sub-picosecond laser pulses are studied. In the **Relativistic** case, non linear effects shift the plasma frequency due to the higher inertia of energetic electrons. This effectively modifies the plasma dispersion relation as stated in Eq. 1.42 and, consequently, its refractive index ($\eta = \eta(r)$). The transverse variation of the refractive index ($d\eta/dr < 0$) acts as an effective plasma lens leading to a higher laser peak intensity.
Self-focusing can also be induced by the effect of the transverse ponderomotive force which pushes electrons away from the region where the laser beam is more intense, therefore increasing the refractive index and inducing a focusing effect. The **Self focusing** can lead to a growth of the laser peak intensity of several orders of magnitude [113] which can further enhance heating effects.
Eq. 1.37 can be used to study the **wakefield generation**. As already presented in section 1.3, the ponderomotive force associated to an intense laser pulse can induce collective electron plasma waves. These oscillations are related to strong longitudinal electrostatic fields that can be pumped by the electromagnetic wave. The plasma waves eventually breaks, accelerating electrons in phase with it.
Besides these non linear effects, strong electromagnetic fields inside a low density plasma can induce plasma instabilities. The basic principle is straightforward: the laser beam may excite plasma waves, the pondero-

motive force associated to the total field can further support the growth of the perturbation leading to a feedback loop. The growing waves can be eventually damped by collisions, Landau damping or, eventually, wave breaking leading to a strong plasma heating.

In **Raman instability** an incident electromagnetic wave decays into scattered electromagnetic and an electron plasma wave. The scattered beam can further pump the plasma and induce the instability. This phenomena can occur only if strict frequency and wave-vector matching conditions are met:

$$\begin{cases} \omega_0 = \omega_s + \omega_{pe} \\ \mathbf{k}_0 = \mathbf{k}_s + \mathbf{k}_{pe} \\ n_e \leq n_c/4 \end{cases} \tag{2.18}$$

where $\omega_0 - \mathbf{k}_0$ and $\omega_s - \mathbf{k}_s$ are the frequencies and wave vectors of the incident and reflected wave respectively. The **Two plasmon instability** shares the same basic principle, with the exception that in this case the electromagnetic wave decays in two electron plasma waves which can constructively interfere with themselves. This instability is particularly relevant in cold plasmas with $n \simeq n_c/4$. In these instabilities part of the incident beam energy is transferred to plasma waves and, as they damp, they heat the plasma. Electron plasma waves can exhibit extreme phase velocities, thus Raman and two plasmon instabilities may trap electrons and boost them to relativistic energies and can further heat the medium.

In **Brillouin instability** the incident wave decays into a scattered one and an ion acoustic wave. As previous cases, matching conditions are required:

$$\begin{cases} \omega_0 = \omega_s + \omega_{ac,i} \\ \mathbf{k}_0 = \mathbf{k}_s + \mathbf{k}_{ac,i} \\ n_e \leq n_c \end{cases} \tag{2.19}$$

Due to the much lower frequencies of the acoustic waves with respect to the electron plasma waves, the matching conditions are fulfilled at higher plasma densities ($n \simeq n_c$) with respect to Raman instability. Most of the incident wave is scattered, this instability can be particularly noxious if a spatially controlled laser absorption is required. Finally a relevant effect to be presented is the **Filamentation instability**, it corresponds to the growth of a local density perturbation in the plane orthogonal to the electromagnetic wave propagation axis. The physical picture is similar to the one of the ponderomotive self focusing: if an initial charge density perturbation is provided the laser beam will be focused into the low-density

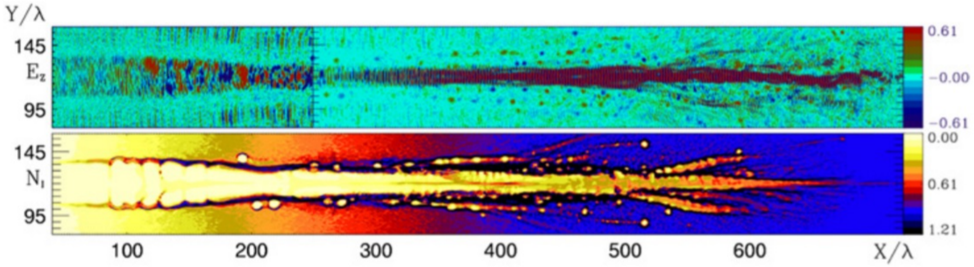

Figure 2.10: *The E_z component of the electric field and the ion density N_i (color map) as a function of the spatial coordinates. Plasma channels and electromagnetic filaments are evident [114].*

regions. The ponderomotive force will further drill plasma channels which consequently drive the laser beam [114, 115]. The net effect is the laser beam splitting in smaller high intensity filaments as in fig. 2.10.

A fine control over collective modes excitations and laser energy deposition is overwhelmingly challenging in actual experiments. This is especially relevant in intense pulse interaction with near-critical plasmas generated from nanostructured targets which might exhibit inhomogeneities on sub-micrometric spatial scales. Indeed, matching conditions are reliant on the local dispersion relation and, thus, inhomogeneities limit the region over which collective modes can be resonantly excited. If we suppose that these conditions are met in a given location, moving away from it will cause the growth of a phase mismatch $\phi(\mathbf{r})$. The resonant coupling is broken if a significant phase shift develops. The typical interaction scale (l_{int}) can be estimated as $\int_0^{l_{int}} \phi(\mathbf{r}) d\mathbf{r} \sim 1/2$ and will be dependent on the plasma inhomogeneities. In order to obtain an efficient coupling l_{int} must be long enough to support the collective mode in exam. This condition can be hard to be fulfilled in nanostructured targets characterized by significant variations of the local plasma density over short spatial scales ($<\mu$m).

Beside collective effects, electrons can also be efficiently boosted by the direct effect of the electromagnetic wave [116].

In the **Leading edge depletion** an ultra-intense ultra-short laser pulse can promptly accelerate electrons along its propagation direction to relativistic energies ($p \sim a_0^2$). As the laser beam propagates through the target its group velocity decreases, electrons finally overcome the laser beam depleting its energy [117, 118].

The **Transverse Ponderomotive Acceleration** is a physical effect coupled with the ponderomotive self focusing [119, 120]. The transverse pon-

deromotive force, not only creates plasma channels, but can also accelerate electrons which are expelled from the plasma channel with energies comparable to the ponderomotive potential ($p \sim a_0$).
Despite being still an open topic of research in the plasma physics community, it is widely accepted that near critical targets could greatly boost the laser energy absorbed by the plasma [121, 122] and thus could be promising for enhancing ion acceleration as it will be discussed in 2.2.1.
In conclusion we have shown several of the main physical effects that can influence plasma heating and laser propagation under different experimental conditions. It must be remarked that due to the richness of the physics involved this is still a challenging and fertile topic of research.

2.2 Evolution of laser induced ion acceleration

The first experimental observations of laser induced ion acceleration were achieved using simple flat solid targets (SLT). In section 2 we highlighted how most of potential applications would require better performances, in particular, in terms of ion maximum energy and total accelerated particles. Reaching and overcoming the 100 MeV/nucleon milestone would be of crucial importance especially in radiotherapy. Such energies could be achieved in the framework of traditional TNSA, with multi-PW facilities. However these structures are extremely expensive, still under development and can not be expected to be used for mass-applications in the short-medium time period. To overcome current limitations of the laser technology, a great amount of theoretical as well as experimental effort has been spent into the development of advanced TNSA schemes as well as on the study of different laser-induced ion acceleration techniques.

2.2.1 Advanced TNSA

One of the main drawback of TNSA with SLTs is the rather low laser-to-ion energy conversion efficiency ($\eta_{Li} < 10\%$). A better laser-plasma coupling would indeed guarantee better performances. In section 2 we showed how in TNSA the laser directly heats electrons which convert part of their energy to the accelerated ion population. If ultra-short laser pluses (<ps) are considered, electron heating would occur on a different time scale than ion dynamics. The two processes can be studied separately. We can define the electron heating efficiency (η_{Le}) and electrons-to-ions (η_{ei}) efficiency.

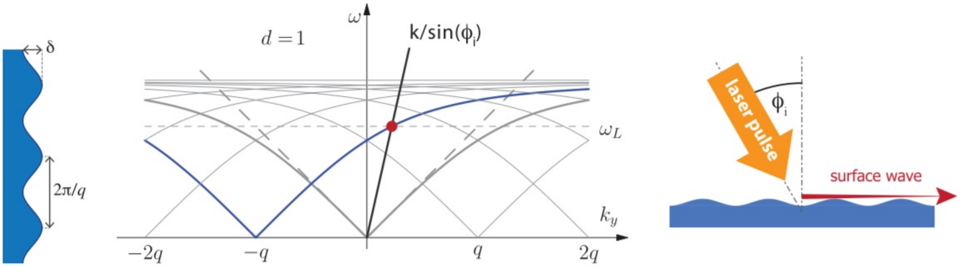

Figure 2.11: *Schematic representation of surface plasmon excitation. The dispersion relation shows the resonance condition, met with gratings targets at oblique incidence.*

These will be naturally linked to the acceleration efficiency by:

$$\begin{cases} \eta_{Le} = \frac{E_{ele}}{E_L} \\ \eta_{ei} = \frac{E_{ion}}{E_{ele}} \\ \eta_{Li} = \frac{E_{ion}}{E_L} = \eta_{Le} \cdot \eta_{ei}. \end{cases} \tag{2.20}$$

The acceleration efficiency can be, thus, enhanced either increasing the laser-plasma coupling or the electrons-to-ions conversion. The latter however can naturally reach high values (up to 50%) and can not be straightforwardly controlled since it would require a proper manipulation of the hot electron plasma flow and expansion.

The most natural solution to improve TNSA is given by a better laser-plasma coupling. In agreement with recent numerical works [123, 124], a considerable room for improvement in interaction optimization is achievable. This is mostly due to the modest conversion efficiency η_{Le} (<20 %) with traditional SLTs. The physical constraint for this quantity is given by the low fraction of plasma electrons that can be heated with $j \times B$ heating or Brunel effect.

A possible solution proposed in the latest years is to induce surface plasmons excitations [125], collective electron oscillation confined in a thin layer in a metal-dielectric interface. However, it is well known that, due to their dispersion relation, these superficial modes can not be efficiently pumped with a flat vacuum-target interface. As presented in 2.11, among the proposed strategies to overcome this hurdle, periodic modulation of the target surface has proven suitable in ultra-intense laser interactions [88, 109, 126].

In ref. [88] authors reported an increase of the accelerated proton maximum energy with respect to SLTs of a factor 2 at resonance incidence angle.

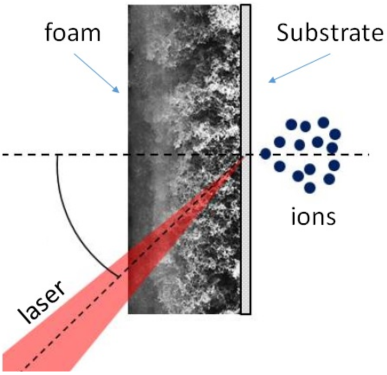

Figure 2.12: *Enhanced TNSA with foam attached targets.*

Nanostructured surface targets have been extensively studied. In recent works, a nano-sphere layer [127, 128] and hollow micro-cones [129] over solid substrates allowed better laser-plasma coupling and, as a consequence, higher ions energies.

These techniques require an ultra-high laser contrast and short pulses durations: long pulses ($\sim ps$) or intense pre-pulses ($I > 10^{12} W/\mathrm{cm}^2$) can blow-away the surface nanostructure before the interaction with the peak of the laser beam takes place. Another advanced TNSA scheme exploits multi-layered targets (MLT) to greatly enhance laser absorption. These targets are composed by a low-density material (foam) deposited over a micrometric flat foil and have been studied both numerically [123] and experimentally [130]. These foams are characterized by a nanostructured porous structure and turn into near-critical plasmas when fully ionized. As seen in figure 2.12, the laser beam can travel through the foam volume being reflected by the solid substrate. The combined volumetric and superficial interaction (in the foam and in the substrate, respectively) leads to an efficient laser absorption which can be exploited to effectively accelerate ions if proper laser and target conditions are met. An important part of this work is dedicated to this specific advanced-TNSA scheme, a more detailed description will be given in chapters 4 and 5.

We finally present a different strategy to improve TNSA given by *mass limited targets*: micrometric sized foils or micro-spheres [131–133]. Traditional TNSA foils can be considered as infinite slabs since their transverse dimension ($\sim mm$) are typically orders of magnitude greater than the distances traveled by electron interacting with the electromagnetic wave ($\sim \mu m$). Mass limited targets, on the other hand, exploits hot electrons

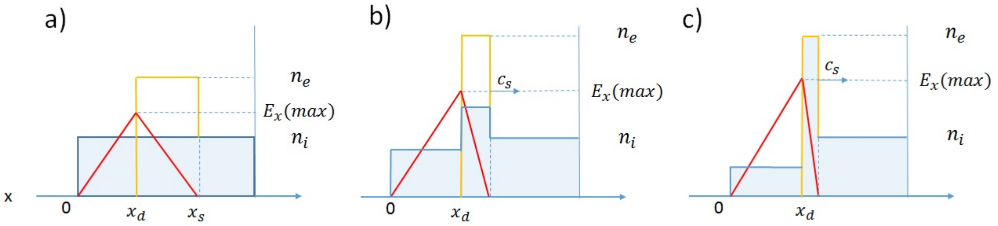

Figure 2.13: *Monodimensional representation of the temporal evolution of RPA.*

reflections at the lateral surfaces to create a denser electron cloud with respect to SLT case. A higher electron density creates stronger electrostatic fields and, thus, enhanced ion acceleration.

2.2.2 Other acceleration schemes

In this section several alternative acceleration schemes with respect to TNSA will be briefly presented. The so called **Radiation Pressure Acceleration** (RPA) is an acceleration mechanism which gained considerable popularity in latest years. It exploits the direct effect of the ponderomotive force to boost ions on the irradiated surface of a solid foil (see figure 2.1). RPA can be achieved at high laser intensity ($I > 10^{22} W/\mathrm{cm}^2$) and to be observed electron heating must be suppressed, otherwise TNSA ions cover the RPA component of the accelerated spectrum. As presented in section 2.1.3, electron heating with SLTs is dominated by Brunel effect and $j \times B$ heating which can be strongly quenched using circularly polarized (C-pol) laser pulses at normal incidence. As presented in figure 2.13.a, the secular component of the ponderomotive force 1.25 pushes electrons into the target leaving a charge depleted region. An electrostatic field rises 2.13.b to balance the radiation pressure inducing charge imbalance which accelerates ion bunches as in figure 2.13.c. The electromagnetic wave can further drill into the target and push the high density ion layer which is modeled as a moving piston. In the approximation of elastic collision with an infinite mass moving wall, ions can acquire up to 2 times its velocity. This process is called **Hole Boring RPA**.

The drift velocity of the ion layer can be estimated balancing the radiation pressure and the ion fluid linear momentum [58]. The maximum energy achievable with RPA is thus given by:

$$
\begin{aligned}
E_{max} &= 2m_p c^2 \frac{\Pi}{1+2\sqrt{\Pi}} \\
\Pi &= \frac{I}{m_i n_i c^3}
\end{aligned}
\tag{2.21}
$$

Numerical and theoretical works predict a narrower proton energy spectrum with respect to TNSA [134].
Hole Boring RPA scheme holds if the piston does not break through the rear surface, condition easily fulfilled with micrometric targets. With thinner targets ($\sim$ 10 nm), the foil can be continuously accelerated by the incoming laser beam. The acceleration scheme known as **Ligh Sail RPA** can be pictured as a perfect reflecting mirror boosted by an intense laser beam [135, 136]. This technique is extremely appealing since it could potentially lead to extreme energy conversion and acceleration performances. Despite the promising theoretical and numerical predictions an experimental observation of RPA is still challenging since, at available intensities $I < 10^{22} W/\mathrm{cm}^2$, parasitic TNSA effects overshadow RPA which should be dominant at higher intensities. Hints of light sail RPA were recovered in several experiments with 5-20 nm thick foils [137–139]. We finally remark how a novel RPA concept have been proposed in [73], it exploits the laser self focusing in a micrometric near critical layer formed by carbon nanotubes in order to enhance the peak intensity of a C-pol laser beam by a factor 10. This allows to increase the relative effect of RPA with respect to TNSA, confirmed by the peculiar accelerated spectrum.
Another proposed acceleration mechanism is **Collisionless shock acceleration** (CSA) [140, 141] which exploits a laser-pressure induced electrostatic shock-wave in a low density plasma to accelerate ions. Similar to hole-boring RPA, CSA promises a better scaling of the maximum energy to the laser intensity with respect to TNSA and a narrow accelerated spectrum. The quasi-monoenergetic $\sim$ 20 (1% energy spread) MeV protons measured in [142] have been attributed to the shock-waves induced into a gas jet by a train of CO_2 laser pulses, on the basis of numerical simulations as well of the theoretical model.
Finally must be mentioned an emerging acceleration technique called **Break Out Afterburner** (BOA), numerically studied in [143–145]. BOA takes place in two phases. The first stage is traditional TNSA with solid foils and electrons are heated by mechanisms presented in 2.1.3. As the electron population gains energy, it expands and the relativistic skin depth ($\lambda_{SD} = \gamma c/\omega_{pe}$) grows at the same time. If the target is sufficiently thin

(tens of nm) it may experience relativistic transparency. In the second phase of BOA the remaining part of the laser pulse penetrates into the target, inducing a forward electron beam due to the ponderomotive force. This beam is unstable to relativistic Buneman instability, which rapidly converts the electron energy into ion energy. This mechanism should accelerate ions to much higher energies than traditional TNSA, however strong experimental evidences of BOA are still lacking.

3

Theoretical and numerical description of the TNSA mechanism

Coherently with the previous chapter, most of the experimental activity regarding laser induced ion acceleration was performed under operating conditions where TNSA is the dominant scheme. In this framework, non experimental approaches are indispensable to interpret and investigate its complex physics, strongly dominated by non-linear effects. The basic purpose of these methods is to provide reliable predictions of experimental results, a better control over the technique and, arguably, lay the foundations for future researches. At this regard, in this work we adopted a combined study given by:

- **Analytical models** are of extreme interest in order to unfold the fundamental physics governing the system studied. TNSA theoretical models usually split the whole process in sub-processes easier to be modeled. Their main purpose is to identify the most relevant physical mechanisms as well as to provide reliable scaling laws to estimate key quantities (e.g. cut off energy, plasma temperature etc.) rather than achieving a perfect accord with experiments.

- **Numerical simulations** are extraordinarily powerful tools to achieve a better understanding of the physical processes at play. They provide information on quantities (e.g. phase space and fs-nm resolved EM fields) not measurable in actual experiments. The objective of numerical codes is to accurately reproduce the physical system, however, special care should be taken if a quantitative agreement with experimental results is desired. The main drawback of this approach is that numerical simulations can be computationally expensive ($\sim$

40k CPU hours for each 3D simulation performed in this work). The total amount of CPU hours available sets a constraint over the total number, maximum resolution, size and temporal duration of simulations performed.

In this chapter we will cover the above mentioned approaches. In section 3.1 we present some of the most studied TNSA analytical models with a particular focus on the one which will be adopted in this work. In section 3.2 we will describe some the most exploited numerical approaches, in particular Particle In Cell codes (PIC) which are of key interest in plasma physics. Finally, in section 3.3 we will list the open issues of TNSA which are covered in this work.

3.1 Analytical modeling

In section 2.1 a simple model allowed to estimate the sheath field which balanced the thermal pressure of hot electrons as well as the ion cut-off energy $E_{max} =\simeq ZeE_s\lambda_D \propto T_h$. If Eq. 2.2 is coupled with Eq. 2.17 (the ponderomotive scaling for the T_h) we retrieve a dependence of $E_{max} \propto I^{0.5}$. This scaling was also observed in several experimental works with long ($\sim$ ps) laser pulses [59, 146, 147], nevertheless proved to be pessimistic with shorter ones ($\sim$ tens fs).

Indeed, even an extremely basic approach is able to provide useful information regarding the acceleration scheme. In the latest years much more accurate analytical models have been proposed to gain a better understanding of the physical system. Consistently with the introduction of this chapter, TNSA is an extremely complex process, for a theoretical study several simplifications are thus required.

First of all, in order to tackle the problem it is useful to divide the mechanism into more fundamental sub-tasks: electron heating, electron transport, sheath field generation and ion acceleration. In the framework of sub-picosecond beams, laser-coupling occurs on a different time scale with respect to ion acceleration which requires hundreds of fs to take place. A reasonable choice is to focus the attention just on the modeling of the sheath field, treating the first stages of TNSA as fixed boundary conditions.

Analytical models, thus, deal with targets already in the plasma state which can be divided in four main species. As seen in section 2.1.2, electrons can be split into *hot* and *cold* ones. The former are directly heated by the laser beam and characterized by much higher temperature than the

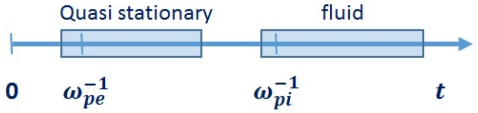

Figure 3.1: *Typical time scales of different classes of physical models.*

latter $T_h \gg T_c$. In most of cases relevant for laser-induced ion acceleration just a small fraction of total electrons are directly boosted by the beam so that their density is typically much lower than the cold background ($n_h \ll n_c$). Ions on the other hand are usually divided between *bulk* and *surface* ions. In accord with the TNSA scheme, surface ions are accelerated more efficiently than bulk ones and are usually composed of light ions (Hydrogen and Carbon) contaminants.

A commonly adopted strategy is a 1D geometry to greatly reduce the complexity of the system. The spatial coordinate considered is usually the one defining the normal to the target, thus homogeneous in the transverse plane. This assumption also rules magnetic effects out of the dissertation, only the electrostatic response is considered.

Theoretical models can be divided in three main branches, defined by the different time scales considered. Two time scales of utmost interest in TNSA are given by the dynamics of hot electrons and background ions, respectively. The former can be estimated with the inverse of the electron plasma frequency $\tau_{e,hot} \propto \omega_{pe}^{-1} \sim 10^1$ fs and is orders of magnitude smaller than the latter ($\tau_i \propto \omega_{pi}^{-1} \sim$ ps). Due to this fact, the three families of theoretical descriptions can be outlined:

- The *fluid* models consider the temporal evolution of both ions and electrons and are reliable for time scales longer that the ion dynamics $t > \tau_i$ (fig. 3.1). Their basic principle is to consider the plasma expansion in vacuum: during this process a fraction of energy is transferred from hot electrons to ions.

- A second approach models the sheath field in the early stages of TNSA $\tau_{e,hot} < t < \tau_i$ (fig. 3.1) and does not take into account its temporal evolution due to the plasma expansion. In this framework bulk ions are fixed into the target while surface ions are test particles boosted by the electrostatic field, supported by the charge displacement. In this work we will present a particular case given by *quasi-stationary* models in which the electron cloud is neither influenced by ions or evolves in time. This approach is particularly appealing to describe the most energetic component of the ion spectra.

- A final strategy is an *hybrid* one which describes similar time scales as the quasi-stationary one but takes into account the motion of light ions and the temporal evolution of the sheath field.

It is important to remark how all the here described models consider time intervals greater that $\tau_{e,hot}$, so that electrons can be safely assumed to be in thermal equilibrium with a characteristic temperature T_h. Most of theoretical works model hot electrons with the Boltzmann relation:

$$n_e = n_0 e^{\frac{e\phi(x,t)}{T_h}}. \tag{3.1}$$

Moreover, semi-infinite plasmas are usually exploited and represent a good approximation for targets much thicker than the typical penetration depth of the sheath field inside the target (typically tens of nm). In this framework, n_0 is the unperturbed density inside the target ($x \to -\infty$). This choice leads to an intrinsic limitation to theoretical models. The infinite extension of the electron cloud ($n_e \to 0$ for $x \to \infty$) implies ions to be accelerated over infinite distances, leading to the divergence of their energy that is not compatible with the sharp cut-off measured in experiments. To address this problem several solutions have been proposed, such as:

- Impose a finite acceleration time or acceleration distance for ions
- Consider plasmas with finite dimension. This limits the total energy stored inside it and thus the energy acquirable by ions.
- Replace the Boltzmann relation with a cut-off in the electron spectrum.

In the following subsections we provide a more detailed description of some of the most renowned models for each theoretical class.

3.1.1 Fluid models

A basic approach to the problem is to adopt a fluid description of the plasma (thus neglecting kinetic effects) and taking into account only the electrostatic problem. This system of equations is then considered:

$$\begin{cases} \nabla E = 4\pi(Zni - n_e) \\ \frac{\partial n_j}{\partial t} + \frac{\partial}{\partial x}(n_j v_j) = 0 \\ \frac{\partial v_j}{\partial t} + v_j \frac{\partial v_j}{\partial x} = \frac{q_j E}{m_j} - \frac{\nabla p_j}{n_j m_j} + R_a \end{cases} \tag{3.2}$$

where n_j, v_j, p_j and q_j are respectively the density, velocity, pressure and charge of the j-th plasma population. The term R_a takes into account the evolution of the fluid momentum due to collisions with other plasma species.

Several assumptions are required in order to analytically solve this problem. In first place, as seen in section 2.1.3, the collisional term can be ignored, as well as the ion pressure with respect to the electron one ($T_e \gg T_i$ in most cases). Furthermore, for $t \gg \tau_e$ electron inertia can be neglected. Electrons are assumed to be in thermal equilibrium and modeled with the Boltzman relation.

Under these approximations the system to be solved reduces to:

$$\begin{cases} n_e e E = -\nabla p_e \\ \frac{\partial n_i}{\partial t} + \frac{\partial}{\partial x}(n_i v_i) = 0 \\ \frac{\partial v_i}{\partial t} + v_i \frac{\partial v_i}{\partial x} = \frac{ZeE}{m_i}. \end{cases} \tag{3.3}$$

The initial condition is a semi-infinite plasma slab (x<0) of density n_0. This set of equations provides the temporal evolution of the electrostatic field, plasma density and, more importantly, the velocity of the plasma fluid, required to estimate the ion spectrum. A basic approach to the problem is to exploit the quasi neutral approximation $n_e \simeq Zn_i$, valid for length scales greater than the electron Debye length. If an isothermal expansion of the electron cloud is considered, this system can be finally analytically solved exploiting self similar solutions [96]. For t>0 a rarefaction wave flows into vacuum and the density profile as well as the fluid velocity can be retrieved.

$$\begin{aligned} v_i &= c_s + \frac{x}{t} \\ n &= n_0 e^{-\frac{x}{c_s t}} \end{aligned} \tag{3.4}$$

where $c_s = \sqrt{\frac{ZT_e}{m_i}}$ is the already defined ion sound velocity. This approach is particularly appealing to predict the accelerated ions spectra, as proved by the good agreement with numerical simulations in [148]. This model has, however major limitations resulting from the quasi-neutral approximation which breaks for sub-picosecond time scales, shorter than ion dynamics, limiting the range of applicability of this model. Moreover, the Boltzmann relation coupled with an isothermal expansion naturally leads to a diverging ion velocity for $x \to \infty$, thus can not be used to estimate the TNSA cut-off energy without imposing a finite acceleration distance or time. The actual position and velocity of the ion front can be estimated noticing that the quasi-neutrality approximation is no longer valid when the density scale length ($c_s t$) equals the local Debye length. If we finally assume that an ion can not overcome than the ion front, the maximum velocity is:

$$v_{i,max}(t) = 2c_s \ln(\omega_{pi} t) \tag{3.5}$$

which is still divergent. In [148] the authors exploited a Lagrangian code to solve numerically the system of equations 3.3 within the approximation of isothermal expansion of a semi-infinite plasma slab. The computed maximum energy scaling law is:

$$E_{max} = 2ZT_h \ln^2(\tau + \sqrt{\tau + 1}) \tag{3.6}$$

with $\tau = \omega_{pi} t / \sqrt{2\mathrm{e}}$. Despite being more accurate than the quasi neutral model, this solution is still intrinsically divergent due to the isothermal expansion and Boltzman distribution. We remark how the initial condition (a semi-infinite slab) supports an isothermal expansion, due to the infinite amount of energy stored in the electrons.

The strategy adopted by the authors to avoid the divergence of the cut-off energy is to consider a finite acceleration time [146, 149] given by this semi-empirical law:

$$t_{max} = 1.3\tau_L + \tau_{offset}, \tag{3.7}$$

τ_L being the pulse duration. An off set is added (78 fs) in order to cope with the under-estimation of ion energies for ultra-short pulses (τ_L<150 fs).

The main issue of this solution is that an external constraint on the acceleration time is unphysical. To avoid this, a more realistic model has been proposed by Mora which describes the adiabatic expansion of a thin foil in vacuum [150].

The main difference with respect to the previous case is that a finite target is studied and electrons cool down as they expand with ions. The hot electron temperature T_h evolves in time in accord with the energy conservation:

$$\frac{dE_e}{dt} = \frac{dE_f}{dt} + \frac{dE_i}{dt} \tag{3.8}$$

where E_e, E_f and E_i are the energies stored by electrons, fields and ions respectively. This equation is coupled with 3.4 and the system is solved with the Lagrangian code, obtaining this result for the ion maximum energy:

$$E_{max} = 2ZT_h \ln^2\left(0.49\frac{L}{\lambda_{De}} + 5.4\right) \tag{3.9}$$

where L is the target thickness. The adiabatic expansion does not require the imposition a finite acceleration time due to the finite energy of hot electrons in a thin slab. We finally remark how an intrinsic limit of these approaches is that they do not distinguish between the different ion species. The plasma expands as a whole, while it is generally accepted that just surface ions are efficiently accelerated in TNSA.

3.1.2 Quasi stationary models

The *quasi stationary* approach is one of the simplest but yet predictive for TNSA. In this scheme, a stationary electrostatic field is supported by the charge displacement given by immobile bulk ions and the hot electronic cloud. Surface ions, on the other hand, are treated as test particles, being accelerated by the sheath field without perturbing the system. This approach is particularly suitable to evaluate the most energetic component of the accelerated TNSA spectrum.
The theoretical model proposed in [151] retrieves the electrostatic potential from the solution of the monodimensional Poisson equation:

$$\begin{gathered}\frac{d\phi^2}{d^2x} = 4\pi\rho \\ \rho = \begin{cases} n_e, & \text{x>0} \\ n_e - Zn_i & \text{x<0} \end{cases}\end{gathered} \tag{3.10}$$

where n_e and n_i are the electron and ion density, respectively. As initial condition a semi-infinite plasma slab is considered where bulk ions are confined (x<0). Electrons, on the other hand, extend in vacuum (x>0). In [151] the authors exploited the Boltzmann relation which, as we anticipated, leads to the divergence of the electrostatic potential and, thus, of the ion cut-off energy. To overcome this hurdle authors imposed a finite electron cloud extension (l) so that n_e(x> l)=0. In this framework the ion maximum energy is given by:

$$E_{max} = ZT_h \ln\left[1 + \tan^2\left(\frac{l}{\sqrt{2}\lambda_{Dh}}\right)\right] \tag{3.11}$$

where T_h and λ_{Dh} are the hot electron temperature and the Debye length. The l parameter can be evaluated through experimental fits but represent a serious limit on the model since there is no self-consistent method to support a finite acceleration distance within simple physical assumptions. In reference [152] an alternative strategy is proposed. In the so called *trapped electrons* model the most energetic component of the hot electron spectrum can escape the self-consistent electrostatic field and does not contribute to ion acceleration. The hypothesis of two populations, given by bound and free electrons, is supported by several experimental and numerical works [153, 154] and allows to estimate a finite ion cut-off energy without any unphysical constraint.

Under this assumption the Boltzmann relation cannot be used and a kinetic treatment is required. In [152] the Maxwell-Boltzman distribution function was used to describe hot electrons, while the relativistic corrected description in [155, 156] exploits the Maxwell-JÃijttner function:

$$f_e(x,p) = \frac{\tilde{n}}{2m_e c K_2(\zeta)} \mathrm{e}^{-\zeta\left(\gamma(p) - \frac{e\phi(x)}{m_e c^2}\right)}, \tag{3.12}$$

being $\tilde{n}$ the normalization coefficient, $\zeta = m_e c^2/T_h$, K_2 the modified Bessel function of the second kind and $\gamma = \sqrt{1 + p^2/m_e c^2}$ the Lorentz gamma factor.

The electron density responsible for ion acceleration can be self-consistently found integrating 3.12 over energies satisfying the local *bound condition*: $e\phi(x) - E_k < 0$ (being E_k the kinetic energy).

$$\begin{cases} n_e = \int_0^{p_{max}} f(x,p)dp = \tilde{n}\frac{I(\varphi(x),\zeta)}{\zeta K_2(\zeta)}\mathrm{e}^{\varphi(x)} \\ \left[\gamma(p_{max}) - 1\right] m_e c^2 = T_h \varphi^* \end{cases} \tag{3.13}$$

where we defined:

$$\varphi \equiv \frac{e\phi}{m_e c^2}, \quad I\left[\varphi(x), \zeta\right] \equiv \int_0^{\beta(\varphi)} \mathrm{e}^{-\sqrt{\zeta^2 - p^2}} dp, \quad \beta(\zeta, \varphi) \equiv \sqrt{(\varphi + \zeta)^2 - \zeta^2}. \tag{3.14}$$

Relation 3.13 coupled with the Poisson equation allows to evaluate the spatial profile of the electrostatic potential which is peaked at the solid-vacuum interface. The cut off energy of TNSA ions can be straightforwardly evaluated as:

$$E_{max} = Ze\phi(x=0)T_h = ZT_h\left[\varphi^* - 1 + \frac{\beta(\zeta, \varphi^*)}{I(\varphi^*, \zeta)e^{(\zeta + \varphi^*)}}\right]. \tag{3.15}$$

We must remark how Eq. 3.15 depends only on two parameters: the hot electron temperature T_h and φ^*. The latter is the electrostatic potential deep inside the target which determines the maximum energy of bound electrons. These parameters determine the accuracy of the model, however, they are strictly dependent on the physical system studied and can not be straightforwardly measured in experiments. A basic approach to obtain simple scaling laws is to combine the experimental results with analytical and numerical models. As far as φ^* is of concern, the most natural strategy is to link the maximum bound electron energy to the energy of the laser beam. At this regard, in reference [156] authors proposed a semi-empirical law obtained fitting experimental results $\varphi^* = 4.8 + 0.8 Log(E_L)$. A more advanced model, described in reference [90], takes into account the effect of electron recirculation during the interaction with the laser beam.

$$\varphi^* + \log\left[\frac{I(\varphi^*)}{\zeta K_2(\zeta)}\right] = \log\left[\frac{\eta \tilde{D}_h}{\tilde{n} D \left\langle E_k \right\rangle V_\infty}\right] + \log(E_p) \tag{3.16}$$

where $\langle E_k \rangle$ is the mean kinetic energy of electron, D is the target thickness, $\tilde{D}_h$ is the longitudinal extension of the electron cloud in a semi-infinite target (no recirculation) and V_∞ its volume. The implicit Eq. 3.16 can be solved and allows to predict the ion cut-off energy as a function of the target thickness.

Besides φ^* the other parameter to be estimated is the hot electron temperature T_h. As seen in section 2.1.3, T_h is determined by laser induced electron heating mechanisms, most of them still subject of major discussion and theoretical research, and is further discussed in section 3.3.

The main advantage of the *trapped electrons* model with respect to other approaches is that it offers a self consistent description of the TNSA field which is naturally limited over a finite region and does not require further limitations on ion dynamics (e.g. acceleration time or distance).

3.1.3 Hybrid models

Quasi stationary models are particularly suitable for evaluating the highest energies achievable by light ions, however they lack the description of dynamical effects which can affect TNSA spectra. At this purpose several *hybrid models* have been proposed in the effort to combine in a simple way fluid and stationary approaches.

In this section we present two widely accepted descriptions: the layered target description [157] and the moving sheath model [158].

In ref. [157] authors consider the evolution of a delta-like charge distribution of light ions of surface charge Q_i being accelerated by the self-consistent sheath field. This model is meant to take into account the temporal evolution of the electrostatic potential due to the motion of the ion layer.

The Poisson equation is numerically solved using the Boltzmann relation for the electrons and assuming an immobile heavy ion bulk target (a more refined model also takes into account heavy ions dynamics). The electrostatic field at the layer position x_L is found. Finally the median force acting on the accelerated ions is computed and a scaling law for the ion maximum energy is obtained:

$$E_{max} = Z_i T_h f(q) \tag{3.17}$$

with $q = \frac{Q_i}{en_{H0}\lambda_{Dh}}$ being the normalized surface charge and $f(q)$ the function:

$$f(q) = 3.44 - 2.66ln(q) - 0.182ln^2(q). \tag{3.18}$$

This relation holds for $0.003 < q < 0.3$, condition satisfied in TNSA experiments.

In the moving sheath model [158] surface ions (usually light ions of the contaminant layers) are treated as test particles being accelerated in the electrostatic field which is found from the solution of the Poisson equation. Bulk ions dynamics affect the temporal evolution of the sheath field and is modeled with the thermal expansion model in ref. [148]. The TNSA field is then numerically found as a function of the bulk ion front:

$$E(t) = \frac{\sqrt{2}T_h}{e\lambda_{Dh}} \mathrm{e}^{\left(\frac{e\phi(t)}{2T_h}\right)} \left[1 + \frac{x - x_s(t)}{2\lambda_{Dh}} \mathrm{e}^{\left(\frac{e\phi(t)}{2T_h}\right)}\right]^{-1} \tag{3.19}$$

where $\phi_s(t)$ is the electrostatic potential at the ion front ($x_s(t)$).

The integration of the electrostatic field should give an estimation of the cut-off energy, however, the Bolztmann distribution leads, once again, to its divergence. In a similar way to [148] an external constraint on the maximum acceleration time can be imposed in order to retrieve a finite value for E_{max}.

3.2 Numerical approach

Despite the interest over analytical models, many heavily non linear phenomena can not be treated with theoretical approaches unless by extremely simplified means. In this context, numerical simulations are largely exploited in physics to support theory and to interpret experimental results. Over the last decades a collection of numerical tools has been developed, suitable in specific physical scenarios. In figure 3.2 the most commonly used to model plasmas are presented, detailed descriptions are provided in [26, 159].

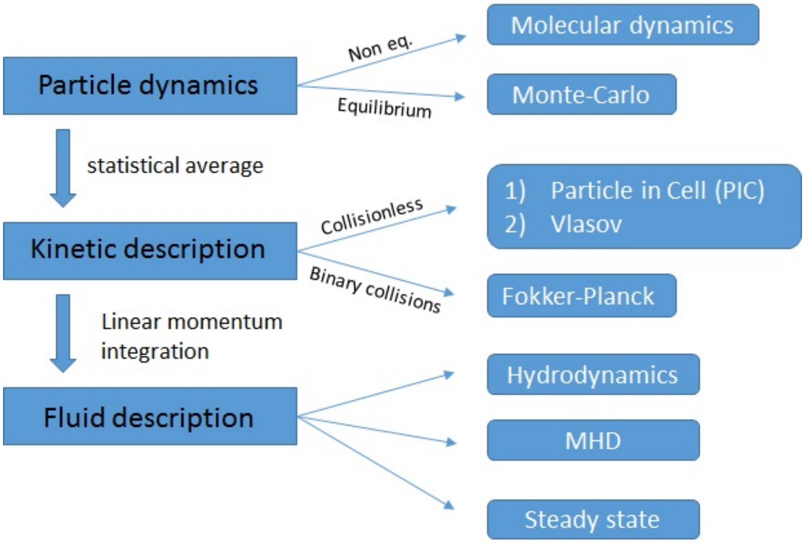

Figure 3.2: *Schematic representation of common numerical approaches (image adapted from [26]).*

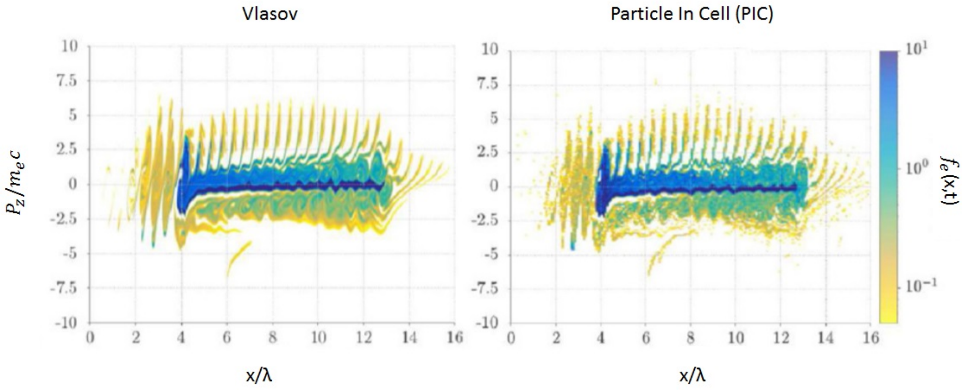

Figure 3.3: *Comparison between Vlasov and PIC results. The electron phase spaces are taken in the exact same time frame and experimental conditions (image adapted from [160]).*

In interaction regimes explored in this work kinetic effects cannot be ignored. Moreover, due to the high laser intensities simulated ($I > 10^{19}$ W/cm^2), in first approximation, the process of matter ionization can be neglected as well as particle collisions. The fully ionized plasma can be then well computed with *Vlasov* as well as Particle In Cell codes. Vlasov codes solve the system given by relativistic Vlasov and Maxwell equations for each particle species and they better resolve the actual evolution of the distribution functions, as presented in figure 3.3. Despite being more accurate, Vlasov codes are more computationally expensive, at the point that in most of cases their requirements for 3D simulations exceed the computational capabilities of high performance facilities worldwide.
In this work we relied on PIC simulation, at this purpose, in the following section we provide a basic description of these codes.

3.2.1 Particle In Cell codes

Particle In Cell codes are somehow in between microscopic and kinetic approaches. In reference [161] is provided an in depth discussion of the relation between PIC and Vlasov codes and their reliability with respect to the real plasma physics.
In the PIC approach, the actual distribution functions are sampled with macro-particles carrying a fixed charge and mass, while the electromagnetic fields are spatially sampled on a grid. The value of the Lorentz force in each point of the simulated space is found by interpolation of EM field on adjacent grid points. Macro particles are moved individually by the effect of the Lorentz force and their motion self-consistently modifies the fields values accordingly to Maxwell equations. In figure 3.4 we offer a schematic representation of a single PIC time step. If we start from the current deposition on the grid point two basic strategies can be highlighted: energy conservation and charge conservation algorithms. The former forces the energy conservation at the price of a non exact charge conservation which may lead to unphysical effects. The *Esirkepov* current algorithm, on the other hand, ensures the charge conservation. This strategy is however more computationally expensive and it will be not considered since the open source Particle-In-Cell code PICcante [162] used in this work embraced the first approach.
As **J** are deposited on the simulation grid the macroparticles are moved as in a lagrangian approach, the E field evolves of a full time step while B field of half time period in accord with Maxwell equations. At this point particle momenta are advanced of a full step and, finally the B field of the

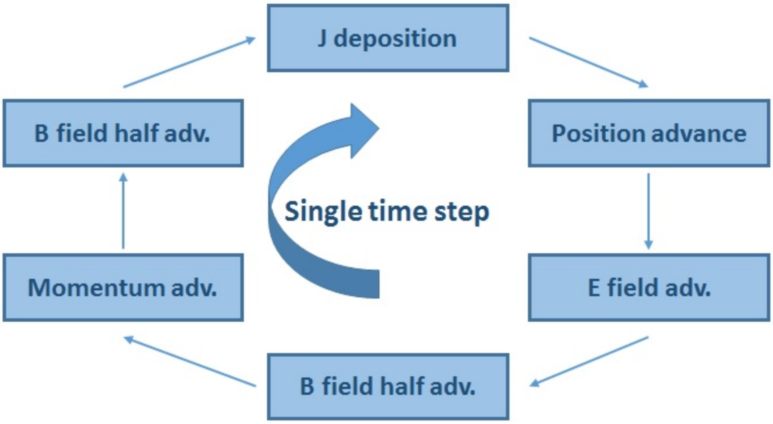

Figure 3.4: *Basic principle of a single time step of a common Particle In Cell code.*

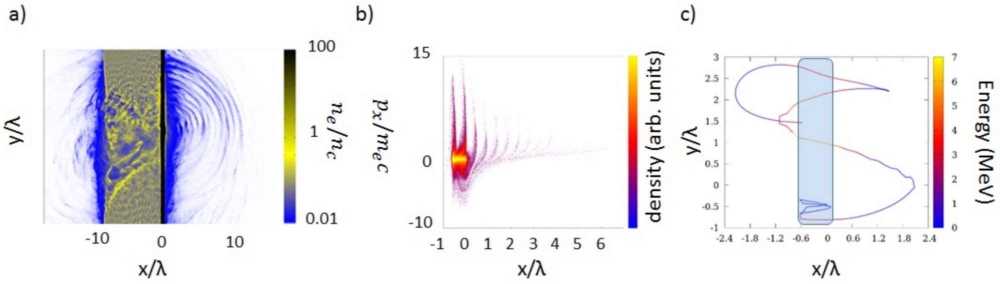

Figure 3.5: *Graphical visualization of PIC outputs. a) electron density after the interaction of an intense laser beam with a foam attached target, b) phase space (p_x,x) of electrons from an irradiated micrometric foil, c) representative trajectory of a surface electron from the previous simulation.*

remaining half. The integration method adopted is the well known *leap frog* (see ref. [159] for more details) which provides a simple and accurate tool to solve differential equations. As example, in the particle push routine positions and momenta evolutions are shifted of half a period and this ensures an error that vanishes as $\Delta t \to 0$ as an $O\left[(\Delta t)^2\right]$. This is a fair tradeoff between more accurate but heavier algorithms (e.g. Runge-Kutta 4 $O\left[(\Delta t)^4\right]$) or lighter but less accurate ones (e.g. Euler algorithm $O\left[\Delta t\right]$)

3.2.2 Data analysis and derived quantities estimations

The binary output of PICcante numerical code used in this work is converted in formats suitable to be read with scientific data analysis software such as Origin and Gnuplot. In figure 3.5 several examples of PIC outputs

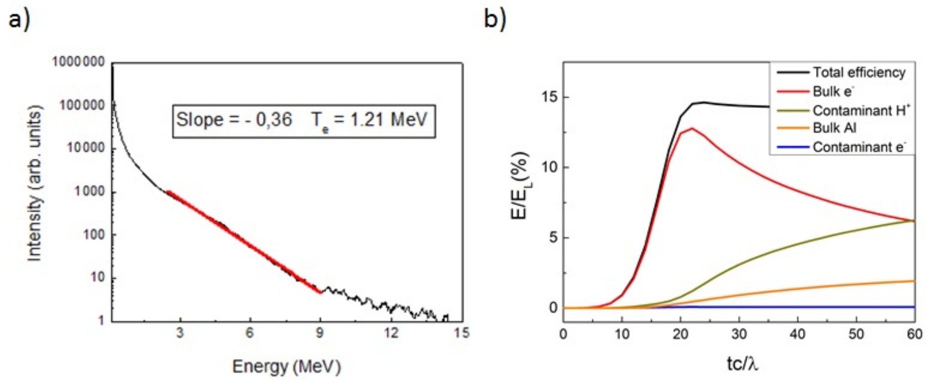

Figure 3.6: *a) Typical electron spectrum observed in laser interaction with flat solid targets. The red line represent the linear fit performed. b) Time evolution of the E/E_L of different particle species in a TNSA PIC simulation. In black the total efficiency is shown.*

are shown. Spatially and temporally resolved densities, phase spaces and electromagnetic fields (not shown in figure) can be probed and results can be directly compared to analytical models. Moreover as seen in fig. 3.5.c particle trajectories can be extracted from the output files and these can be of great aid in the interpretation of the physics simulated.

Finally, quantities such as the electron temperature or the interaction efficiency are extremely relevant in this work and are derived from direct output of the numerical code. Nonetheless it is necessary to clarify the procedure followed in this work. At the thermal equilibrium the electron spectrum is proportional to $e^{E/T}$ and its temperature can be evaluated straightforwardly. As illustrated in figure 3.6.a, we performed a linear fit in a semi-logarithmic scale, the temperature is then the inverse of its slope. This strategy holds only if the analyzed spectra exhibits quasi-exponential behavior at least in certain energy intervals (if non complete thermalization occurs). Fortunately this condition is easily fulfilled, since in simulations performed in this work ion acceleration takes place on a latter temporal frame with respect to electron heating, thus electrons have enough time to reach thermal equilibrium.

The interaction efficiency on the other hand was estimated by the ratio of the total plasma energy (or the one of a specific population) and the incident energy of the laser beam. Particularly relevant in this work is the electron heating efficiency, evaluated in the time frame when the electron energy reaches its peak, as in figure 3.6.b.

3.3 Open problems & objectives of this work

It is now useful to sum up some of the most relevant open problems regarding the control and optimization of TNSA from both analytical and experimental point of views.

A better control over the technique can be achieved with a more satisfying comprehension of the whole ion acceleration processes and how the vast range of laser (e.g. intensity, polarization, incidence angle, pre-pulse) as well as target (e.g composition, thickness, target design) parameters affect TNSA. This would arguably lead to its optimization in terms of ion cut-off energy, conversion efficiency and total accelerated charge, also with the aim of providing laser-induced accelerators suitable for applications. In order to properly fulfill this task, a combined experimental and analytical approach must be adopted.

As seen in section 2.1.1, it is widely accepted that the laser parameters play a major role in ion acceleration. Their actual contribution, however, is still subject of discussion due to the fact that they cannot be independently varied, preventing a proper separate study. An additional hurdle is given by the fact that high power laser facilities do not always guarantee a perfect reproducibility of experiments, leading to significant fluctuations despite similar nominal conditions.

Even in the most investigated scenario of TNSA with micrometric solid targets a satisfying experimental background has not been achieved yet. Despite the fact that experimental works proved a strong influence of the laser intensity and power on TNSA properties, the actual dependence is still not globally acknowledged. As seen in section 2.1.1 a scaling law of the ion maximum energy to the laser intensity is reported in all experiments. It is, however, subject to significant variations between high energy-long pulses (E$\sim$ 100 J, $\tau \sim$ ps) and low energy-short pulses (E$\sim$ J, $\tau \sim$ 10 fs), being $E_{max} \propto I^{0.5}$ and $E_{max} \propto I$, respectively.

Besides, it is well known that laser polarization and incidence angle play a crucial role in electron heating and ion acceleration [87, 163], however this topic is still inadequately covered. Indeed, the few and scattered experimental results cannot allow to draw a trend, expempli gratia, of the effect of laser polarization at different intensities or incidence angles.

Coherently with section 2.1.2, electron heating is one of the fundamental sub-processes of TNSA. Indeed, a proper mastery of the laser plasma coupling could lead to a more efficient ion acceleration. In particular, the temperature of hot electrons (T_h) is acknowledged to determine TNSA properties (e.g. the cut-off energy). In accord with section 2.1.3, electron

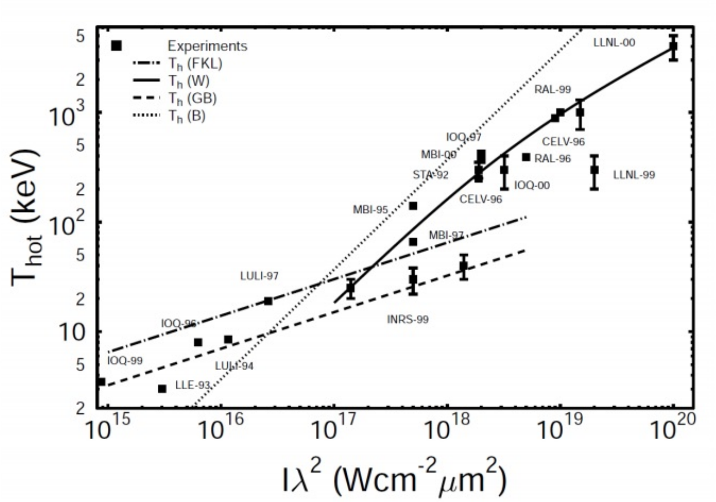

Figure 3.7: *Electron temperature as a function of the laser irradiance $I\lambda^2$. Black squares refer to experimental measurements of experiments involving fs laser pulses interacting with micrometric solid targets (image from ref. [26]).*

heating results from a large collection of different and possibly competing mechanisms, most of them insufficiently surveyed. Due to the richness of the physics at play and the technical difficulties of direct measurements of T_h, experiments may be particularly hard to be interpreted and may not be sufficiently accurate if a specific electron population is to be probed (e.g. the hot electrons confined at the interfaces).

Despite these issues, experimental measurements with micrometric flat solid targets, typically used in conventional TNSA, reported a solid scaling law of the electron temperature with respect to the laser irradiance ($I\lambda^2$). Indeed, in fig. 3.7 a clear dependence to $I\lambda^2$ is evident, despite the wide range of experimental parameters considered. In particular, at higher irradiances ($I\lambda^2 > 10^{17}$ Wμm^2/cm^2) a scaling proportional to $\sqrt{I\lambda^2}$ is found. This trend is also remarkably similar to the one of the ion maximum energy reported with long pulses and supports the assumption of an essential connection between electron heating and ion acceleration. Nonetheless, the experimental database does not offer any information regarding the dependence of the electron temperature to other laser parameters. Moreover, previous studies can not be applied in context of advanced targets. Consistently with section 2.2, innovative solutions were proposed in the latest years to enhance the laser plasma coupling and, as a consequence, ion acceleration. In this context, a proper investigation of TNSA through

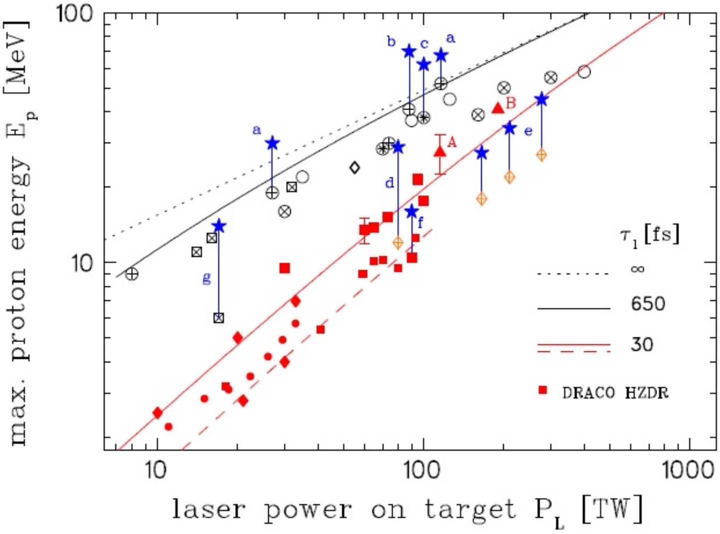

Figure 3.8: *Proton cut-off energy measured with linearly polarized laser beam in different high power laser facilities (we remand to ref. [164] for a better description). The red and the black symbol refers to short (∼ 10 fs) and long (> 500 fs) pulses respectively. The connected blue stars are referred to advanced acceleration techniques and are linked to benchmark results with traditional targets.*

extensive and controlled experiments would be particularly appealing. As seen in fig. 3.8, promising performances have already been achieved at 100 TW laser facilities worldwide. However most of these experiments are one-shot observations at fixed conditions, parametric studies are still far beyond the current state of the art.

Among the possible evolutions of TNSA, in this work we focused on the foam attached targets presented in the section 2.2.1. The first experimental campaign was encouraging but still in a preliminary state [130,165] and required a parametric study at higher laser intensities ($I > 10^{19}$ W/cm^2). These multi layered targets could be of of great interest not only in the framework of ion acceleration but also to probe laser interaction with near-critical plasmas (resulting from foam ionization), a challenging and still uncharted topic of research.

Along with the improvement of the experimental background a better comprehension of the acceleration process is also of great importance. At the state of the art the TNSA scheme can explain the most iconic features of accelerated ions. Nevertheless, a deeper knowledge of the physical process is still required to reach a greater control over the technique.

Analytical models presented in 3.1 proved good agreement with experimental results, as also reported in [156]. They however suffer a rather limited range of applicability, moreover, they need to be extended to advanced target designs. Taking Eq. 3.6, 3.9, 3.15 and 3.19 as references, we highlight how all the models presented rely on quantities that must be estimated by theoretical means or with semi-empirical approaches. Providing more accurate scaling laws is a logical strategy to increase the capabilities of current TNSA descriptions. In most of theoretical works, the temperature of hot electrons T_h is a fundamental quantity and is required to predict the ion cut off energy . Many theoretical works of TNSA with micrometric solid targets adopt the well known ponderomotive scaling in Eq. 2.17 which is able to reproduce with a good agreement the dependence of T_h to the laser intensity seen in fig. 3.7. However, this approach has some clear limitations: no polarization or incidence angle dependence, which are known to be crucial for laser-plasma coupling [163] and cannot be applied to new target designs. Besides the strong limitations highlighted, recent works [166–168] suggest that ponderomotive scaling can significantly over-estimate T_h at high laser intensities ($I > 10^{19}$ W/cm^2). Clearly, an improvement of the estimation of T_h would allow, not only to extend the predicting capability of the quasi-stationary model, but also to improve other theoretical descriptions.

This PhD work was carried out within The Micro and Nanostructured

Materials Lab (NanoLab) group of Politecnico Di Milano and was aimed at overcoming some of current issues of TNSA. In particular this work was divided as it follows:

- **Experimental activity**: A consistent part of this work was devoted to the analysis of two recent experimental campaigns carried out by the Nanolab group (Politecnico Di Milano) in collaboration with the GIST institute (Gwangju, Republic of Korea). This activity had a dual aim. First of all it allowed to demonstrate the feasibility of an enhanced TNSA with foam attached targets (MLT) with respect to traditional micrometric foils (SLT). A parametric study of the effect of laser intensity and polarization was carried out with both target configurations: different designs targets were tested for the first time in an extensive campaign at high laser intensities (I> 10^{19} W/cm^2). These analysis also provided a solid and reliable experimental database which proved to be an invaluable tool to test theoretical models under a wide range of parameters. In chapter 4 we provide a detailed description of some of the most remarkable results observed in the experimental campaigns.
- **Theoretical activity**: in order to further extend the applicability range and accuracy of current theoretical TNSA models, chapter 5 was dedicated to the theoretical study of electron heating with both SLTs and MLTs. As far as traditional targets are of concern, our aim was to provide a more accurate scaling law for the electron temperature which could take into account some crucial parametric dependencies (polarization and incidence angle) not considered by previous models. With MLTs the task was harder since no reliable models were available at the state of the art. At this purpose we performed a first approach in order to understand the role of the laser intensity into electron heating with foam attached targets.
- **Numerical activity**: as anticipated, numerical simulations could provide powerful support to analytical approaches. Indeed, a large numerical campaign was performed in order to probe the laser-plasma coupling in conditions suitable for TNSA. Quantities such as the electron temperature and heating efficiency were estimated at different laser intensities, polarizations and incidence angles using both micrometric foils and foam attached targets. These results, combined with the analytical model guaranteed a solid scaling law which could predict the angular and polarization dependence of the electronic temperature over an ample range of laser intensities, appealing for ion

acceleration (I>10^{18} W/cm^2). Our numerical activity was also aimed at probing laser-plasma coupling with foam attached targets. An intensity scan was performed at fixed laser and target configuration in order to understand the enhancement in the electron heating in conditions similar to those of the two experimental campaigns performed in 2014 and 2015. This analysis also supported the simple theoretical model and this combined strategy provided a reliable scaling law for T_h that could be applied to MLTs.

- **Benchmarks**: an interesting solution in order to test our numerical and theoretical results was to combine these results with the quasi-stationary model 3.1.2 to predict the experimental results analyzed in chapter 4. The final outcome of this work was to prove that our description could be more accurate than previous ones to interpret laser induced electron heating.

4

Data analysis of ion acceleration experiments with solid and nanostructured targets

In agreement with section 3.3, experiments under controlled and reproducible conditions are of ultimate priority to provide a reliable experimental picture of the parametric dependencies of TNSA. This is required, not only to achieve a greater understanding of traditional TNSA with micrometric solid targets (SLT), but also to test the potentiality of innovative target designs such as foam attached targets (MLT). Coherently with section 2.2.1, these foams can provide a near-critical layer and it is generally acknowledged in the plasma physics community that such plasmas could greatly boost the laser energy absorbed [115,121,122,169,170] and could be appealing to enhance ion acceleration. This topic, however, remains quite unexplored in experiments owing essentially to the technical difficulties of creating controllable and reproducible low density plasmas (~ 10 mg/cm^3). These can be produced using different techniques such as gas jets [171,172], preplasmas [93,94,173], chemical depositions of foams [115, 174] and nanotubes [73, 175] or foams created using pulsed laser deposition [165]. The latter, in particular, is proved to be a reliable source of low density materials of controlled thickness, density and composition which can be also deposited over virtually any substrate. Foam created using Pulsed Laser Deposition (PLD) are characterized by a porous structure composed by solid-density nano-particles (d $\sim$ 10 - 20 nm) resulting in an average near-critical density on a micrometric scale. Advanced MLTs have been firstly analyzed in a numerical campaign in ref. [123] which demonstrated how a near-critical plasma layer on a solid substrate may strongly increase both the conversion efficiency and the electron heating, leading to an enhanced TNSA mechanism. In particular, 2D and 3D numerical simulations highlighted the importance of target parameters (e.g. foam thickness and density) to achieve the best acceleration performances. A first experimental campaign was carried out with the UHI100 laser system at the CEA Saclay center [130]. In that explorative work two Aluminum SLTs of different thicknesses, 1.5 and 10 μm were adopted and their performances were compared to MLTs composed by 12 and 24 μm C foams, deposited on Al substrates (1.5 and 10 μm, respectively). Carbon foams were characterized by an average density of 7 ± 2 mg/cm^3 which corresponded to a near critical density if fully ionized (n_c coincides to 5.7 mg/cm^3 with 800 nm laser wavelength). Targets were irradiated at 10° incidence with laser beams in the $10^{16} - 10^{19}$ W/cm^2 intensity range in both Low Contrast (10^8) and High Contrast (10^{12}) regime. In [130] the authors reported proton cutoff energies in the MeVs range with an increase of a factor 2-3 at moderate intensities ($I<10^{18}$ W/cm^2) with respect to benchmark SLTs.

An important part of this PhD work was aimed at the analysis of experimental results of TNSA obtained in the framework of an international collaboration led by the Nanolab group in two campaigns in 2014 and 2015 at the PW-class laser facility APRI (GIST, Gwangju, Republic of Korea). These experiments not only provided a solid database with traditional micrometric solid targets (SLT) in a wide range of laser intensities $0.5 \cdot 10^{20}$ W/cm^2$<I<$$4.5 \cdot 10^{20}$ W/cm^2 and polarizations (P-,S- and C- pol) but they also represented the first extensive work with innovative foam attached targets (MLT) in the high intensity regime.

In the framework of this PhD thesis, these results were exploited to support our theoretical and numerical activities in both contexts of SLTs and MLTs. In particular, in chapter 5 we used the here-presented data set to benchmark the prediction of a new analytical model for the electron temperature.

At this purpose, this chapter will be divided as follows. In section 4.1 we illustrate the production and characterization techniques of foam attached targets as well as the specifics of the targets used in the analyzed experiments. Section 4.2 describes the experimental setup of the two campaigns with a particular focus on the diagnostics adopted. Finally, 4.3 will be dedicated to the presentation and discussion of the experimental results.

4.1 Target production and characterization

A remarkable achievement of the numerical campaign in [123] was the parametric study regarding the influence of the foam design on the ion acceleration. In particular, the authors suggested that near critical foams with a thickness ~ 10 μm, coupled with sub micrometric substrates (≤ 1 μm) could provide the best laser-plasma coupling. In this framework, controlled target production and characterization are of crucial importance in order to fulfill ideal conditions for ion acceleration.
Foam attached targets discussed in this chapter were created by Nanolab group using Pulsed Laser Deposition (PLD) technique. With a proper tuning of the deposition parameters, PLD can also be exploited to grow a porous material (foam) over virtually any solid substrate. In figure 4.1 a typical apparatus of Pulsed Laser Deposition is shown. A laser beam is focused onto a target, the resulting ablated material creates a plasma plume which is deposited on the substrate. Coherently with [165], nanoparticles (~ 10 nm) represent the elementary constituent of the deposited film. These aggregate in sub micrometric compounds which determine the target morphology. Under proper deposition conditions, PLD can be exploited to create a void-rich layer, characterized by a mean density hundreds of times lower those of graphite (~ 10 mg/cm^3).
Many experimental features such as laser pulse parameters, gas pressure in the chamber, target temperature and composition influence the properties of the produced foam. As an example in figure 4.2 different foam morphologies are presented as a function of the filling gas and its pressure in the chamber.

In ref. [176] we provided a detailed description of deposition parameters adopted for target production, we here give just a brief summary. A commercial Nd:YAG laser was used in second harmonic mode (wavelength ~ 512 nm) which provided a 7 ns pulse at 10 Hz repetition rate with a fluence of 0.8 J/cm^2. The ablated target was composed of pyrolotic graphite resulting in a carbon foam growth over an Aluminum substrate. Argon, which proved to be ideal to promote the aggregation of nanoclusters, was chosen as filling gas in the chamber. In order to guarantee the best conditions of foam homogeneity and uniformity over large deposition areas ($\sim mm^2$) the substrate was placed on a rotating stage, distant 46 mm from the graphite target.
The foam attached targets produced for the experimental campaigns were characterized by a low density layer in the order of mg/cm^3 ($\sim n_c$) with thicknesses in the 3-64 μm range, obtained tuning the deposition duration.

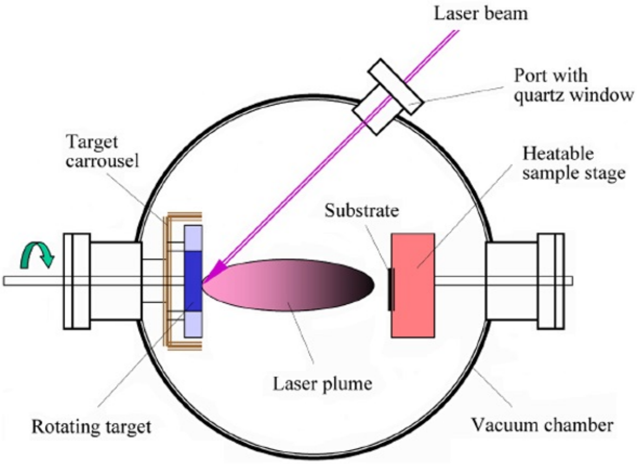

Figure 4.1: *Typical PLD configuration*

To summarize, PLD proved to be a reliable and flexible tool for materials deposition, which is also viable for the production of foams with tunable properties.
Targets were characterized using a Scanning Electron Microscope (SEM) to measure the foam thickness while the density has been evaluated using data acquisitions obtained with Energy Dispersive X-ray Spectroscopy (EDXS) technique. A detailed description of the novel characterization technique adopted is provided in [177].

4.1.1 Targets

The aim of the two experimental campaigns was to explore the capabilities of MLTs at different laser and target configurations using SLTs as references. In the numerical work in ref. [123], the authors showed how foam thickness as well as its density should determine ion properties. In particular, best performances had to be expected with a near-critical foam in the 10 μm range.
At this purpose, in 2014 different foam/substrate thicknesses and foam densities were chosen in agreement with numerical results in [123]. For each shot with foam-attached targets, experiments under the same laser conditions with bare Al foils were performed for comparison. In 4.1 are listed the targets used in the first experimental campaign.

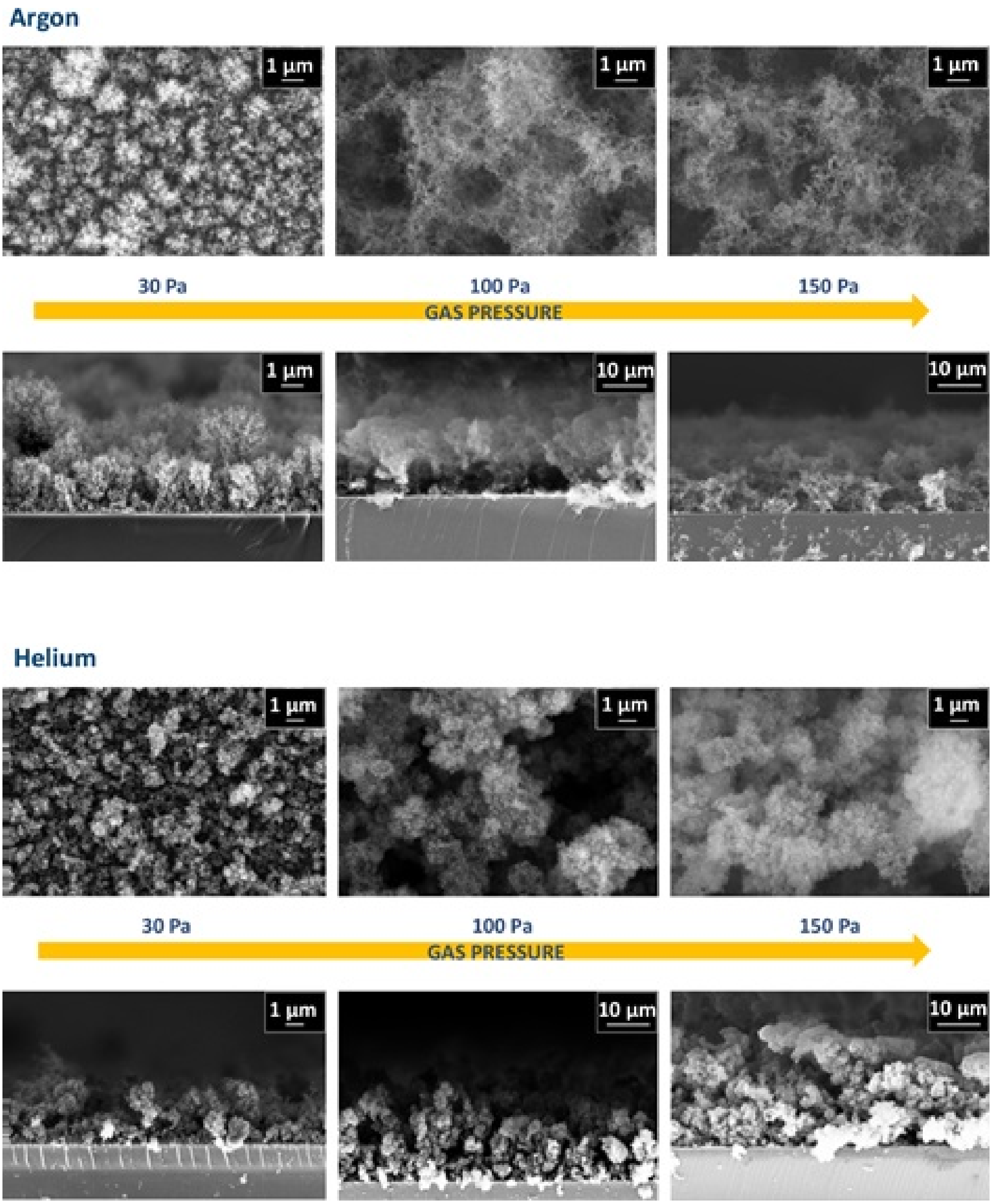

Figure 4.2: *Foam morphology under different deposition conditions*

Substrate composition	**Substrate thickness**	**Foam Thickness**	**Foam density** (n_e/n_c)
Al	0.75 μm	8,12,18,36 μm	1.2
Al	1.5 μm	12,18 μm	1.2
Al	0.75 μm	12 μm	4.3
Al	0.75, 1.5 μm	X	X

Table 4.1: *Targets used in the 2014 campaign*

The second campaign was planned as complement to the first one, providing a parametric study with thinner foams, different substrate compositions and thicknesses, as reported in 4.2.

Substrate composition	**Substrate thickness**	**Foam Thickness**	**Foam density** (n_e/n_c)
Al	0.75, 1.5 μm	X	X
Polymer	20 nm	X	X
Al	0.75 μm	3,5,8,10,12 μm	1.2
Al	1.5, 6.5 μm	8 μm	1.2
Cu	7 μm	8 μm	1.2
Polymer	20 nm	8,12,32,64 μm	1.2

Table 4.2: *Targets used in the 2015 campaign*

4.2 Experimental setup and diagnostics

The two experimental campaigns took place in September 2014 and July 2015 at the Gwangju Institute of Science and Technology (GIST) in Republic of Korea. The PULSER laser system is a PW-class laser, several properties are listed in table 4.3 while a detailed description is provided in [178, 179].

	Design value
Laser system	Ti:Sapphire
Energy before compressor	38 J (2014), 45 J (2015)
Peak Intensity (W/cm^2)	$4.5 \cdot 10^{20}$ (2014), $7 \cdot 10^{20}$ (2015)
Laser Constrast	10^{-12} at 500 ps, 10^{-10} at 50 ps
Pulse Duration	30 fs
Focal Diameter	5 μm
Repetition Rate	0.1 Hz

Table 4.3: *PULSER I laser specifics*

In fig. 4.3 a schematic representation of the interaction chamber is provided. The energy delivered by the laser beam before the compressor was 38 J in 2014 and 45 J in 2015, 25 % of this energy was lost in the compressor stage. A double plasma mirror ensured beam contrast of $3 \cdot 10^{-11}$ 6 ps before the main pulse with a 50 % energy depletion. Due to the geometry of the system, the laser beam on target was S-polarized. However, Half-wave or quarter-wave plates allowed, to provide P- and C- polarizations at the price of an additional 18 % and 13 % energy loss, respectively. As final outcome, few Joules on target were delivered by a 30 fs laser pulse characterized by a circular focal spot of 5 μm diameter which contained 22% of the total beam energy. As reported in the scheme in fig. 4.3 the laser pulse is focused on the target and, finally, the accelerated ion signal is recorded by multiple Thompson Parabolae.

4.2.1 Spectrometer: Thompson Parabola

Thompson Parabolae (TPS) were chosen as the main diagnostics to compare the performances of foam-attached targets with Aluminum foils in terms of both maximum ion energy and spectrum. As presented in fig. 4.4, TPS rely on stationary electric (30-40 kV/mm) and magnetic (~ 0.45 T) fields in order to separate particles with different charge over mass ratios and energies. Since the accelerated ions energies are typically orders of magnitude under their rest masses, relativistic corrections can be neglected and the acceleration due to EM fields is simply given by $\mathbf{a} = \frac{q}{m}\left(\mathbf{E} + \frac{\mathbf{v}}{c} \times \mathbf{B}\right)$. If we then consider a particle moving in the $\hat{z}$ direction with $\mathbf{E}$ and $\mathbf{B}$ lying in the $\hat{x}\hat{y}$ plane, their total x and y displacements with respect to the propagation axis will be:

$$\begin{cases} \delta_x = A\frac{q}{mv^2} \\ \delta_y = B\frac{q}{mv} \end{cases} \tag{4.1}$$

where A and B are dependent to experimental parameter (flight path and EM fields) reported in fig. 4.4. In accord with equation 4.1, charged particles with equal q/m ratio but different energies draw a parabolic trace in the $\hat{x}\hat{y}$ plane. Deflected particles are then collected by detectors such as CR-39 films, *Image Plates* (IP) or *Micro Channel Plates* (MCP). In MCP detectors, the ion signal is converted and amplified into electrons which retain the same spatial structure of the former beam. These electrons impress a phosphor screen, the image then is recorded by a CCD camera (see fig. 4.4). The main advantage of the coupled system of MCP and CCD is that it allows an active data collection, particularly suitable for

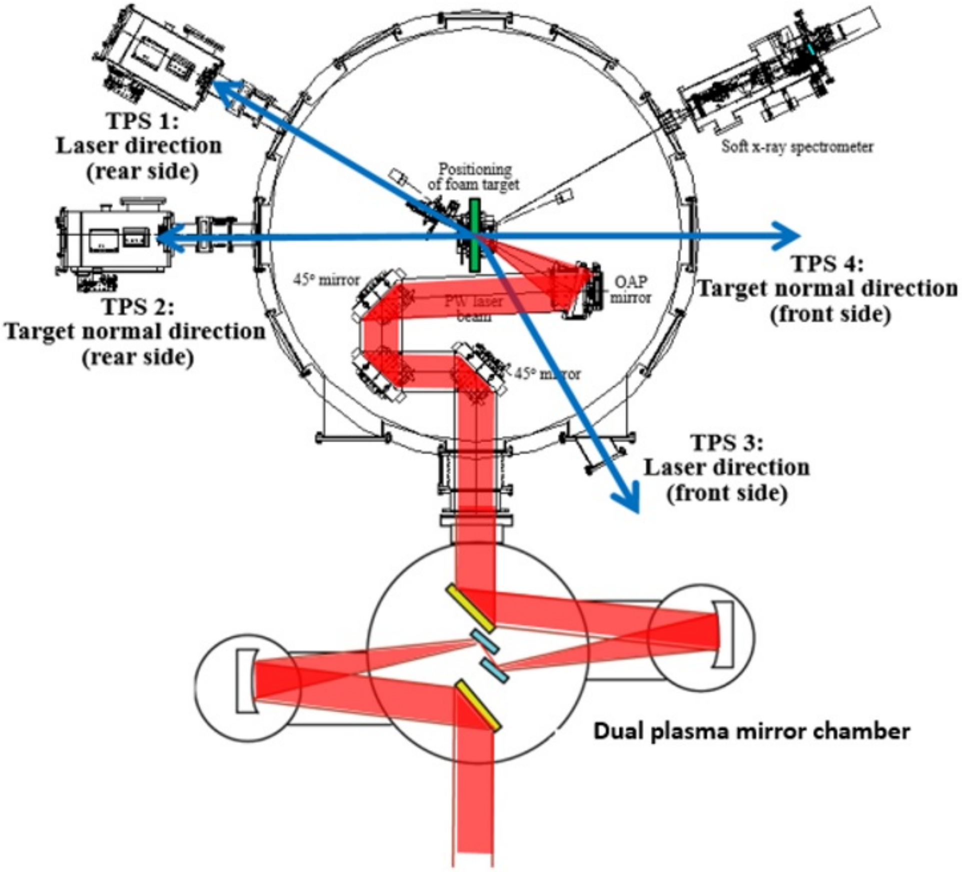

Figure 4.3: *Schematic representation of the experimental setup adopted in Korea in 2015. In the 2014 campaign the two front side TPS were missing.*

measurements at high repetitions rates. Finally, the parabolic traces in fig. 4.4 were analyzed with the software Tiarra which allowed to extract the ion spectra. The main drawback of this diagnostic system is that the absolute calibration is not straightforward to be obtained, mostly due to the strongly non-linear response of MCPs. A latter experiment using a slotted nuclear track detector, CR-39, installed in front of the MCP allowed to calibrate the system.

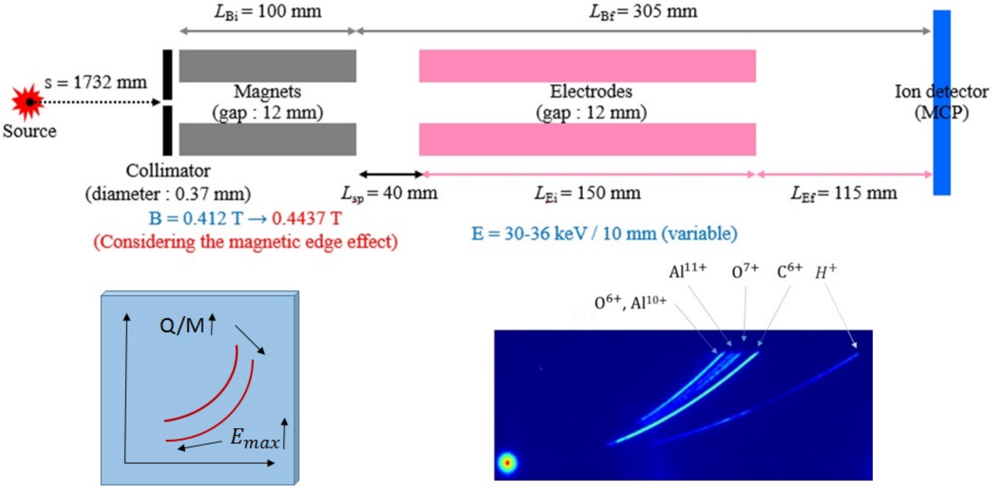

Figure 4.4: *Configuration of the Thompson Parabola Spectrometer adopted in the 2014 experimental campaign*

4.2.2 2014 experimental campaign

The aim of the first experimental campaign conducted in 2014 was to explore the capabilities of MLTs with respect to traditional SLTs. The incidence angle was kept fixed (30°), the pulse intensity was tuned in the range $0.5 \cdot 10^{20}$ W/cm^2<I<$4.5 \cdot 10^{20}$ W/cm^2 with a corresponding energy on target of 1-7.5 J. Another innovative aspect of this experimental campaign was a systematic study of the effect of laser polarization in the context of TNSA with both SLTs and MLTs.

To analyze accelerated ion spectra two TPS were adopted. The first TPS was placed along the axis normal to the rear surface and captured most of the ion signal due to the normal emission of TNSA ions. The second TPS collected ions accelerated along the laser propagation direction to record possible non-normal emissions which could have been relevant with foam-attached targets.

Finally three imaging plates spectrometers were placed in the chamber to capture electron spectra. Since the chamber could only be opened once in a day, each spectrometer could be used for a single shot acquisition. In addition, magnetic fields were too weak to capture the most energetic component of the electronic spectra. For these reasons, only qualitative information regarding the different electron heating in SLTs and MLTs could be obtained and a proper estimation of the electron temperature could not be performed.

4.2.3 2015 experimental campaign

The 2015 campaign setup was similar to the previous one. Two different incidence angles were tested: 30° and 2.5° (defined from here on “normal incidence"). A recent upgrade increased the pulse energy from 38 to 45 J. Two more TPS were adopted and placed in the front side, normal to the surface and along the reflected laser propagation direction. Using foam attached targets all 4 TPS collected accelerated ions but the strongest signal, accordingly to a TNSA scheme, was always measured by the one placed normal to the rear surface.

In this campaign the effect of pulse duration on the acceleration process was also studied. This was possible adjusting the gratings distances in the compression stage of CPA (see chapter 1.1). We remind how a non-optimal compression leads to a chirped pulse. This, not only modifies the temporal duration, but also determines which spectral component of the laser beam interacts first with the target. To the best of our knowledge this interaction regime has never been approached experimentally or numerically.

In the 2015 campaign the configuration of the TPS spectrometers was slightly changed with the aim of increasing the signal-to-noise ratio. The diameters of collimators placed at the entrance of the TPS were lowered from 0.37 mm to 0.28 mm in order to reduce the thickness of the parabolic traces. The resolution of the CCD cameras was improved from 51 to 156 pixel/mm^2. Also the MCP was upgraded, increasing its sensitivity by a factor 16.

However these changes paradoxically lowered the signal-to-noise ratio. The smaller collimators enabled less particles to enter in the spectrometer and the increase of the resolution of the CCD cameras increased the impact of statistical fluctuations and thus statistical noise. Unfortunately, the higher noise covered the low intensity component of the ion spectra which is also, due to TNSA exponential behavior, the most energetic one.

As a consequence, we could not quantitatively compare 2014 and 2015 results since lower cut-off energies were recorded in the latter campaign under similar experimental conditions. Nonetheless, 2015 experiments still provided useful information regarding the qualitative dependencies of TNSA with both SLTs and MLTs.

4.3 Experimental results

We here report the results of the two experimental campaigns carried out at PULSER laser facilities. Due to the issues presented in 4.2.3, we could not perform a full analysis on the 2015 campaign we thus present the more solid results. One of the main goals of the experimental campaigns was to prove that MLTs could enhance TNSA in the high laser intensity regime ($I > 10^{19}$ W/cm^2) and to find optimum target configurations for ion acceleration.

4.3.1 Evidences of enhanced-TNSA

The first and crucial part of our analysis was aimed at supporting our hypotheses of foam-enhanced TNSA. In the parallel and independent study in [73], despite similar experimental conditions to those of our campaigns (in terms of both target used and laser parameters), the authors reported a significant difference in the accelerated ions spectra with respect to traditional TNSA.

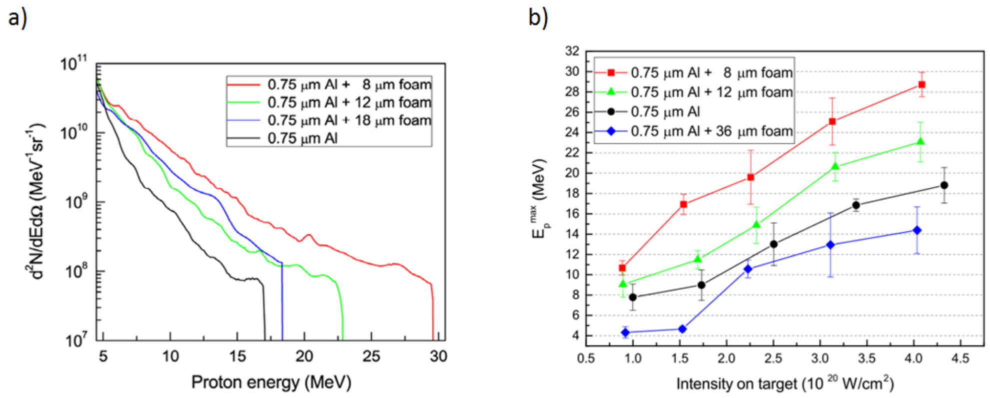

Figure 4.5: *Maximum ion energy as function of the foam thickness. The results refer to a 0.75 μm thick SLT and a MLTs composed of 0.75 μm thick Al foils covered with 3âĂŞ36 μm thick foams irradiated for the maximum laser intensities. a) Representative ion spectra obtained at the highest intensity explored in 2014 ($I = 4.5 \cdot 10^{20}$ W/cm^2) for SLT (black line) and MLT with 8 μm (red line), 12 μm (green line) and 18 μm (blue line) thick foams. b) E^p_{max} is reported as a function of the laser intensity in S polarization for SLT (black circles) and MLT with 8 μm (red squares), 12 μm (green triangles) and 36 μm (blue diamonds) thick foams. c) 2014 results: E^p_{max} and E^C_{max} are shown as function of the foam thickness for S- (blue squares), P- (red triangles) and C- (black circles) polarization. d) 2015 results: E^p_{max} is shown as a function of the foam thickness for P- (red triangles) at 30° incidence angle and C- (black circles) polarization at normal incidence.*

In figure 4.5.a we report typical spectra recorded in our campaigns. A quasi exponential decrease with a high energy cut-off was observed in all conditions explored in our work in both MLT and SLT cases. Moreover, as clearly seen in figure 4.5.a, a remarkable increase in both the cut-off energies and total accelerated charge with respect to Aluminum SLTs was measured.

Consistently with section 2.1.1, TNSA ions are strongly collimated along the direction normal to the target. To support our claim of enhanced-TNSA, we expected ions to be collected mostly by the TPS placed in this direction (TPS2 and TPS4 in fig. 4.4). Indeed, as presented in fig. 4.6, the TPS placed on the rear side along the laser propagation direction (TPS1) reported no detectable signal with SLTs, while a feeble one, just above the statistical noise, was captured in several shots with MLTs. On the other hand, clear parabolic traces were recorded in all experiments with the normal to the surface TPS (TPS2).

In conclusion, the exponential spectra with a high energy cut-off and the good collimation of accelerated ions along the normal direction made us conclude that our experiments could be interpreted in the framework of a foam-enhanced TNSA mechanism.

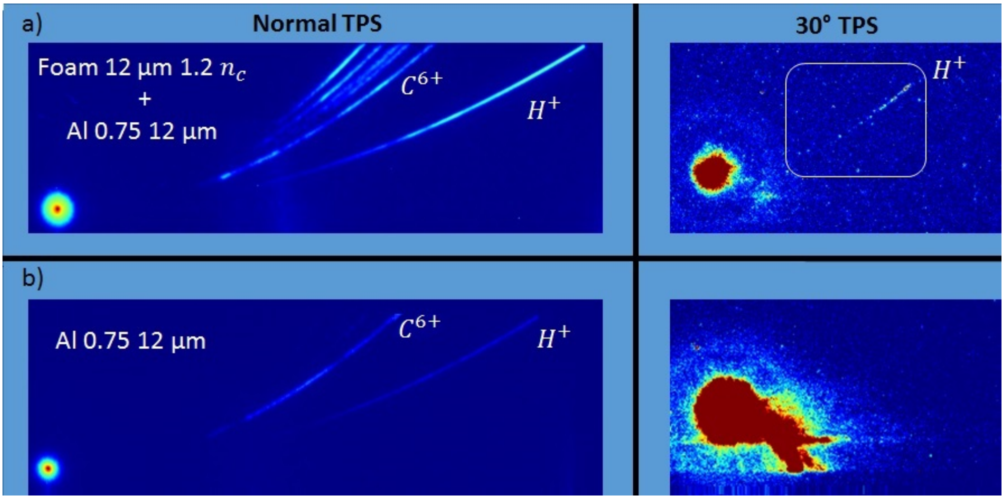

Figure 4.6: *Typical parabolic traces recorded with TPS in the 2014 campaign. On the left ions collected by the TPS normal to the rear surface are shown, on the right measurements from the TPS placed at* 30° *with respect to the rear normal (image obtained with a higher magnification). a) MLT composed by 12 µm foam 1.2* n_c *on a 0.75 µm Al substrate, b) SLT 0.75 µm Al.*

4.3.2 Role of foam thickness

A first parameter of utmost relevance in ion acceleration with MLTs is the foam thickness. With thicker ones a large fraction of the laser energy is lost to heat electrons that are too distant from the rear surface to efficiently contribute to the charge displacement at the non-irradiated surface and, thus, to ion acceleration. In contrast, with thinner foams only a modest increase in the laser absorption with respect with SLTs is to be expected. A tradeoff between these two regimes was predicted. Nonetheless, the numerical study presented in [123] suggested an optimum thickness of 8-10 μm. Using these results as a guideline for the experimental work, foams were grown in a thickness (and density) range compatible with the cited work. The first experimental campaign explored foam thicknesses ranging from 8 to 36 μm with bare Al targets as benchmarks. In 2015 thinner foams were tested (3-5μm) to further extend the analysis. In fig. 4.5.a typical spectra recorded by the normal to the rear surface TPS are presented. As seen in 4.3.1, all the measured spectra are consistent with an enhanced TNSA scheme. Moreover, the cut-off energy as well as the total accelerated charge are strongly dependent to the foam thickness. The former dependence is well shown in fig. 4.5.b, where the proton maximum energy is plotted as a function of the laser intensity for different target

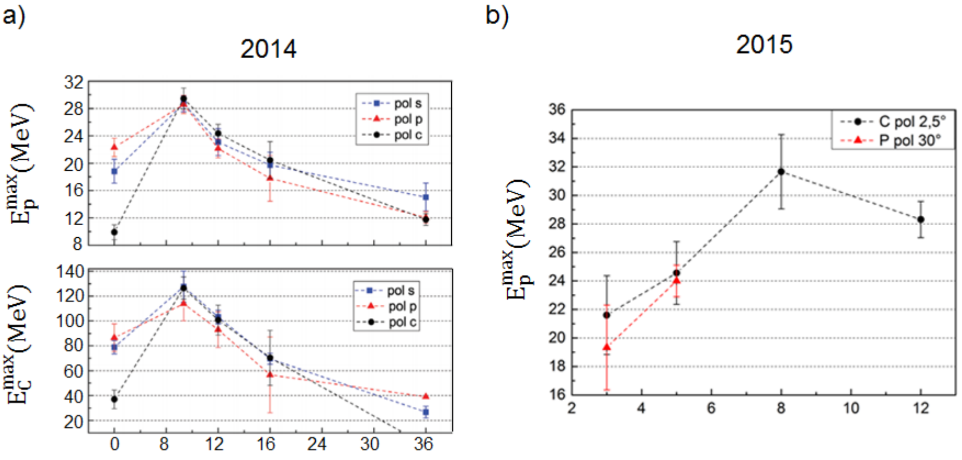

Figure 4.7: *Maximum ion energy as a function of the foam thickness. The results refer to a 0.75 μm thick SLT and a MLTs composed of 0.75 μm thick Al foils covered with 3âĂŞ36 μm thick foams irradiated for the maximum laser intensities. a) 2014 results: E^p_{max} and E^C_{max} are shown as a function of the foam thickness for S- (blue squares), P- (red triangles) and C- (black circles) polarization. b) 2015 results: E^p_{max} is shown as a function of the foam thickness for P- (red triangles) at 30° incidence angle and C- (black circles) polarization at normal incidence.*

configurations. These results refer to S-polarization, however, qualitatively similar ones were also reported in P- and C-pol. An enhancement of the performances with the 8 and 12 μm MLTs with respect to SLTs was systematically observed in the whole intensity range.
In this work, not only we proved how under suitable conditions MLTs can outperform SLTs but we also identified an optimum foam thickness which enhanced the proton maximum energy, in agreement with numerical predictions in [123]. In figure 4.7.a and 4.7.b the proton maximum ion energy (and Carbon) is reported as a function of the foam thickness. The 8μm foam guaranteed the best ion acceleration in both campaigns, also in different laser conditions (P-pol at 30° and C-pol at normal incidence). In 2014 protons with energies up to 33 MeV were measured at the highest intensity with 8 μm foam MLTs, while benchmark SLTs top performances in the same conditions were around 22 MeV. A near-constant gain factor $E^p_{max}(MLT)/E^p_{max}(SLT) \sim 1.5$ was observed at all laser intensities in P-polarization. It must be however remarked how considering the 8μm foam the best target for TNSA would be a rushed conclusion. Indeed, the thinner foams used in 2015 (3-5 μm) were less homogeneous and less uniform than the thicker ones and this could have led to worse performances.

As anticipated, we noticed how MLTs can also boost the total accelerated charge (N_{MLT} or N_{SLT}, depending on the target design). An enhancement of the number of high energy protons (E_p>8 MeV) per solid angle unit (sr^{-1}) was measured with 8 and 12 μm foams. For the first target $N_{MLT} \sim 3.4 \cdot 10^{10}$ sr^{-1}, while it decreased to $\sim 1.2 \cdot 10^{10}$ sr^{-1} with the 12 μm foam. An interesting fact is that N_{MLT} for the 18μm foam ($1.7 \cdot 10^{10}$ sr^{-1})) was found to be about four times higher than the SLT case ($3.9 \cdot 10^{10}$ sr^{-1}), despite having roughly the same maximum energies.

These enhancements were also greatly dependent to the laser polarization and will be further discussed in the following section.

4.3.3 Role of the laser polarization

Another important aspect of our experimental activity was a proper study of the effect of laser polarization in laser driven ion acceleration. As anticipated, this parameter was known to be remarkably relevant in laser-plasma coupling, however very few experimental works addressed this problem properly.

In our work we investigated the effect of three laser polarizations (P-,S- and C-pol) on TNSA with both SLTs and MLTs in a wide range of laser intensities. In figure 4.8 we present the comparison of the proton maximum energy between 8μm foam MLTs and SLTs at different laser polarizations and intensities.

First of all, in all our cases of study, an almost linear dependence on the laser intensity was found. This was already observed in literature with SLTs and fs laser durations but this is the first time it was reported with advanced MLTs. This also supports the claim made in section 4.3.1 of an enhanced TNSA regime.

As expected, laser polarization deeply influences TNSA with SLTs, due to the different heating mechanisms active. As explained in section 2.1.3, the best laser-plasma coupling is achieved with P polarization due the combined effect of $\mathbf{j} \times \mathbf{B}$ heating and Brunel effect, leading to higher proton energies. At high intensities ($I > 10^{19}$ W/cm^2) $\mathbf{j} \times \mathbf{B}$ (active in P- and S-, suppressed in C-pol) proves to be more efficient than Brunel effect (present in P- and C-pol) and explains why more energetic ions have been collected in S-pol with respect to C-pol.

In contrast with the SLTs case, with MLTs laser polarization seems to not affect ion acceleration. This is an interesting aspect since it allows the relaxation of an experimental parameter. We supposed that such behavior is due to the nanostructure of the foam layer: an irregular surface leads

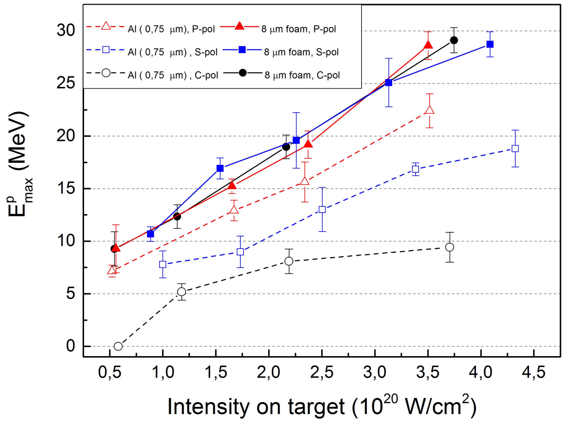

Figure 4.8: *Role of the laser polarization.* E^{p}_{max} *is reported as a function of the laser intensity for the 0.75* μ*m SLT (dashed lines) and MLT with 8* μ*m foam (full lines) in P polarization (red), S polarization (blue) and C polarization (black)*

to multiple-random incidence angles which tends to smooth polarization effects.

In agreement with section 4.3.2, we observed a noticeable increase of high energies protons with MLTs which was deeply influenced, not only by foam composition as in 4.3.2, but also by the laser polarization. In table 4.4 the gain factors N_{MLT}/N_{SLT}, using 8 μm foam MLTs, are reported for P-, S- and C-polarization at different energy intervals. We remark how the polarization dependence of this ratio is related to the strong influence of this parameter on SLTs spectra. As anticipated, MLTs ions are weakly influenced by laser polarization. Even in the worst case scenario of P-pol, an increase of about 60% in the total number of protons in the energy interval 8-10 MeV was found. We also reported a variation of the proton temperature (estimated by an exponential fit of the high energy part of the spectra), being 5.1, 4.9 and 7 MeV for S-, P- and C-pol for MLTs and 2, 2.7 and 0.8 MeV for SLTs.

4.3.4 Role of substrate thickness and foam density

It is well known from literature [90,163] that TNSA performances rely on the solid substrate thickness. Indeed, thinner foils could massively amplify both ions maximum energies and total number, especially in high laser contrast regimes. However, thicker targets ($\sim$ 1-10 μm) would be

Energy interval **MeV**	N_{MLT}/N_{SLT} **P-pol**	N_{MLT}/N_{SLT} **S-pol**	N_{MLT}/N_{SLT} **C-pol**
8-10	7.1	1.6	7.9
8-E^p_{max}	8.7	1.7	20.5
14-16	12.9	1.8	X
14-E^p_{max}	22.4	2.7	X

Table 4.4: *Ratio between the accelerated charge with foam-attached targets (N_{MLT}) and the same quantity with SLT (N_{SLT}) under the same laser intensity for different polarizations and energy intervals considered. These results were obtained in the 2014 campaign at the highest intensity achievable in each polarization.*

easier to handle in actual experiments and possibly cheaper than submicrometric ones.

In fig. 4.9 we report preliminary results obtained in the 2014 campaign. The proton cut-off energy is plotted as a function of the laser intensity (in S-pol) for five different target configurations. Three MLTs were tested: two composed by a near-critical ($\sim 1.2n_c$), 12 μm thick foam over two different Al substrates 0.75 and 1.5 μm thick, respectively, and a third characterized by a higher foam density ($\sim 4.3n_c$) on the thinner 0.75 μm substrate. Results with MLTs were benchmarked against Al targets 0.75 and 1.5 μm thick.

In agreement with results in literature, the thicker SLTs was characterized by lower performances. On the other hand, the 2014 exploratory study reported no significant differences between MLTs with different substrates. At this purpose in 2015 a more extensive study has been carried out. In figure 4.10.a we present several results obtained with a wider range of substrates. Several aspects must be highlighted. First of all, comparable cut-off energies of $\sim$ 15 MeV were measured with MLTs with a thick foil of 12 μm and 0.75 μm SLTs. This aspect is interesting due to the fact that thick substrates are particularly suitable, due to their higher mechanical robustness, for applications which require high repetitions rates.

Unfortunately no data with thick SLTs were available for a proper comparison with MLTs. Nonetheless, we adopted the theoretical model in section 3.1.2, combined with ref. [90] to estimate the proton cut-off energy at different foil thicknesses. With a 12 μm bare Al target energies not exceeding 5 MeV are to be expected, less than a third of the experimental measurements with MLTs. In fig. 4.10.b we combined experimental results in [136], which refer to an experimental campaign at the PULSER laser facility (i.e. similar laser conditions) with flat foils of different thicknesses (10nm-100nm), with our measurements in S polarization and similar laser

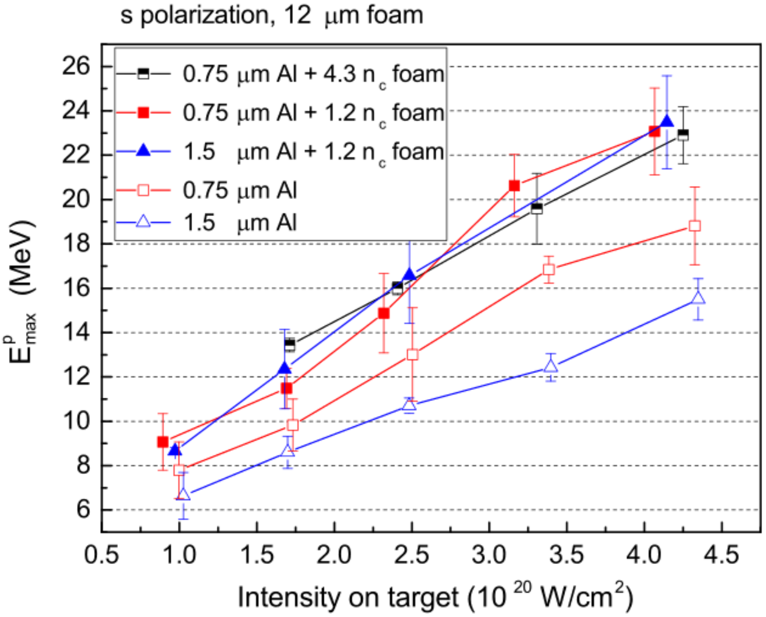

Figure 4.9: *Role of Al foil thickness, foam density and laser intensity. Results refer to 0.75 μm and 1.5 μm thick SLT (red open squares and blue open triangles, respectively); MLT composed of 12 μm thick near-critical foams and Al foils with a thickness of 0.75 μm (red squares) and 1.5 μm (blue triangles); MLT composed of 12 μm thick foam with density $n \sim 4n_c$ and Al foil with the thickness 0.75 μm (half-filled squares). E^p_{max} is reported as a function of the laser intensity for S-polarization.*

intensity ($\sim 3.3 \cdot 10^{20} W/\mathrm{cm}^2$). These are compared with theoretical predictions of the quasi stationary model in [90]. Indeed the good agreement seen in fig. 4.10.b proves the reliability of analytical estimations in fig. 4.10.a.
As a final remark, in the 2014 campaign we also performed several shots with MLTs with different foam densities of $1.2n_c$ and 4.3 n_c. In this first test we observed no variations between the two targets (see fig. 4.9). These shots were performed at laser intensities in the interval $1.7 \cdot 10^{20} - 4.3 \cdot 10^{20}$ W/cm^2 which correspond to values of $a_0 \geq 9$. In such conditions both foams were relativistic transparent to the laser beam, this could be a possible explanation for the similar experimental results obtained.

4.3.5 Role of the gratings distance

In the 2015 experimental campaign an exploratory attempt to investigate the effect of the pulse duration in ion acceleration with both SLTs and

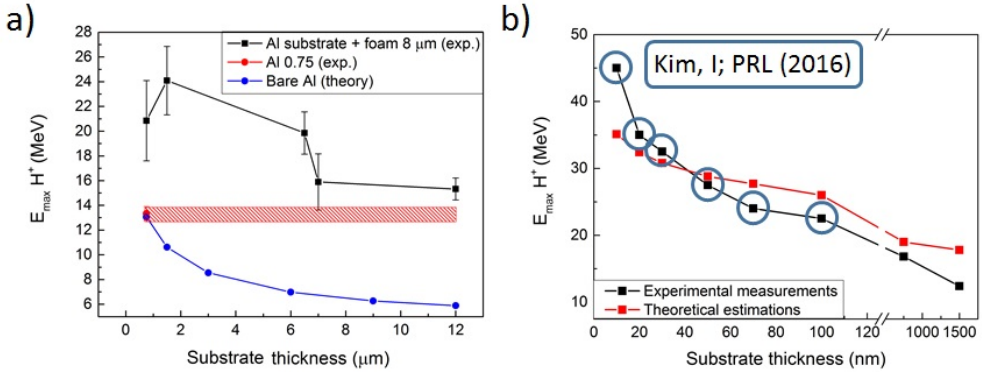

Figure 4.10: *Role of solid substrate. a) Results refer to 0.75 μm SLT and MLT composed of 8 μm foam over a 0.75-12 μm substrate. Experimental results with MLT, E^p_{max} as a function of the substrate thickness are reported (black line). As reference results with 0.75 μm SLT are shown (red) as well as a theoretical prediction of E^p_{max} at higher thicknesses. b) Comparison between theoretical predictions (red) with the TNSA model in [90] and experimental results (black) reported in [136] (circled) combined with the ones in fig. 4.9. These results were obtained in the same laser facilities under similar experimental conditions: same pulse duration, intensity ($\sim 3.3 \cdot 10^{20} W/cm^2$) and focal spot, in S polarization. The different incidence angles (7° and 30°, respectively) should not significantly influence E^p_{max}.*

.

MLTs was made. To tune the pulse length the gratings used in the CPA stage were moved from their optimum chirp position (0 μm). The pulse duration was then tuned between 30 and 150 fs, keeping the energy on target fixed and, thus, lowering the peak intensity. This also changes the frequency components of the electric field that interact first with the target (high frequencies with a positive displacement), this could cause possible asymmetries of measurements between positive and negative displacements.

In figure 4.11 we present the maximum ion energy as a function of the gratings displacement in C-pol at normal incidence and P-pol at 30°. It is worth to highlight how, using MLTs, the highest energies were recorded with a non perfect-chirp in both polarizations. A possible explanation is that, if the relativistic transparency condition is fulfilled ($n < \gamma n_c$), the volumetric heating could be more efficient with a longer pulse.

As seen in section 2.1.3, interaction with SLTs should be strongly hampered at lower intensities and worse ion acceleration with longer pulses was thus expected. However, quasi constant cut-off energies around 15 MeV were measured with SLTs in P-pol at 30° incidence angle. Furthermore, in C pol at normal incidence the highest energy with SLTs was recorded

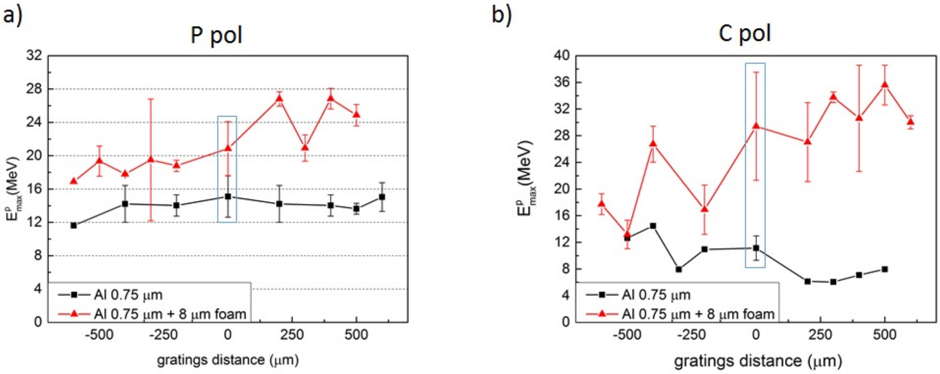

Figure 4.11: *Role of gratings distance.* E^{p}_{max} *is presented as a function of the gratings distance using 0.75* μm *thick SLT (black line) and 8* μm *thick foam MLT (red line) for a) P-polarization at* 30° *incidence angle and b) C-polarization at normal incidence*

with a down-chirped pulse given by a -400 μm gratings displacement.
It must be remarked how, due to the low number of shots and the poor pulse characterization as a function of the gratings displacement, these are just preliminary results and conclusions can not be drawn yet. Nonetheless, it is worth to highlight that this campaign opens a new possible strategy to increase laser plasma coupling with a proper pulse tailoring.

5

Advances in TNSA theory

In chapter 3 we offered an overview of the major TNSA theoretical models. We also highlighted how all of them require the estimation of quantities, such as the hot electron temperature T_h and density, extremely difficult to be directly measured in experiments, in order to predict quantities relevant for ion acceleration (e.g. the cut-off energy). Most of these works take T_h as input parameter. Consistently with section 2.1.3, T_h is determined by laser induced electron heating which is a natural consequence of ultra intense laser-plasma coupling. Due to the vastness of the topic, we focused on interaction scenarios relevant for TNSA. The aim of this chapter is to suggest simple and predictive scaling laws for T_h with both solid foils (SLT) in section 5.2 and foam attached targets (MLT) in section 5.3. These, not only will provide a more solid physical interpretation of the electron heating with respect to existing models, but will be also combined with a well known TNSA analytical model to estimate the maximum energy

Coherently with 3.3, the ponderomotive scaling $T_h[MeV] = 0.511 \cdot (\sqrt{1 + a_0^2/2} - 1)$ [105] is widely adopted in the context of intense laser interaction with SLT and is able to reproduce the dependence of T_h reported by several experimental measurements. This scaling, however, does not include laser polarization and incidence angle, which are known to heavily affect the efficiency of the two main heating mechanisms in this physical scenario: Brunel effect and $\mathbf{j} \times \mathbf{B}$ heating. Moreover, it predicts electron temperatures significantly higher than those reported in recent numerical works [166–168]. To overcome these limitations, in section 5.2.1 we propose a simple model for T_h as a function of pulse intensity, polariza-

tion and angle of incidence. In section 5.2.2 we support and complete the theoretical model with an extensive 2D and 3D numerical campaign. An interesting and natural approach in order to test our results is to combine our scaling with the quasi-stationary model in [155] to increase its predicting capabilities. Therefore, in section 5.2.3 we benchmark the theoretical estimations against the recent experimental results presented in chapter 4.
As described in section 2.2.1 an intrinsic limit of TNSA with SLTs is the low interaction efficiency ($\leq 20\%$) which also limits the electron heating and, as a consequence, ion acceleration. Coherently, in chapter 4 we explored an interesting solution to enhance TNSA with MLTs. Despite being still poorly studied theoretically, it is acknowledged that ion acceleration with these targets relies on an efficient volumetric interaction in the low density layer (see [115, 121, 122, 169, 170, 180, 181]) which naturally boosts the electron heating and, as a consequence the sheath field supported at the solid-vacuum interface. As seen in section 4.3, a significant enhancement of both total accelerated charge and maximum ion energy can be achieved with MLTs with respect to SLTs. In this thesis we propose a first attempt to model the electron temperature in these challenging conditions. In order to restrict our investigation we focus on laser and target parameters comparable to those of sections 4.1.1 and 4.2. With a similar approach to the case of SLTs, in section 5.3.1 we propose a scaling law for T_h and supported such model with the numerical results presented in 5.3.2. We will finally test the results of our scaling with enhanched TNSA experimental results reported in section 4.3.

5.1 Numerical setup

To support the theoretical analysis, we performed an extensive 2D and 3D numerical campaign with the open source Particle-In-Cell code piccante [162]. The numerical activity was carried out at the HPC BG/Q machine FERMI (CINECA, Bologna, Italy).
The high computational cost of 3D PIC simulations (easily exceeding 40k CPU hours each) prevented a proper parametric scan. Due to this fact in this work we mostly relied on 2D simulations, exploiting 3D to address several specific cases.
In this chapter we present results obtained with 0.5 μm thick solid targets with a charge over mass ratio Z/A = 1/3 (e.g. Al^{9+}), a density of $n_e = 80\, n_c$ in 2D and $n_e = 40\, n_c$ in 3D. The lower density in the 3D setup

allowed to reduce the CPU hours required for each simulation. This choice was supported by several convergence tests in 2D which proved no substantial differences in laser absorption between n_e=80 n_c and n_e=40 n_c. A thin H^+ contaminant layer (l_{cont} = 50 nm, $n_{cont} = 9\,n_c$ Z/A = 1) was placed at the rear side of the target. Along with this target configuration, in this work we assessed the role of the target thickness in the electron heating thought several 2D simulation with a 20 μm thick target with the same composition above described.

The laser pulse was Gaussian shaped in the transverse direction with $\sin^2$ temporal envelope, characterized by a pulse duration (intensity FWHM) of 25 fs, a waist of 3 μm and a wavelength of 0.8 μm. The peak intensity was varied in the range of $4.8 \cdot 10^{18}$ - $4.8 \cdot 10^{20}$ W/cm^2, which corresponds to a normalized laser amplitude $a_0 = \sqrt{\frac{I\lambda^2}{1.37 \cdot 10^{18}}} \sim 1.5$ - 15, well within the capabilities of present facilities [9].

The effect of the laser polarization in the laser plasma coupling was investigated through a vast 2D parametric scan (more than 60 2D simulations were performed) in P a C polarization at different incidence angles (0-15-30-45-60°) and intensities. It is well known that significant differences between 2D and 3D simulations can be expected. Moreover, a 2D Cartesian geometry is not suitable to reproduce S polarized beams, due to the fact that the system is homogenous in the plane where the electric field lies. To address these issues we performed several 3D simulations in S polarization at a fixed laser intensity (a_0=10) with 0-30-45° incidence angles as well as several benchmark in C and P polarization.

The spatial resolution in the 2D campaign was $\Delta x = c/2\omega_p$ and $\Delta y = c/1.5\omega_p$ evaluating ω_p for the dense foil. In 3D simulations we adopted a "moving window" configuration combined with a stretched grid in y-z axis with a constant resolution in the interaction volume of $\Delta x = \Delta y = \Delta z = c/\omega_p$. The resolution was safely lowered in 3D due to the fact that benchmark 2D simulations reported no significant differences between the two setups (less than 5 % on ion maximum energy).

The solid layer was sampled with 81 macro-electrons per cell and 9 macro-ions in 2D, while in 3D 42 macro-electrons were used. The contaminant layer contained 9 macro-electrons and 9 macro-ions per cell for both 2D and 3D simulations.

Simulations were stopped at 170 fs (60 λ/c), since most of the ion acceleration processes in 3D has taken place at this point ($\frac{dE_{max}(ions)}{dt \cdot E_{max}(ions)} < 1\%$ per laser period). In 2D simulations charged particles are actually infinite wires, thus their electrostatic potential is $\propto -ln(r)$, which leads to a slower saturation. However, $\frac{dE_{max}(ions)}{dt \cdot E_{max}(ions)}$ is still less than $< 5\%$ per laser period.

5.2 Flat solid targets

The aim of this section is to construct an effective description of the hot electron temperature arising from the interaction between ultra-intense (I>10^{18} W/cm^2) beams and micrometric ($\geq$ 0.5 μm) solid foils. Even though this topic was extensively studied in the last decades (see section 2.1.3), relevant open issues are still to be addressed. As anticipated, $\mathbf{j} \times \mathbf{B}$ heating and Brunel effect are generally accepted to be the dominant mechanisms in these conditions. However actual proofs of these two schemes are still debatable. Moreover, as explained in section 3.3, a scaling law that could properly predict the contribution of each effect is still lacking.

5.2.1 Theoretical description

In this section we propose a simple relation for the electron temperature which is given by two contributions weighted by two coefficients, so that: $T_h = C_1 T_{\mathbf{j}\times\mathbf{B}} + C_2 T_{Brunel}$. For the $\mathbf{j} \times \mathbf{B}$ term we start from the well known ponderomotive scaling:

$$T_{\mathbf{j}\times\mathbf{B}}[\text{MeV}] = 0.511 \cdot \left[\sqrt{1 + \frac{a_0^2}{2}} - 1\right]. \tag{5.1}$$

We thus made the assumption that $\mathbf{j} \times \mathbf{B}$ heating is not dependent to the incidence angle and that is well described by the ponderomotive scaling. As far as the Brunel term is of concern, no scaling laws for T_h, which could be applied in a fully relativistic regime, have been proposed. However, the simple model presented in [26] allows to estimate the interaction efficiency $\left(\eta_b = \frac{I(absorbed)}{I(incident)}\right)$ as:

$$\eta_b = \frac{1}{\pi a_0} f \left[\left(1 + f^2 \frac{a_0^2}{2} \sin^2\theta\right)^{1/2} - 1\right] \tan\theta, \tag{5.2}$$

f is the field amplification factor due to the reflection of the electromagnetic wave at the target surface. In general f depends on the absorption efficiency, being $f = 1 + \sqrt{1-\eta}$. However in all cases treated in this section the absorption efficiency is quite low ($\eta < 20\%$) thus f can be safely approximated as if the pulse reflection was perfect ($f > 1.9$). We can estimate Brunel contribution as $T_{Brunel} \propto E_{laser} \cdot \eta_b / N_e$, where N_e is the total number of electrons interacting with the laser beam. This quantity should be proportional to the typical penetration length of electromagnetic fields in dense plasmas, given by the relativistic skin depth $\lambda_{sd} = c/\omega_{pe} \cdot \sqrt{1 + a_0^2/2}$. We then obtain this expression for the Brunel term:

$$T_{Brunel}[\text{MeV}] \propto 0.511 \cdot \left[\sqrt{1 + f^2 \frac{a_0^2}{2} \cdot \sin^2\theta} - 1 \right] \cdot \tan\theta \qquad (5.3)$$

In Eq. 5.3 a factor $F = a_0/\sqrt{1 + a_0^2/2}$ should appear. However, even for modest laser intensities ($a_0 > 3$) this term approaches a constant. Combining Eq.5.1 and Eq.5.3, we propose the following scaling law for T_h which is able to take into account both $\mathbf{j} \times \mathbf{B}$ and Brunel effect:

$$\begin{aligned} T_h[\text{MeV}] = {} & C_1(a_0, pol, l_{foil}) \cdot 0.511 \cdot \left[\sqrt{1 + \frac{a_0^2}{2}} - 1 \right] + \\ & C_2(a_0, pol, l_{foil}) \cdot 0.511 \cdot \left[\sqrt{1 + f^2 \frac{a_0^2}{2} \cdot \sin^2\theta} - 1 \right] \cdot \tan\theta \end{aligned} \qquad (5.4)$$

where $C_1(a_0, pol, l_{foil})$ and $C_2(a_0, pol, l_{foil})$ are the weights of $\mathbf{j} \times \mathbf{B}$ heating and Brunel effect respectively, depending in principle on the laser polarization, intensity and target thickness. However, we assume to have included most of the dependence on the laser intensity and incidence angle explicitly in Eq. 5.4 and, thus, we expect C_1 and C_2 to be quasi-constant with respect to a_0. Our model can be adopted to estimate the electron temperature if the two coefficients are provided. Nonetheless, the relative weights of the two heating effects depend on aspects of laser-plasma coupling not included in our model which can not be easily assessed with a simple analytical approach. We therefore developed dedicated PIC simulations in order to obtain reliable estimations of the C_1 and C_2 coefficients. In addition, numerical simulations can allow to provide evidences, required to properly use our model, to check whether the $\mathbf{j} \times \mathbf{B}$ heating and Brunel effect dominate over other heating schemes in experiments with flat foils irradiated by high intensity (I>10^{18} W/cm^2) lasers.

5.2.2 Numerical investigation

We performed a numerical parametric scan at different laser intensities, polarizations and incidence angles with a micrometric (0.5 μm) solid foil. As anticipated the aim of this investigation is to support our theoretical model, in particular, it is of crucial importance to achieve a proper estimation of the C_1 and C_2. The electron temperature will be extracted from a large set of 2D and 3D PIC simulation and Eq. 5.4 will be used to fit these results with the two coefficients as free parameters. At this regard, it must be remarked that the simulation dimensionality is likely to influence numerical results, with a 3D simulation being obviously more representative of the actual physical process. However a parametric scan using 3D PIC simulations would have cost a massive amount of CPU hours and could not be performed. Nonetheless, from the the comparison of few but representative 2D and 3D results, we noticed that electron temperature ratio $R = T_h(2D)/T_h(3D)$ was weakly dependent to parameters such as intensity and incidence angle (less than 10% in our cases), but somehow sensible to the laser polarization, being $R(P\ pol) \sim 1.5$ and $R(C\ pol) \sim 1$. We thus assumed that P and C-pol 3D temperatures (and thus C_1 and C_2) could be estimated in all conditions not directly simulated through $T_h(2D)$/R. In fig. 5.1 we present a typical 2D simulation: the electron density is shown paired with the electromagnetic energy density at different stages of TNSA. The electron spectra were analyzed after the interaction with the laser beam (fig. 5.1.c-d), considering only trapped particles inside the target and in a Debye length at the interfaces. In fig. 5.2.a we report representative output observed in our simulations at different incidence angles and polarizations. It must be noticed how electrons total number, mean and maximum energies are deeply influenced by laser conditions, the best coupling being achieved in P polarization at high incidence angles.

A key hypothesis to obtain Eq. 5.3 was the direct proportionality between the electron temperature and the heating efficiency. At this purpose, these quantities were extracted at different experimental conditions (as seen in section 3.2.2) and their scaling laws to laser parameters were compared. In fig. 5.2.b a typical result is reported: for low incidence angles $\theta \leq 45°$ our assumption holds. On the other hand, at higher values the proportionality is broken, thus, our models fails to describe this specific scenario. In fig 5.3 T_h is shown for the three laser polarizations as a function of the incidence angle in a broad range of laser intensities. A clear trend with respect to beam parameters was found and proved to be compatible with Eq. 5.3. In this scheme, at normal incidence the electron heating is caused

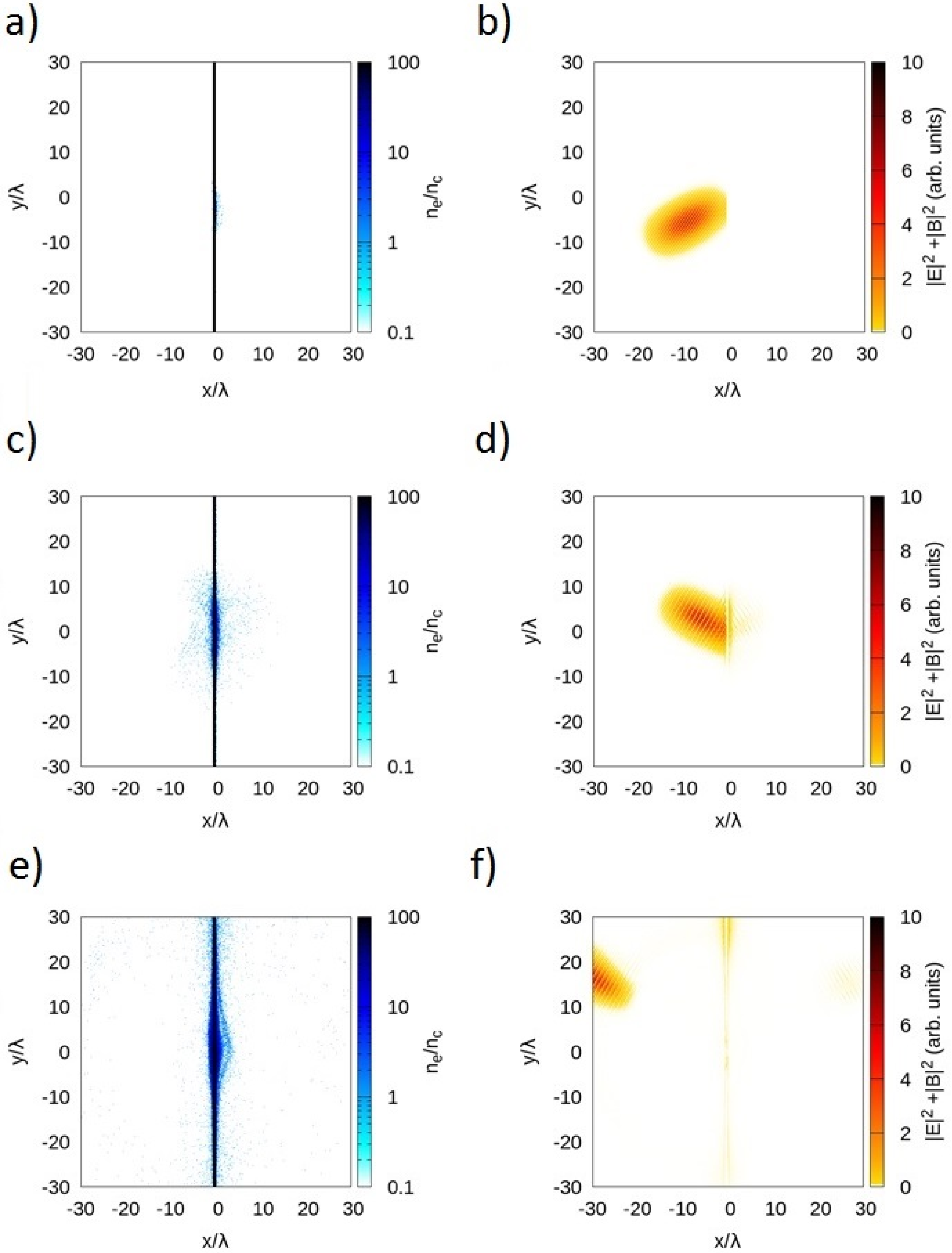

Figure 5.1: *Numerical simulations with SLT. The electron density (a,c,e) and the electromagnetic energy density (b,d,f) are reported at three different temporal frames: the beginning of laser-plasma interaction (12 fs, shown in a,b), the instant when the electron energy reaches its peak (50 fs, shown in c,d) and the onset of ion acceleration (110 fs, shown in e,f).*

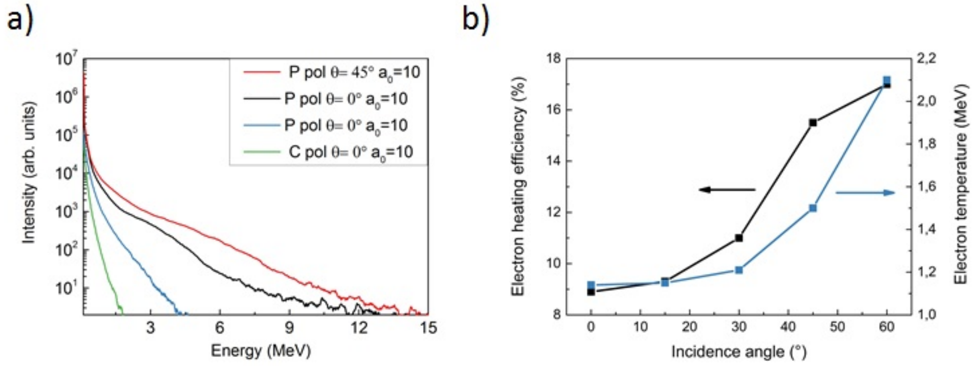

Figure 5.2: *a) Samples of electron spectra obtained at fixed laser intensity ($a_0 = 10$) with P polarized laser pulses at 45° (red) and normal (black) incidence and C polarization at 45° (blue) and normal (green) incidence. b) Electron temperature (blue) and electron heating efficiency (black) as a function of the laser incidence angle using a P polarizared beam with $a_0 = 10$.*

by $\mathbf{j} \times \mathbf{B}$ heating only. The temperature growth at higher incidence angles can be attributed to the increasing component of the normal to the surface electric field (in P and C pol) $\sim E_0 \sin(\theta)$. This simple physical picture is also consistent with the 3D results in S polarization which reported no significant variations on T_h with respect to the the incidence angle. It is worth to stress that, in agreement with recent works [166–168], our results confirm that the ponderomotive scaling largely overestimates the electron temperature (e.g. $T_{pond}(a_0 = 10) = 3.1 MeV$) in all our cases of study.

In this work we also performed a few tests to approach the study of the influence of target thickness on electron heating. In agreement with section 2.1.2, as hot electrons cross the non irradiated surface a sheath field generates which can back reflect them into the target. If the target is sufficiently thin (depending on the pulse duration) these electrons can further interact with the laser, gaining more energy. In our simulations we adopted two different target configurations: 0.5 μm target (thin), thick enough to suppress relativistic transparency (which can take place when the relativistic skin depth exceeds the actual thickness of the target) at all explored intensities, and a 20 μm one (thick), still suitable for laser induced ion acceleration experiments. In the former case each electron is predicted to interact multiple times with the laser beam, while in the latter case the traveling time of a relativistic electron in a full round trip through the target is greater than the actual pulse duration. In fig. 5.4 we report two representative electron spectra. It is worth to highlight how

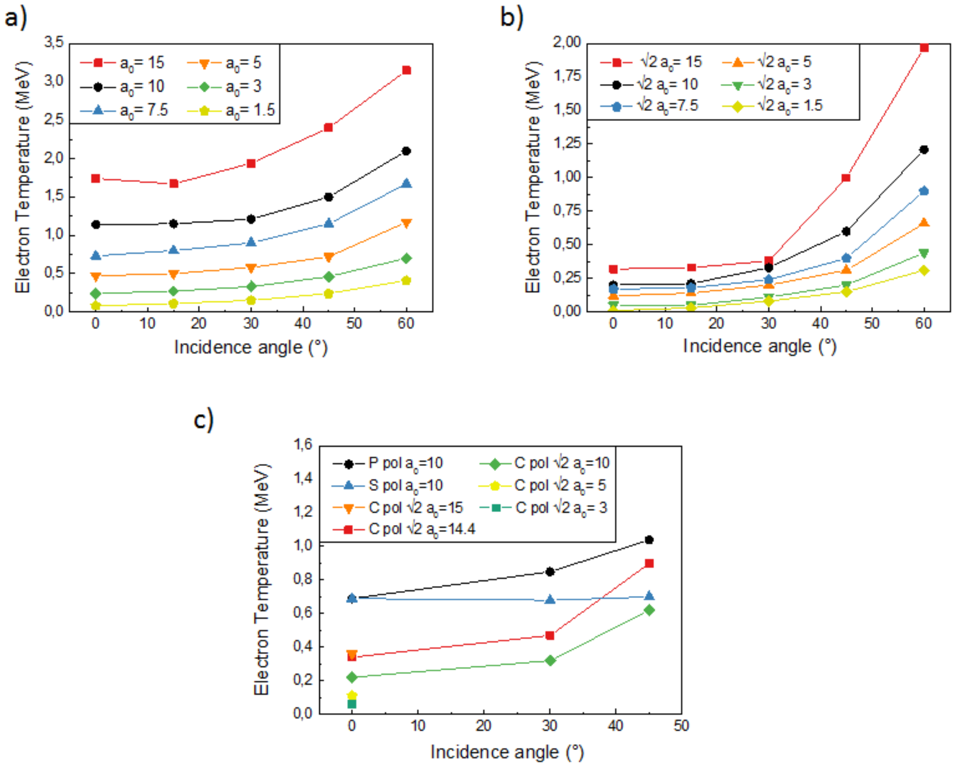

Figure 5.3: *Electron temperature for an irradiated plain solid target ($l_{foil} = 0.5\mu m$, $n_e(2D) = 80n_c$, $n_e(3D) = 40n_c$) as a function of the incidence angle at different laser intensities: a) P polarization b) C polarization c) 3D results.*

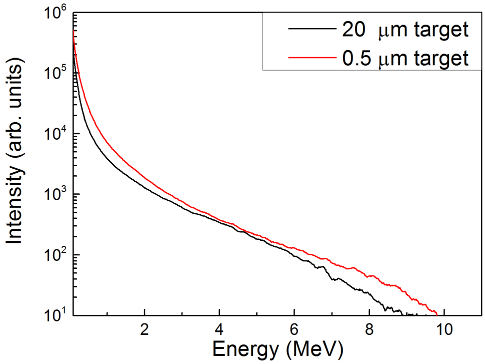

Figure 5.4: *Electron spectra observed in simulations with a 0.5μm (red) and 20 μm (black) thick SLT. These results refer to the exact temporal frame and laser conditions.*

the electron temperature decrease was less than 20% despite a 27 times thicker target.
Numerical simulations also allow to track particle trajectories, which can provide useful insights on the physical processes at play. Fig. 5.5.a and 5.5.b show some representative electron trajectories for both targets. In the thin case, in fig. 5.5.a, electrons are reflected multiple times in the target while in the thick case they travel freely into the plasma as they are injected by the laser. The stronger confinement of electrons in the thin target with respect to the thick one is evident, leading to a denser electron cloud and thus to a more efficient ion acceleration, which is compatible with the theoretical description in [90] and in agreement with experimental results in fig. 4.10.b.

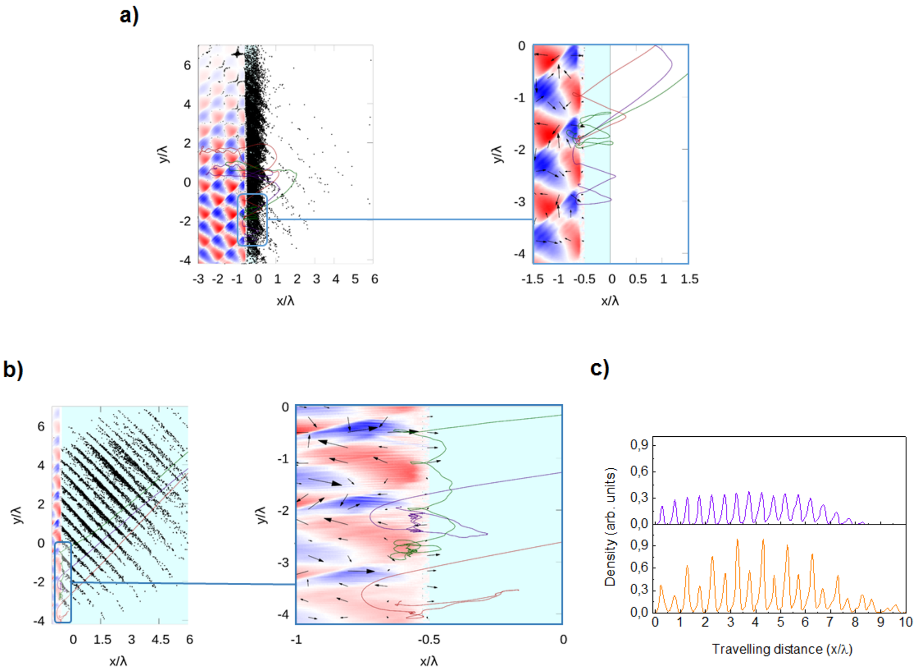

Figure 5.5: *Trajectories of 3 test electrons (colored lines) with energy above 3 MeV after the interaction with a laser beam of* $a_0 = 10$ *at* 45° *incidence with a) 0.5* μ *m thick target and b) 20* μ*m. The magnetic field component* B_z *(red and blue color scale) and electric field (black vectors) are taken at the injection time. The black dots represent all the electrons with an energy above 3 MeV. c) Electron density along the laser propagation axis at normal (upper figure) and* 45° *incidence angle (lower figure).*

Electron recirculation leads to random re-injections, making trajectories hard to interpret. Thus, some features of the interaction can be seen

more clearly in the thick target. Fig. 5.5.a and 5.5.b show that electrons undergo i) small normal oscillations near the surface ii) extraction in vacuum over distances of the order of the Debye length iii) a strong kick along the incidence angle iv) injection in the target.
As seen in fig. 5.5.b electron bunches can freely propagate through the 20 μm target. In fig. 5.5.c we show the hot electron density along the propagation axis calculated integrating electrons in the orthogonal plane with energies $\geq T_h$. The upper graph shows electron bunches injected at 2ω with a spatial envelope similar to that of the pulse, which is a clear signature of $\mathbf{j} \times \mathbf{B}$ heating. In the lower graph, electrons are injected at 2ω, but it is evident that higher peaks appear with a frequency equal to ω which can be directly linked to the Brunel effect.
Numerical results obtained in this campaign allowed us to support our claim of combined heating effect. Moreover, the wide and controlled numerical dataset was exploited to obtain C_1 and C_2 coefficients of Eq. 5.4 which could not be otherwise easily evaluated with theoretical methods.

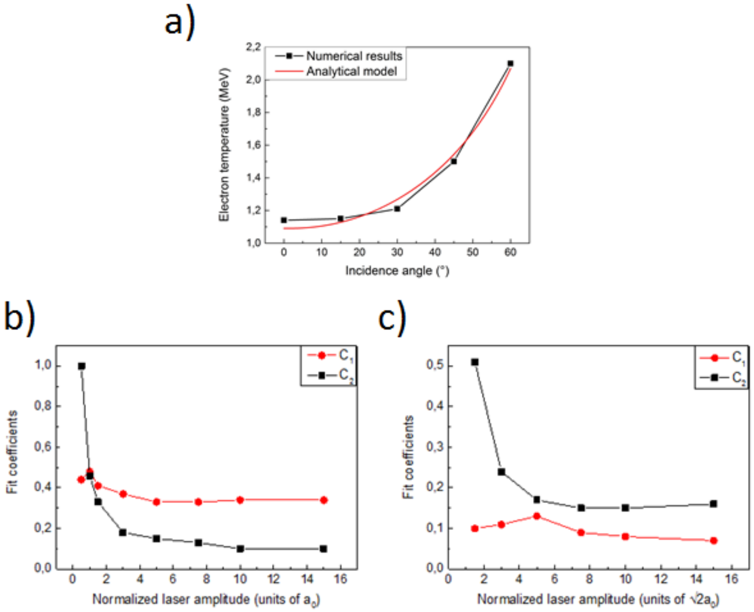

Figure 5.6: *a) Comparison between the electron temperature observed in simulations (black squares) at different incidence angles using a P polarized beam ($a_0 = 10$) and the numerical fit with Eq. 5.4 (red line). b-c) C_1(2D) and C_2(2D) coefficients as a function of the laser intensity for: a) P polarization, b) C polarization.*

For each simulated laser intensity, a fit of T_h was performed, using Eq.

5.4 as the fit function and leaving C_1 and C_2 as free parameters. As shown in fig. 5.6.a, a very good agreement was found in all our cases of study. In fig. 5.6.b, 5.6.c the two coefficients are shown as a function of the laser intensity. They are nearly constant for normalized laser intensities exceeding $a_0 = 3$. This confirms that our model includes most of the laser intensity dependency explicitly. At low intensity, an implicit dependence on the laser intensity in C_2 appears. In this condition ($I < 10^{19}$ W$/cm^2$) other heating mechanisms are expected to become relevant, as reviewed in section 2.1.3. Indeed, our combined heating model does not include all the physical processes at play. Based on these results we consider the following estimates to be reliable for $a_0 > 3$ intensities, achievable with sub 100 TW laser facilities:

	P	**C**
$C_1(2D)$	0.33	0.1
$C_2(2D)$	0.06	0.16

Table 5.1: *2D numerical coefficients for SLT for P and C polarization*

3D simulations provide the best estimation for the electron temperature and are essential for S polarization. We thus selected a few representative cases for C and P polarization and observed that, as previously mentioned, the ratio $R[P\,pol] = T_h(2D)/T_h(3D) = 1.5$ and $R[C\,pol] = 1$ are weakly dependent on laser parameters. To obtain reliable estimation for $T_h(3D)$, we estimate $C_{1,2}(3D)$ coefficients as $C_{1,2}(2D)/R$. As far as S polarization is concerned, since no dependence on the angle of incidence is observed $C_2 = 0$. At 0° incidence S and P polarization are indistinguishable, then $C_1(P) = C_1(S)$. This procedure leads to:

	P	**S**	**C**
C_1(3D)	0.22	0.22	0.1
C_2(3D)	0.04	0	0.16

Table 5.2: *3D numerical coefficients for SLT for the three polarizations*

Experiments would be the most natural solution in order to test our scaling law. Nonetheless, in agreement with section 3.3 it is extremely challenging to obtain a fs-resolved direct measurement of electron temperature. Therefore, to benchmark our model we relied on experimental data of the cut-off energy of laser-driven accelerated ions in chapter 4. As anticipated at the beginning of this chapter, we compared them with the theoretical predictions of the TNSA model in [155] obtained with our new scaling law.

5.2.3 Benchmark of theoretical estimation and experimental results

Eq. 5.4 can be combined with the values given in tab. 5.2 and ion acceleration models to provide more accurate predictions as well as adding new features regarding hot electron physics not included in previous descriptions. In the specific case reviewed in section 3.1.2 the ion cut-off energy can be evaluated through:

$$E_{max} = Ze\phi(x=0)T_h = ZT_h\left[\varphi^* - 1 + \frac{\beta(\zeta,\varphi^*)}{I(\varphi^*,\zeta)e^{(\zeta+\varphi^*)}}\right], \tag{5.5}$$

we remind how φ^* was obtained fitting several experimental data, assuming the ponderomotive scaling for T_h. However, in all our cases of study $T_h < T_{pond}$. Indeed, φ^* must be changed accordingly in order to be compatible with the new scaling law. It can be achieved noticing that, at normal incidence in P- and S- polarization, Eq. 5.4 and the ponderomotive scaling differ just for a constant factor. However, estimations with the two scaling laws must lead to the same result:

$$\begin{aligned} 0.511\cdot\left(\sqrt{1+a_0^2/2}-1\right)\left[\varphi^*_{\text{old}} - 1 + \frac{\beta(\zeta,\varphi^*_{\text{old}})}{I(\varphi^*_{\text{old}},\zeta)e^{(\zeta+\varphi^*_{\text{old}})}}\right] = \\ C_1\cdot 0.511\cdot\left(\sqrt{1+a_0^2/2}-1\right)\left[\varphi^*_{\text{new}} - 1 + \frac{\beta(\zeta,\varphi^*_{\text{new}})}{I(\varphi^*_{\text{new}},\zeta)e^{(\zeta+\varphi^*_{\text{new}})}}\right], \end{aligned} \tag{5.6}$$

where φ^*_{new} and φ^*_{old} are the values of φ^* with the new scaling law and the ponderomotive one, respectively. Eq. 5.6 is numerically solved and the computed value of φ^*_{new} will be then used under experimental conditions (laser polarization and incidence angle) not taken into account by the old ponderomotive scaling.

To test our results we used our expression of T_h with C_1 and C_2 in table 5.2, combined with Eq. 5.5 and compared its predictions with experimental results with SLTs reported in fig. 4.8.

In fig. 5.7.a the comparison in P polarization revealed that predictions with our scaling law are closer to experimental data than those obtained with the ponderomotive scaling. As far as results for S polarization are of concern (fig. 5.7.b), no further improvements have been made since in

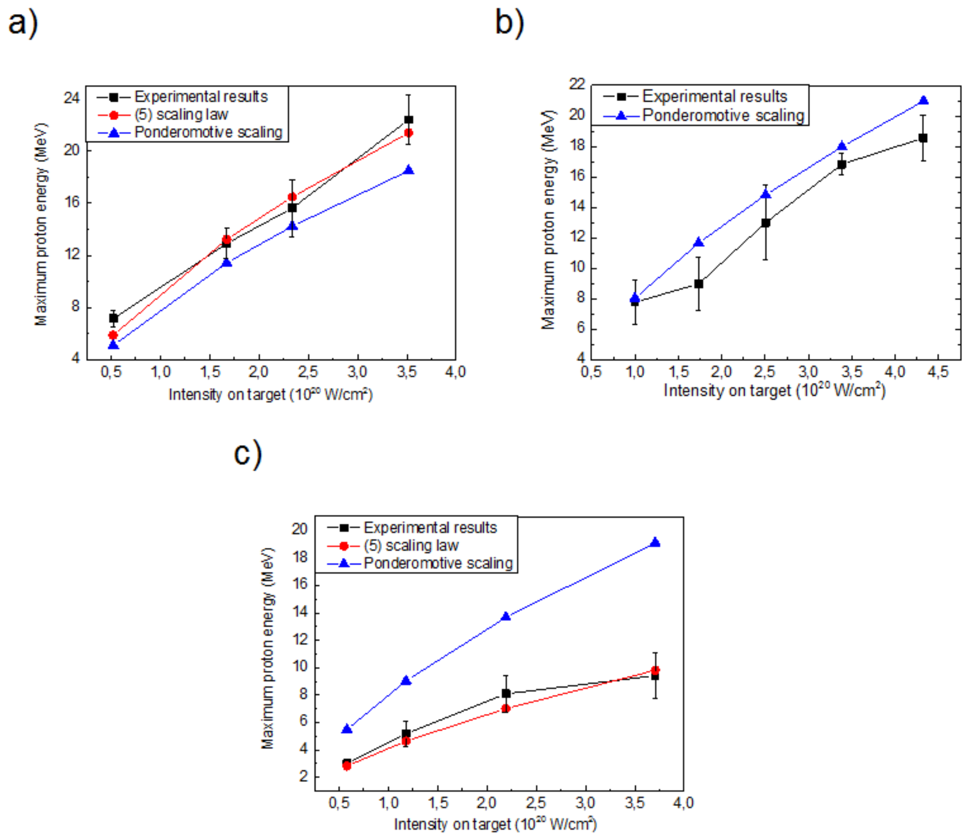

Figure 5.7: *Comparison between experimental results in section 4.3 (black squares) and the quasi-stationary analytical model using the ponderomotive scaling (blue triangles) and the scaling 5.4 (red circles) for: a) P polarization, b) S polarization and c) C polarization.*

S polarization Eq. 5.4 retains the same expression of the old law (C_2=0). This was expected since $\mathbf{j} \times \mathbf{B}$ is the main heating mechanism active and was already described by ponderomotive scaling up to a constant factor “absorbed" in φ^*. Finally, in C polarization $\mathbf{j} \times \mathbf{B}$ heating is suppressed ($C_1 = 0.1$), the ponderomotive scaling greatly overestimates the actual temperature and, as a consequence the proton cutoff energies. On the other hand our model, which takes into account both heating mechanisms, allows to have a good prediction even in this case.

5.3 Foam-attached targets

In agreement with section 2.2.1, novel foam attached targets rely on the efficient laser-plasma energy coupling in the near-critical plasma, formed in the low density layer, to boost ion acceleration. Experimental observations in section 4.3.1 were coherent with our hypothesis of enhanced TNSA. The natural approach adopted in this section to extend TNSA theoretical descriptions to MLTs is through a suitable scaling law for the electron temperature which could take into account the different interaction mechanism. In this framework, dedicated numerical simulations, aimed at interpreting the experiments in chapter 4, were exploited not only to probe the laser-plasma coupling in this still unexplored regime but also to support our theoretical description, analogously to section 5.2.

5.3.1 Theoretical description

As a starting point for our work we assume that electrons which drive enhanced TNSA in MLTs experiments are heated by a pronderomotive driven mechanism which was also observed in other numerical and theoretical works [116, 119, 120]. In this scenario we propose a simple scaling for T_h:

$$T_h[\mathrm{MeV}] = C_3 \cdot T_{pond} + C_4 = C_3 \cdot 0.511 \cdot \left(\sqrt{1 + a_0^2/2} - 1\right) + C_4, \quad (5.7)$$

where the two C_3 and C_4 coefficients depend in principle on both laser and target properties. Indeed, it must be stressed that experimental parameters surely affect electron heating in a near-critical and possibly nanostructured plasma, and their actual impact is still almost completely unexplored. Nonetheless, in this first approach to the problem we decided to limit our study to the dependence on the laser intensity alone, keeping other parameters fixed. As a result the two coefficients will be derived with an approach analogous to the one presented in section 5.2 which can be applied only under similar conditions to those simulated.

We exploit PIC simulations in order to both study laser-plasma interaction with foam attached targets and to provide the two coefficients C_3 and C_4 that are required to properly use Eq. 5.7 in the analytical model in [90, 155] used in this thesis.

5.3.2 Electron temperature analysis

We here present the results of a numerical campaign aimed at studying electron heating with MLTs. As anticipated, this first survey consists in a parametric scan over the laser intensity alone. Target composition as well as other beam parameters were chosen comparable to those of chapter 4 and were kept fixed. As described in 4.1, foams grown with PLD are characterized by a complex structure: nanoparticles ($\sim$ 10-40nm) form micrometric aggregates as reported in [165]. These materials exhibit an average density of few mg/cm^3, hundreds of times lower that pyrolitic graphite ($\sim$ 2 g/cm^3). Since nanoparticles are at the solid density, most of the foam volume is empty and the filling factor (the fraction of the total foam volume occupied by actual material) is as low as $\sim$ 3-5$\cdot 10^{-3}$.
The first issue to be addressed is indeed how to properly model the foam layer. In most of literature works low density plasmas are simulated with a uniform density layer, thus neglecting their nanostructure. This strategy is reliable to describe experiments with gas jets [170, 182] or possibly with low density materials formed by arrays of nanotubes, much smaller than the laser wavelength [73]. A homogeneous plasma can also be considered a good approximation if the pre-pulse is intense enough to ionize the material and blow away its nanostructure.
Coherently with section 4.2, experiments in Korea were performed in a high-contrast regime ($3 \cdot 10^{-11}$). As a consequence, the foam morphology can be assumed to be still mostly intact at the arrival of the main pulse and can actually affect the laser-plasma coupling (see [183]). As a first approach, we compared the results of numerical simulations with two different types of foam: a homogeneous plasma with $Z/A = 1/2$ (e.g. C^{6+}) at the critical density (1 n_c) and a nanostructured foam consisting in a spatially random collection of 10 nm over-dense (100 n_c) spheres, with an average density of 1 n_c in its volume. Both foams were 8μm thick, in order to match the best case scenario in experiments (see section 4.3.2).
In fig. 5.8 and 5.9 we present the electron density and the $\hat{z}$ component of the magnetic field at different temporal frames. Regardless the foam structure, the interaction with both targets is essentially identical. The laser penetrates the low density layer and is reflected back by the over-dense plasma. It must also be remarked how the electron density in both cases is rather uniform after the interaction with the laser pulse (see fig. 5.8.e and 5.9.e). Moreover, the interaction with MLTs leads to a different production of hot electrons with respect to SLTs, in terms of both spectrum and spatial distribution. Two populations can be identi-

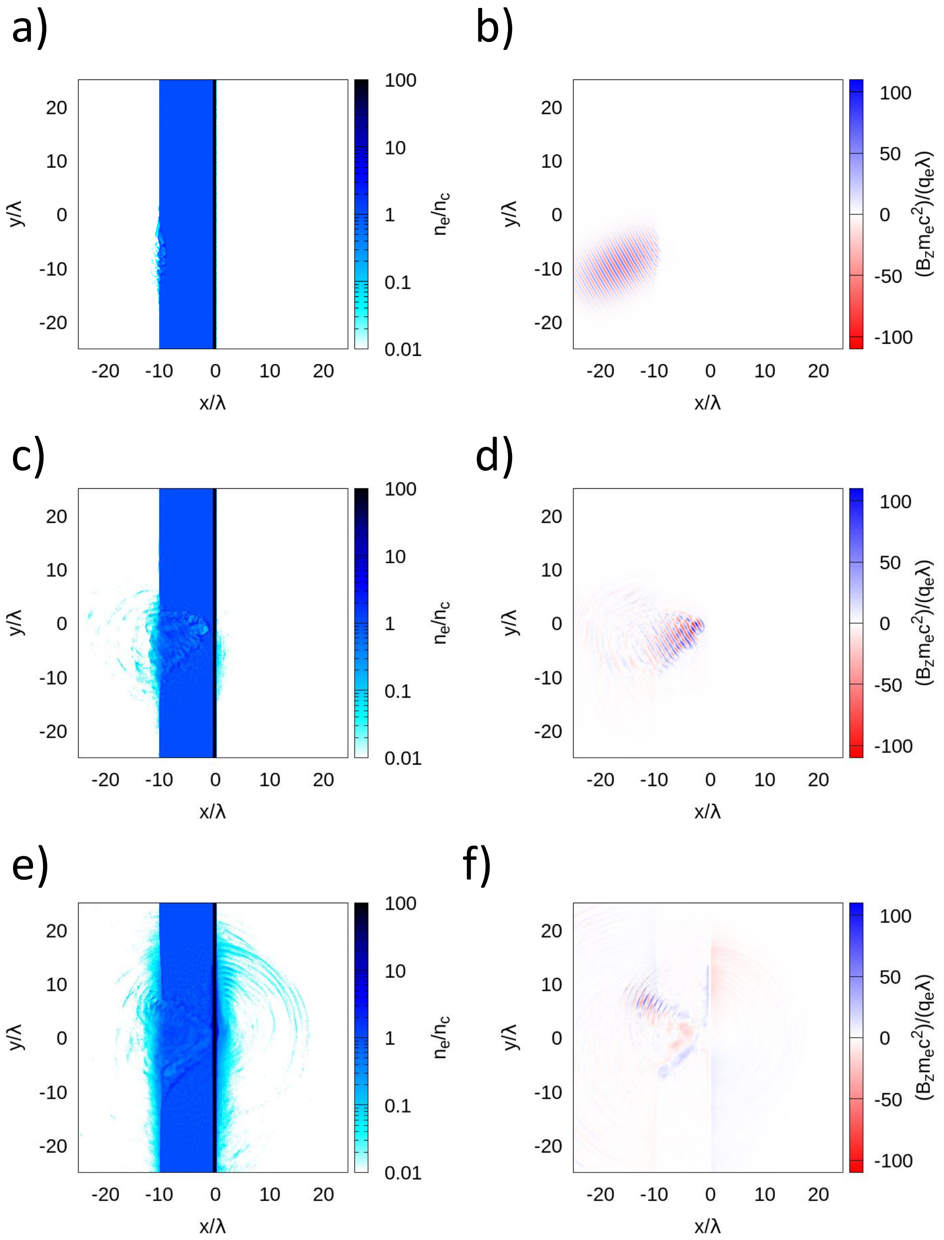

Figure 5.8: *Numerical simulations with MLT composed by the uniform foam over a 0.5 μm substrate. The electron density (a,c,e) and B_z (b,d,f) are reported at three different temporal frames: the beginning of laser interaction with the foam layer (12 fs, shown in a,b), the instant before the reflection of the beam by the solid foil (50 fs, shown in c,d) and end of laser interaction (110 fs, shown in e,f).*

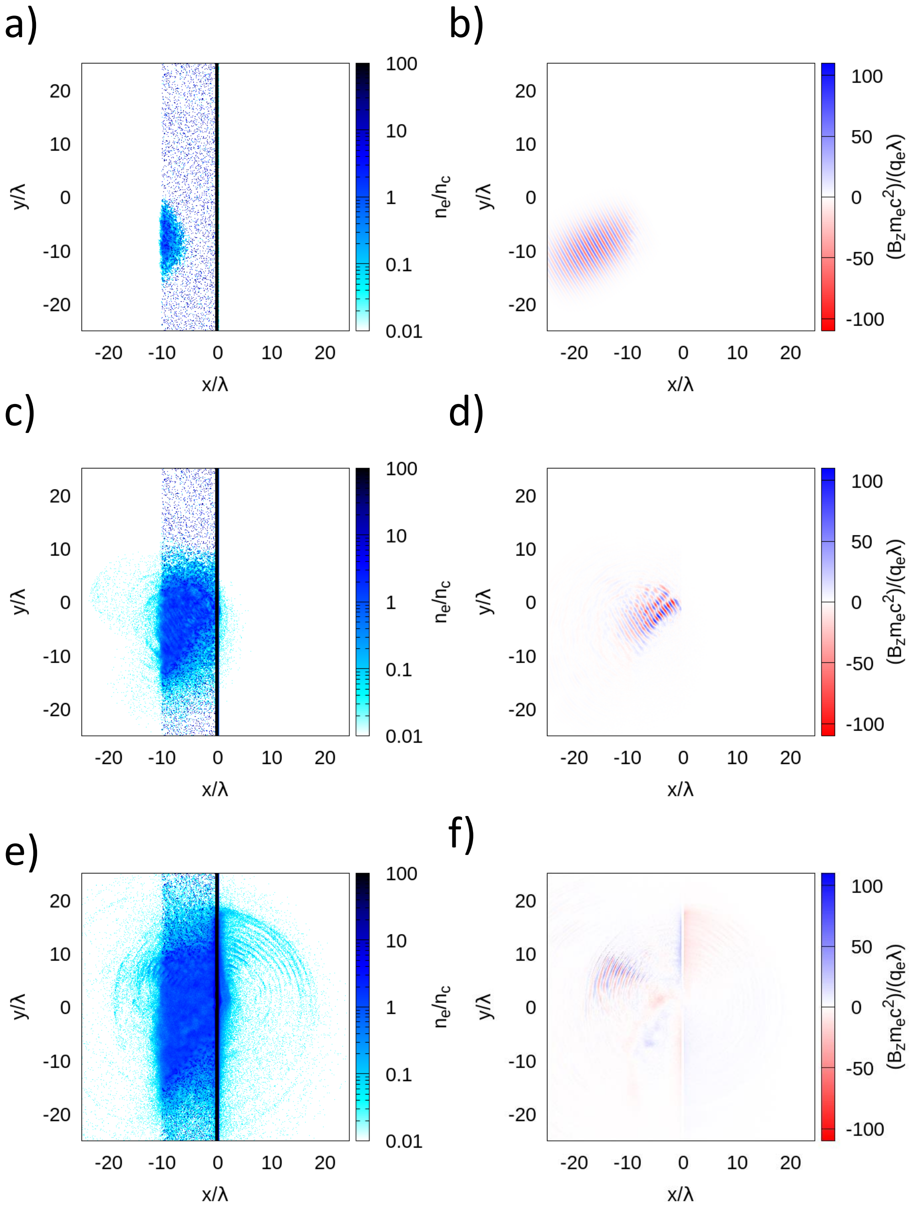

Figure 5.9: *Numerical simulations with MLT composed by the nanostructured foam over a 0.5 μm substrate. The electron density (a,c,e) and* B_z *(b,d,f) are reported at three different temporal frames: the beginning of laser interaction with the foam layer (12 fs, shown in a,b), the instant before the reflection of the beam by the solid foil (50 fs, shown in c,d) and end of laser interaction (110 fs, shown in e,f).*

fied: electrons trapped inside the target and high energy bunches that promptly escape (the emi-circular packets in fig. 5.8.e and 5.9.e).

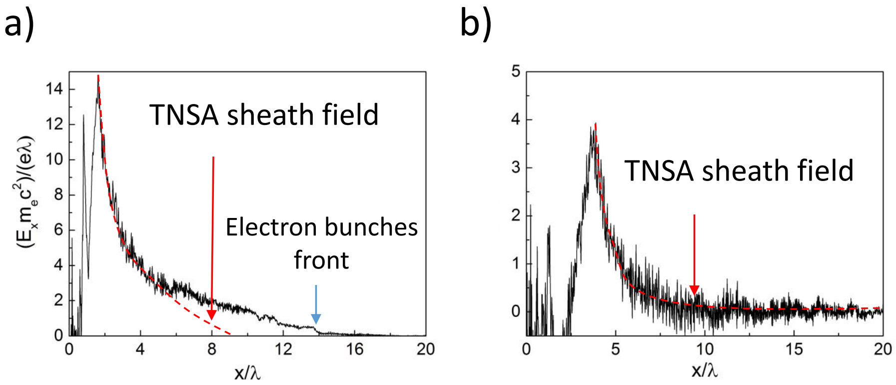

Figure 5.10: *The normal to the surface component of the electric field in the same experimental condition of 5.8 at: a) 80 fs and b) 110 fs. The dashed red lines refer to the profile of the sheath field typically observed in numerical simulations of TNSA with flat foils.*

In fig. 5.10 we show E_x during two phases of ion acceleration. Electrons trapped at the solid-vacuum interface generate the TNSA-like component of the electrostatic field which decays over few λ in the vacuum. On the other hand the escaping electrons are responsible of the “quasi constant” profile in fig. 5.10.a which quickly fades away during the ion acceleration (see 5.10.b). A simple 3D expanding capacitor model predicts that this component should vanish rapidly ($E_x \propto 1/(ct)^2$), and thus it does not contribute efficiently to the ion acceleration process.

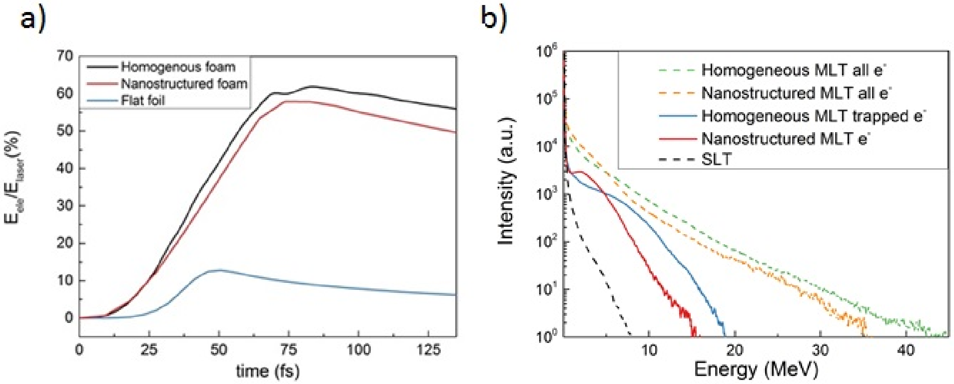

Figure 5.11: *a) Temporal evolution of E_{ele}/E_L(%) for homogeneous and nanostructured MLT (black and red, respectively) and SLT (blue). b) Electron spectra obtained under the same condition as a). The dashed lines refer to the spectra of all electrons in simulation, the straight lines to those of trapped electrons.*

In fig. 5.11.a we report the fraction of the laser beam energy absorbed by the electrons in the three target designs: MLT homogeneous/nanostructured and SLT. The presence of a near critical layer over the solid foil boosts the electron heating efficiency from $\sim 10\%$ in the SLT case to over 55% with MLTs which is also in agreement with numerical results in literature [123]. Furthermore, it must be remarked how the foam nanostructure leads to a slightly lower heating efficiency with respect to the homogeneous case. This could be due to the fact that a portion of the laser beam is lost in the Coulomb explosion of the nano-spheres. The enhanced heating efficiency achieved with MLTs naturally leads to a more energetic electron spectra, as seen in fig. 5.11.b. A clear increase of both total number and energy is observed with both types of MLT with respect to SLT. However, this enhancement effect is strongly reduced when only electrons trapped inside the target (and in a Debye length at the solid-vacuum interface) are considered. Coherently with previous considerations and with the trapped electrons model in [155], we assume that only these electrons can effectively drive TNSA.

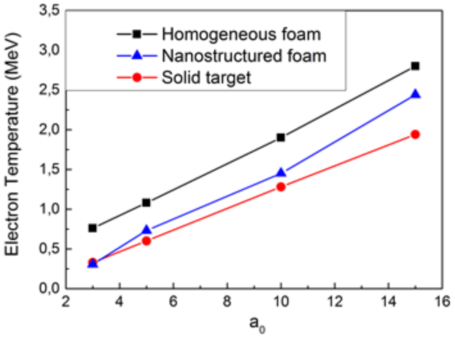

Figure 5.12: *Trapped electrons temperature at 30° incidence for homogeneous foam (black), nanostructured foam (blue), solid targets (red)*

Fig. 5.12 shows trapped electron temperatures with homogeneous foam, nanostructured foam and SLT at different laser intensities, comparable to those of section 4.2. Both MLT targets exhibit an enhanced heating with respect to SLT. We remark that the nanostructure reduces the temperature with respect to the homogeneous case which is a direct consequence of the lower coupling of the laser beam with the electronic population, as seen in fig. 5.11.a.
With an approach analogous to that of section 5.2.2, we used 5.7 to fit the intensity dependence of electron temperatures observed in simulations. We here provide the resulting C_3 and C_4 coefficients:

	homogeneous foam	**nanostructured foam**
C_3	0.48	0.48
C_4	0.42	0

Table 5.3: *2D numerical coefficients for nanostrucured and homogeneous MLT*

As anticipated at the beginning of this section, C_3 and C_4 depend in principle on a vast set of experimental parameters. For instance, the dependence of the ion cut-off energy on the foam thickness and density reported in [123] should also be observed in the electron heating and, thus, on the electron temperature. Nonetheless, our results confirm a scaling of T_h to the laser intensity $\propto \sqrt{I}$ which is compatible with a ponderomotive-like mechanism, already suggested by previous works [116, 119, 120].

5.3.3 Benchmark of theoretical estimation and experimental results

In this section we present a first attempt to extend the quasi stationary model [155] to MLT configurations. Consistently with section 5.2, this is accomplished through Eq. 5.7 with the C_3 and C_4 previously provided, comparing analytical estimations with experiments.

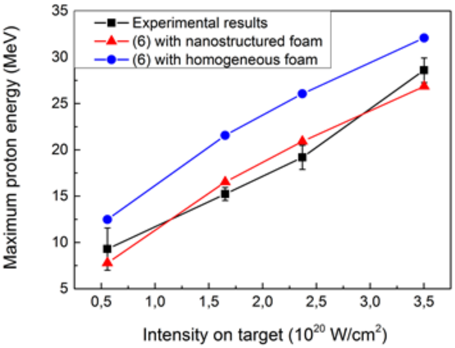

Figure 5.13: *Comparison between experimental results in section 4.3 (black) and the analytical predictions using 5.7 for homogeneous foam (blue) and nanostructured (red).*

Fig. 5.13 presents experimental results in section 4.3, obtained focusing a P polarized laser beam at 30° incidence on the best MLTs tested (l_{foam} $= 8$ μm, $n_{foam} = 1.2 n_c$ and Al 0.75 μm substrate) as well as the theoretical prediction of the quasi-stationary model combined with Eq. 5.7. It is worth to point out that, while using C_3 and C_4 for the homogeneous foam leads to an over-estimation of the ion maximum energy, a very good agreement with experimental data is found with the coefficients referring to the nanostructured case.

This is still an early result but suggests that ion acceleration with MLTs can be described through simplified TNSA analytical approaches, combined with scaling laws suitable for the different interaction regimes. The simulations also highlight the importance of the target nanostructure in the laser-plasma coupling. Further parametric analysis will be required in order to better clarify the role of laser (incidence and polarization) and target parameters (foam density, thickness) in electron heating with complex targets, with a particular focus on more realistic nanostructured foams (e.g. using diffusion limit aggregation, as in ref [183]).

6

Conclusions and future perspectives

The present PhD thesis was dedicated to a comprehensive study of Target Normal Sheath Acceleration (TNSA), not only with traditional solid targets (SLT), but also with the innovative concept of foam-attached targets (MLT). At the state of the art, TNSA is by far the most robust and observed acceleration scheme in experiments. Besides a rather simple physical interpretation, TNSA is still far from reaching an adequate degree of control and optimization, due to richness and complexity of the physics involved. The acceleration process can be divided into several sub-steps, among them, the electron heating holds a primary position since it determines the energy acquired by the plasma and, as a consequence, sets an upper limit on the ion conversion efficiency. In section 2.1.3, a concise review outlined how different experimental conditions may lead to different coupling mechanisms which result into a more or less efficient electron heating. Even though laser-plasma interaction is an active topic of research, in specific regimes it is still largely unexplored. In chapter 3 we also outlined how all theoretical descriptions include the electron temperature as a building block. The latter is one of the quantities which characterize the hot electron population which, in agreement with the TNSA scheme, drives the ion acceleration. Up to date, the largely used ponderomotive scaling law shows clear limitations, not taking into account the role of a number of parameters which are experimentally known to significantly influence the laser plasma coupling. As a natural consequence, this limitation reflects into TNSA analytical models which adopt such scaling law, that will thus neglect some relevant physical aspects. Moreover, a ponderomotive scaling also needs justifications to be applied to advanced target configurations which had recently

attracted significant interest.
The best solution to tackle all the outlined open issues is through a theoretical approach supported by experimental data and numerical simulations. As seen in chapter 4, the analysis of two recent experimental campaigns allowed to gain a deeper insight of TNSA. We list some of the main results here:

- This analysis allowed to obtain a robust experimental database of laser-ion acceleration with flat solid target (SLT), clarifying the role of laser polarization over a wide range of laser intensities. Through a large set of measurements we confirmed that laser polarization is indeed a crucial parameter to be controlled in order to achieve an efficient ion acceleration. Protons with energies up to 22 MeV were measured in P polarization while S and C polarizations reached as far as 17 and 10 MeV, respectively. Furthermore, significant differences in the total accelerated charge between the three polarizations were reported. Even thought these results were qualitatively expected, this dedicated study greatly improved the quantitative knowledge of this laser feature in TNSA.

- The comparison between experiments with both SLTs and novel MLTs (described in section 4.1) supported our claim of TNSA, enhanced by a more efficient laser absorption in the foam layer. Indeed, the accelerated ion spectra with MLT reproduces all TNSA features, with a remarkable improvement with respect to traditional targets under suitable experimental conditions.

- The analysis of TNSA with different MLT configurations demonstrated a significant dependence of the properties of the ion beam to the foam thickness which was predicted by a previous numerical campaign [123]. Cut-off energies above 30 MeVs were reported with the best MLT tested (8 μm, $\sim n_c$ foam), to be compared to the 22 MeV with SLTs in P pol.

- We did not report any significant sensitivity to the laser polarization of the cut-off energy and total accelerated charge with MLTs. This could be a direct consequence of the deeply different interaction mechanism with respect to SLTs.

- A minor decrease of the cut-off energy in MLTs with thick substrates (up to 12 μm), to be compared to the strong thickness dependence of TNSA with SLTs, also reported in many literature works. Thicker substrates could be appealing for their higher mechanical robustness which is suitable for applications requiring high repetition rates.

Besides the intrinsic interest in the above presented results, the experimental analysis was exploited in this work to support the theoretical activity described in chapter 5. In particular, in this PhD we focused our attention on the study of laser induced electron heating. A better understanding of this process could be of great importance in scenarios where an efficient laser-plasma coupling is required. In the specific case of this work, the study was aimed at laser interaction with both SLTs and MLTs. As far as SLTs are of concern, we combined Brunel effect and $\mathbf{j}\times\mathbf{B}$ heating. We thus provided a simple scaling law that overcomes some limitations of the ponderomotive scaling. Our claim of a combined heating is supported by an extensive 3D and 2D numerical campaign. Simulations suggest also that ponderomotive scaling may strongly overestimate the electron temperature which is in line with recent works [166–168]. In order to test our scaling law, we combined it with the quasi-stationary TNSA model presented in section 3.1.2. The comparison with the experimental results shows a better agreement with respect to predictions relying on the ponderomotive scaling.

In this work we also approached laser interaction with MLTs. Furthermore, as a first attempt to address the possible influence of the foam morphology, we compared two different configurations of MTLs: an homogeneous foam and a nanostructured one, respectively. In both cases, the strongly enhanced electron heating efficiency, with respect to SLTs, naturally led to a higher electron temperature. A strong indication from simulations is that only electrons trapped in the target and in a Debye length at the vacuum-target interface significantly contribute to the ion acceleration. Moreover, the preliminary test of two foam morphologies suggests that the target nanostructure can play a significant role in electron heating. Furthermore, we remark how numerical results were coherent with a ponderomotive-like scaling to the laser intensity, enhanced by the presence of the foam layer, also suggested in previous literature works. Finally, the good agreement between model predictions and experimental results is a first but promising step towards the study of laser absorption with MLT.

6.1 Future perspectives

This discussion naturally leads to some appealing perspective of the present work. The two experimental campaigns disclosed new opportunities for future research. More target designs as well as laser parameters can be addressed in forthcoming studies. Following the footsteps of the 2015 campaign, experiments with thinner and more uniform foams ($\leq 8\ \mu$m) will be performed. Moreover, different combinations of foam densities and thicknesses could provide a more efficient acceleration at given laser conditions and must be therefore investigated. A further exploration of the effect of laser parameters on TNSA with MLT is also of great interest. The linear dependence of the cut-off energy observed could be confirmed in experiments at higher intensity. Moreover, they are required to sustain the proposal of the MLT concept over SLTs in a more ample interaction regime.

The influence of the laser energy on laser induced ion acceleration is still object of discussion, even in the SLT case, and demands a dedicated study. Furthermore, the few experimental measurements at different pulse durations (and chirp) in section 4.3.5 provided non-trivial results. Nonetheless a further investigation could be appealing in order to outline a new and possibly efficient strategy for ion acceleration. As a final remark, TNSA experiments with SLTs are usually performed with high contrast lasers, in order to prevent the pre-pulses from damaging the target. In most of works, plasma mirrors are exploited to suppress this undesired component of the beam, at the price of losing up to 50% of its energy. On the other hand, MLTs should be able, in principle, to perform well even at low contrast. In this scenario, the foam layer should absorb the pre-pulse, preventing damages on the substrate. This is particularly interesting since it allows to avoid the significant laser energy loss caused by the plasma mirrors.

Experiments, aimed at clarifying the above mentioned open points, are already planned in collaboration with Helmholtz-Zentrum Dresden-Rossendorf (HZDR, Germany).

As far as the numerical work is considered, a more extensive scan, also exploiting realistic 3D geometries, could support and guide the suggested experimental investigations. New target designs can be easily tested over a wide range of laser features. It must be however remarked how some specific scenarios require a particular care. As an example, the long time scales of pre-pulses (from ps to few ns) can not be reproduced with PIC simulations due to the immense amount of CPU hours that would be re-

quired. A possible solution could be obtained using hydrodynamical codes to reproduce the plasma expansion due to the interaction with the prepulse and then use the expanded plasma configuration as input for the PIC simulation of the interaction with the main beam.
Numerical simulations can be also aimed at a deeper study of the electron heating. It must be also included a proper investigation of the influence of the foam morphology in the production of hot electrons with MLTs. As suggested in this work, it could be of great relevance and at the sate of the art is still poorly surveyed. Indeed, more realistic foam designs (as seen in [183])could provide a more accurate insight of laser coupling with MLTs and a deeper knowledge of this complex interaction regime.
The numerical analysis can also inspire the development of more theoretically robust models, required to better disclose the dominant physical mechanisms. Scaling laws for the electron temperature, predictive in a more ample range of experimental conditions, are particularly requested in the case of MLTs. As seen in this PhD, these are also essential to extend analytical description of TNSA with advanced targets which can interpret, predict and also guide future research.
We finally suggest a possible parallel applications of MLTs. Indeed, these could also be exploited as a source of short (tens of fs) electron bursts. Indeed, in the numerical part of this PhD we suggested how the highly energetic bunches of escaping electrons do not contribute to ion acceleration. If the targets are properly designed to enhance this emission instead of focusing on ion acceleration, these electrons could be exploited in applications such as ultra-fast electron imaging.

List of Figures

List of Tables

Bibliography

[1] Albert Einstein. Zur quantentheorie der strahlung. *Physikalische Zeitschrift*, 18, 1917.

[2] Theodore H Maiman. Stimulated optical radiation in ruby. 1960.

[3] FJ McClung and RW Hellwarth. Giant optical pulsations from ruby. *Journal of Applied Physics*, 33(3):828–829, 1962.

[4] LE Hargrove, Richard L Fork, and MA Pollack. Locking of he–ne laser modes induced by synchronous intracavity modulation. *Applied Physics Letters*, 5(1):4–5, 1964.

[5] Arlee V Smith, Binh T Do, G Ronald Hadley, and Roger L Farrow. Optical damage limits to pulse energy from fibers. *IEEE Journal of selected topics in quantum electronics*, 15(1):153–158, 2009.

[6] Donna Strickland and Gerard Mourou. Compression of amplified chirped optical pulses. *Optics communications*, 56(3):219–221, 1985.

[7] Rajeev Khare and Paritosh K Shukla. *Temporal stretching of laser pulses*. INTECH Open Access Publisher, 2010.

[8] Cédric Thaury, F Quéré, J-P Geindre, et al. Plasma mirrors for ultrahigh-intensity optics. *Nature Physics*, 3(6):424–429, 2007.

[9] Colin Danson, David Hillier, Nicholas Hopps, and David Neely. Petawatt class lasers worldwide. *High Power Laser Science and Engineering*, 3:e3, 2015.

[10] P. F. Moulton. Spectroscopic and laser characteristics of ti:al2o3. *J. Opt. Soc. Am. B*, 3(1):125–133, Jan 1986.

[11] C Kumar N Patel. Continuous-wave laser action on vibrational-rotational transitions of c o 2. *Physical review*, 136(5A):A1187, 1964.

[12] JE Geusic, HM Marcos, and LeGrand Van Uitert. Laser oscillations in nd-doped yttrium aluminum, yttrium gallium and gadolinium garnets. *Applied Physics Letters*, 4(10):182–184, 1964.

[13] Jae Hee Sung, Seong Ku Lee, Tae Jun Yu, Tae Moon Jeong, and Jongmin Lee. 0.1 hz 1.0 pw ti:sapphire laser. *Opt. Lett.*, 35(18):3021–3023, Sep 2010.

[14] Erhard W Gaul, Mikael Martinez, Joel Blakeney, et al. Demonstration of a 1.1 petawatt laser based on a hybrid optical parametric chirped pulse amplification/mixed nd: glass amplifier. *Applied optics*, 49(9):1676–1681, 2010.

[15] Igor V. Pogorelsky, Markus Babzien, Ilan Ben-Zvi, John Skaritka, and Mikhail N. Polyanskiy. {BESTIA} âĂŞ the next generation ultra-fast {CO2} laser for advanced accelerator research. *Nuclear Instruments and Methods in Physics Research Section A: Accelerators, Spectrometers, Detectors and Associated Equipment*, 829:432 – 437, 2016. 2nd European Advanced Accelerator Concepts Workshop - {EAAC} 2015.

[16] V. Yanovsky, V. Chvykov, G. Kalinchenko, et al. Ultra-high intensity- 300-tw laser at 0.1 hz repetition rate. *Opt. Express*, 16(3):2109–2114, Feb 2008.

[17] Jae Hee Sung, Seong Ku Lee, Hwang Woon Lee, Je Yoon Yoo, and Chang Hee Nam. Development of 0.1 hz 4.0 pw laser at corels. In *Conference on Lasers and Electro-Optics*, page SM1M.3. Optical Society of America, 2016.

[18] C Hernandez-Gomez, S P Blake, O Chekhlov, et al. The vulcan 10 pw project. *Journal of Physics: Conference Series*, 244(3):032006, 2010.

[19] Ian N Ross, John L Collier, Pavel Matousek, et al. Generation of terawatt pulses by use of optical parametric chirped pulse amplification. *Applied Optics*, 39(15):2422–2427, 2000.

[20] Xiaodong Yang, Zhi zhan Xu, Yu xin Leng, et al. Multiterawatt laser system based on optical parametric chirped pulse amplification. *Opt. Lett.*, 27(13):1135–1137, Jul 2002.

[21] L.J. Waxer, D.N. Maywar, J.H. Kelly, et al. High-energy petawatt capability for the omega laser. *Opt. Photon. News*, 16(7):30–36, Jul 2005.

[22] V.V. Lozhkarev, G.I. Freidman, V.N. Ginzburg, et al. 200 tw 45 fs laser based on optical parametric chirped pulse amplification. *Opt. Express*, 14(1):446–454, Jan 2006.

[23] B Rus, P Bakule, D Kramer, et al. Eli-beamlines: development of next generation short-pulse laser systems. In *SPIE Optics+ Optoelectronics*, pages 95150F–95150F. International Society for Optics and Photonics, 2015.

[24] JP Zou, C Le Blanc, DN Papadopoulos, et al. Design and current progress of the apollon 10 pw project. *High Power Laser Science and Engineering*, 3:e2, 2015.

[25] Dimitrios Papadopoulos, Catherine Le Blanc, Gilles Chériaux, et al. The apollon-10p project: Design and current status. In *Advanced Solid State Lasers*, pages ATu3A–43. Optical Society of America, 2013.

[26] Paul Gibbon. *Short pulse laser interactions with matter.* Imperial College Press, 2005.

[27] Peter Mulser and Dieter Bauer. *High power laser-matter interaction*, volume 238. Springer Science & Business Media, 2010.

[28] William L Kruer. *The physics of laser plasma interactions.* Reading, MA (US); Addison-Wesley Publishing Co., 1988.

[29] D Bauer, P Mulser, and W-H Steeb. Relativistic ponderomotive force, uphill acceleration, and transition to chaos. *Physical review letters*, 75(25):4622, 1995.

[30] H Barry Bebb and Albert Gold. Multiphoton ionization of hydrogen and rare-gas atoms. *Physical Review*, 143(1):1, 1966.

[31] LV Keldysh. Ionization in the field of a strong electromagnetic wave. *Zh. Eksperim. i Teor. Fiz.*, 47, 1964.

[32] SM Vinko, O Ciricosta, TR Preston, et al. Investigation of femtosecond collisional ionization rates in a solid-density aluminium plasma. *Nature communications*, 6, 2015.

[33] G.B. et al. Lee, Y.T.; Zimmerman. Ionization in the field of a strong electromagnetic wave. *3rd international conference and workshop on radiative properties of hot dense matter*, 1986.

[34] T. Tajima and J. M. Dawson. Laser electron accelerator. *Phys. Rev. Lett.*, 43:267–270, Jul 1979.

[35] Alexancer Pukhov and Jürgen Meyer-ter Vehn. Laser wake field acceleration: the highly non-linear broken-wave regime. *Applied Physics B*, 74(4-5):355–361, 2002.

[36] Allen Caldwell, Konstantin Lotov, Alexander Pukhov, and Frank Simon. Proton-driven plasma-wakefield acceleration. *Nature Physics*, 5(5):363–367, 2009.

[37] Y. Kitagawa, T. Matsumoto, T. Minamihata, et al. Beat-wave excitation of plasma wave and observation of accelerated electrons. *Phys. Rev. Lett.*, 68:48–51, Jan 1992.

[38] Thomas Katsouleas. Accelerator physics: Electrons hang ten on laser wake. *Nature*, 431(7008):515–516, 2004.

[39] WP Leemans, B Nagler, AJ Gonsalves, et al. Gev electron beams from a centimetre-scale accelerator. *Nature physics*, 2(10):696–699, 2006.

[40] WP Leemans, AJ Gonsalves, H-S Mao, et al. Multi-gev electron beams from capillary-discharge-guided subpetawatt laser pulses in the self-trapping regime. *Physical review letters*, 113(24):245002, 2014.

[41] Hyung Taek Kim, Ki Hong Pae, Hyuk Jin Cha, et al. Enhancement of electron energy to the multi-gev regime by a dual-stage laser-wakefield accelerator pumped by petawatt laser pulses. *Phys. Rev. Lett.*, 111:165002, Oct 2013.

[42] R Assmann, R Bingham, T Bohl, et al. Proton-driven plasma wakefield acceleration: a path to the future of high-energy particle physics. *Plasma Physics and Controlled Fusion*, 56(8):084013, 2014.

[43] SV Bulanov, NM Naumova, VA Vshivkov, et al. Interaction of petawatt laser pulses with underdense plasmas. *Plasma Physics Reports*, 25(9):701–714, 1999.

[44] F Yan, ZM Sheng, QL Dong, J Zhang, and W Yu. Ion acceleration in laser-excited plasma wake fields. *JOSA B*, 23(6):1190–1195, 2006.

[45] Antoine Rousse, Kim Ta Phuoc, Rahul Shah, et al. Production of a kev x-ray beam from synchrotron radiation in relativistic laser-plasma interaction. *Phys. Rev. Lett.*, 93:135005, 2004.

[46] H-P Schlenvoigt, K Haupt, A Debus, et al. A compact synchrotron radiation source driven by a laser-plasma wakefield accelerator. *Nature Physics*, 4(2):130–133, 2008.

[47] WP Leemans, D Rodgers, PE Catravas, et al. Gamma-neutron activation experiments using laser wakefield accelerators. *Physics of Plasmas*, 8(5):2510–2516, 2001.

[48] SA Reed, V Chvykov, G Kalintchenko, et al. Efficient initiation of photonuclear reactions using quasimonoenergetic electron beams from laser wakefield acceleration. *Journal of Applied Physics*, 102(7):073103, 2007.

[49] E Falize, S Bouquet, and C Michaut. Scaling laws for radiating fluids: the pillar of laboratory astrophysics. *Astrophysics and Space Science*, 322(1-4):107–111, 2009.

[50] P. T. Springer, D. J. Fields, B. G. Wilson, et al. Spectroscopic absorption measurements of an iron plasma. *Phys. Rev. Lett.*, 69:3735–3738, 1992.

[51] F. Fiuza, A. Stockem, E. Boella, et al. Laser-driven shock acceleration of monoenergetic ion beams. *Phys. Rev. Lett.*, 109:215001, 2012.

[52] A Stockem, F Fiuza, A Bret, RA Fonseca, and LO Silva. Exploring the nature of collisionless shocks under laboratory conditions. *Scientific reports*, 4, 2014.

[53] P. M. Nilson, L. Willingale, M. C. Kaluza, et al. Magnetic reconnection and plasma dynamics in two-beam laser-solid interactions. *Phys. Rev. Lett.*, 97:255001, 2006.

[54] SG Glendinning, SV Weber, P Bell, et al. Laser-driven planar rayleigh-taylor instability experiments. *Physical review letters*, 69(8):1201, 1992.

[55] George D Tsakiris, Klaus Eidmann, Jürgen Meyer-ter Vehn, and Ferenc Krausz. Route to intense single attosecond pulses. *New Journal of Physics*, 8(1):19, 2006.

[56] Roland Lichters, J Meyer-ter Vehn, and A Pukhov. Short-pulse laser harmonics from oscillating plasma surfaces driven at relativistic intensity. *Physics of Plasmas (1994-present)*, 3(9):3425–3437, 1996.

[57] Matt Zepf, B Dromey, S Kar, et al. High harmonics from relativistically oscillating plasma surfacesâĂŤa high brightness attosecond source at kev photon energies. *Plasma Physics and Controlled Fusion*, 49(12B):B149, 2007.

[58] Andrea Macchi, Marco Borghesi, and Matteo Passoni. Ion acceleration by superintense laser-plasma interaction. *Rev. Mod. Phys.*, 85:751–793, 2013.

[59] Hiroyuki Daido, Mamiko Nishiuchi, and Alexander S Pirozhkov. Review of laser-driven ion sources and their applications. *Reports on Progress in Physics*, 75(5):056401, 2012.

[60] SV Bulanov, T Zh Esirkepov, VS Khoroshkov, AV Kuznetsov, and F Pegoraro. Oncological hadrontherapy with laser ion accelerators. *Physics Letters A*, 299(2):240–247, 2002.

[61] Ernesto Amato, Antonio Italiano, Daniele Margarone, et al. Study of the production yields of 18 f, 11 c, 13 n and 15 o positron emitters from plasma-laser proton sources at eli-beamlines for labeling of pet radiopharmaceuticals. *Nuclear Instruments and Methods in Physics Research Section A: Accelerators, Spectrometers, Detectors and Associated Equipment*, 811:1–5, 2016.

[62] DP Higginson, L Vassura, MM Gugiu, et al. Temporal narrowing of neutrons produced by high-intensity short-pulse lasers. *Physical review letters*, 115(5):054802, 2015.

[63] S Kar, A Green, H Ahmed, et al. Beamed neutron emission driven by laser accelerated light ions. *New Journal of Physics*, 18(5):053002, 2016.

[64] JC Fernández, BJ Albright, FN Beg, et al. Fast ignition with laser-driven proton and ion beams. *Nuclear Fusion*, 54(5):054006, 2014.

[65] CK Li, FH Séguin, JA Frenje, et al. Measuring e and b fields in laser-produced plasmas with monoenergetic proton radiography. *Physical review letters*, 97(13):135003, 2006.

[66] RA Snavely, MH Key, SP Hatchett, et al. Intense high-energy proton beams from petawatt-laser irradiation of solids. *Physical Review Letters*, 85(14):2945, 2000.

[67] A. Maksimchuk, S. Gu, K. Flippo, D. Umstadter, and V. Yu. Bychenkov. Forward ion acceleration in thin films driven by a high-intensity laser. *Phys. Rev. Lett.*, 84:4108–4111, 2000.

[68] E. L. Clark, K. Krushelnick, J. R. Davies, et al. Measurements of energetic proton transport through magnetized plasma from intense laser interactions with solids. *Phys. Rev. Lett.*, 84:670–673, 2000.

[69] Andrea Favalli, Nevzat Guler, Daniela Henzlova, et al. Experimental observation of β-delayed neutrons from ^{9} li as a way to study short-pulse laser-driven deuteron production. *arXiv preprint arXiv:1605.05702*, 2016.

[70] Satyabrata Kar, Hamad Ahmed, Rajendra Prasad, et al. Guided post-acceleration of laser-driven ions by a miniature modular structure. *Nature communications*, 7, 2016.

[71] F. Wagner, O. Deppert, C. Brabetz, et al. Maximum proton energy above 85 mev from the relativistic interaction of laser pulses with micrometer thick ch_2 targets. *Phys. Rev. Lett.*, 116:205002, 2016.

[72] APL Robinson, M Zepf, S Kar, RG Evans, and C Bellei. Radiation pressure acceleration of thin foils with circularly polarized laser pulses. *New journal of Physics*, 10(1):013021, 2008.

[73] J. H. Bin, W. J. Ma, H. Y. Wang, et al. Ion acceleration using relativistic pulse shaping in near-critical-density plasmas. *Phys. Rev. Lett.*, 115:064801, 2015.

[74] KL Lancaster, S Karsch, H Habara, et al. Characterization of 7li (p, n) 7be neutron yields from laser produced ion beams for fast neutron radiography. *Physics of plasmas*, 11(7):3404–3408, 2004.

[75] LJ Perkins, BG Logan, MD Rosen, et al. The investigation of high intensity laser driven micro neutron sources for fusion materials research at high fluence. *Nuclear Fusion*, 40(1):1, 2000.

[76] SC Wilks, AB Langdon, TE Cowan, et al. Energetic proton generation in ultra-intense laser–solid interactions. *Physics of Plasmas (1994-present)*, 8(2):542–549, 2001.

[77] EL Clark, K Krushelnick, M Zepf, et al. Energetic heavy-ion and proton generation from ultraintense laser-plasma interactions with solids. *Physical Review Letters*, 85(8):1654, 2000.

[78] Matthew Zepf, EL Clark, K Krushelnick, et al. Fast particle generation and energy transport in laser-solid interactions. *Physics of Plasmas*, 8:2323–2330, 2001.

[79] P McKenna, KWD Ledingham, JM Yang, et al. Characterization of proton and heavier ion acceleration in ultrahigh-intensity laser interactions with heated target foils. *Physical Review E*, 70(3):036405, 2004.

[80] I Spencer, KWD Ledingham, P McKenna, et al. Experimental study of proton emission from 60-fs, 200-mj high-repetition-rate tabletop-laser pulses interacting with solid targets. *Physical Review E*, 67(4):046402, 2003.

[81] M Borghesi, AJ Mackinnon, DH Campbell, et al. Multi-mev proton source investigations in ultraintense laser-foil interactions. *Physical Review Letters*, 92(5):055003, 2004.

[82] Matthew Allen, Pravesh K Patel, Andrew Mackinnon, et al. Direct experimental evidence of back-surface ion acceleration from laser-irradiated gold foils. *Physical review letters*, 93(26):265004, 2004.

[83] M Borghesi, A Bigongiari, S Kar, et al. Laser-driven proton acceleration: source optimization and radiographic applications. *Plasma Physics and Controlled Fusion*, 50(12):124040, 2008.

[84] K Krushelnick, EL Clark, FN Beg, et al. High intensity laser-plasma sources of ionsâĂŤphysics and future applications. *Plasma physics and controlled fusion*, 47(12B):B451, 2005.

[85] M Coury, DC Carroll, APL Robinson, et al. Influence of laser irradiated spot size on energetic electron injection and proton acceleration in foil targets. *Applied Physics Letters*, 100(7):074105, 2012.

[86] A Fukumi, M Nishiuchi, H Daido, et al. Laser polarization dependence of proton emission from a thin foil target irradiated by a 70 fs, intense laser pulse. *Physics of plasmas*, 12(10):0701, 2005.

[87] T Ceccotti, A Lévy, F Réau, et al. Tnsa in the ultra-high contrast regime. *Plasma Physics and Controlled Fusion*, 50(12):124006, 2008.

[88] A Sgattoni, T Ceccotti, V Floquet, et al. Laser plasma proton acceleration experiments using foam-covered and grating targets. In *SPIE Optics+ Optoelectronics*, pages 87790L–87790L. International Society for Optics and Photonics, 2013.

[89] K Zeil, SD Kraft, S Bock, et al. The scaling of proton energies in ultrashort pulse laser plasma acceleration. *New Journal of Physics*, 12(4):045015, 2010.

[90] M Passoni, C Perego, A Sgattoni, and D Batani. Advances in target normal sheath acceleration theory. *Physics of Plasmas (1994-present)*, 20(6):060701, 2013.

[91] JH Bin, AL Lei, LH Cao, et al. Influence of the target front-surface curvature on proton acceleration in laser-foil interaction. *Physics of Plasmas (1994-present)*, 16(4):043109, 2009.

[92] Z Lecz, O Boine-Frankenheim, and V Kornilov. Target normal sheath acceleration for arbitrary proton layer thickness. *Nuclear Instruments and Methods in Physics Research Section A: Accelerators, Spectrometers, Detectors and Associated Equipment*, 727:51–58, 2013.

[93] Florian Wagner, Stefan Bedacht, Alex Ortner, et al. Pre-plasma formation in experiments using petawatt lasers. *Optics express*, 22(24):29505–29514, 2014.

[94] Rachel Nuter, Laurent Gremillet, P Combis, et al. Influence of a preplasma on electron heating and proton acceleration in ultraintense laser-foil interaction. *Journal of Applied Physics*, 104(10):103307, 2008.

[95] Issie Peter Shkarofsky, Tudor Wyatt Johnston, and Morrel Paul Bachynski. *The particle kinetics of plasmas.* Reading, Mass.: Addison-Wesley Publishing Company, 1966.

[96] William L Kruer. The physics of laser plasma interactions. 1988.

[97] DW Forslund, JM Kindel, Kenneth Lee, EL Lindman, and RL Morse. Theory and simulation of resonant absorption in a hot plasma. *Physical Review A*, 11(2):679, 1975.

[98] Kent Estabrook and William L Kruer. Properties of resonantly heated electron distributions. *Physical Review Letters*, 40(1):42, 1978.

[99] DW Forslund, JM Kindel, and K Lee. Theory of hot-electron spectra at high laser intensity. *Physical Review Letters*, 39(5):284, 1977.

[100] DW Forslund, JM Kindel, and K Lee. Theory of hot-electron spectra at high laser intensity. *Physical Review Letters*, 39(5):284, 1977.

[101] F Brunel. Not-so-resonant, resonant absorption. *Physical Review Letters*, 59(1):52, 1987.

[102] P Mulser, SM Weng, and Tatyana Liseykina. Analysis of the brunel model and resulting hot electron spectra. *Physics of Plasmas (1994-present)*, 19(4):043301, 2012.

[103] Tatyana Liseykina, P Mulser, and M Murakami. Collisionless absorption, hot electron generation, and energy scaling in intense laser-target interaction. *Physics of Plasmas (1994-present)*, 22(3):033302, 2015.

[104] Paul Gibbon, AA Andreev, and K Yu Platonov. A kinematic model of relativistic laser absorption in an overdense plasma. *Plasma Physics and Controlled Fusion*, 54(4):045001, 2012.

[105] Scott C Wilks and William L Kruer. Absorption of ultrashort, ultra-intense laser light by solids and overdense plasmas. *IEEE Journal of Quantum Electronics*, 33(11):1954–1968, 1997.

[106] Cai Hongbo, Yu Wei, Zhu Shaoping, and Zheng Chunyang. Short-pulse laser absorption via jxb heating in ultrahigh intensity laser plasma interaction. *Physics of plasmas*, 13(11), 2006.

[107] R Gr Chambers. Anomalous skin effect in metals. 1950.

[108] PJ Catto and Richard M More. Sheath inverse bremsstrahlung in laser produced plasmas. *Physics of Fluids*, 20:704, 1977.

[109] XL Chen and RN Sudan. Necessary and sufficient conditions for self-focusing of short ultraintense laser pulse in underdense plasma. *Physical review letters*, 70(14):2082, 1993.

[110] MD Feit, AM Komashko, and AM Rubenchik. Relativistic self-focusing in underdense plasma. *Physica D: Nonlinear Phenomena*, 152:705–713, 2001.

[111] P Sprangle, Cha-Mei Tang, and E Esarey. Relativistic self-focusing of short-pulse radiation beams in plasmas. *IEEE transactions on plasma science*, 15(2):145–153, 1987.

[112] Niti Kant, Sudhir Saralch, and Harjit Singh. Ponderomotive self-focusing of a short laser pulse under a plasma density ramp. *Nukleonika*, 56:149–153, 2011.

[113] P Monot, T Auguste, P Gibbon, et al. Experimental demonstration of relativistic self-channeling of a multiterawatt laser pulse in an underdense plasma. *Physical review letters*, 74(15):2953, 1995.

[114] Andrea Macchi, Alessandra Bigongiari, Francesco Ceccherini, et al. Ion dynamics and coherent structure formation following laser pulse self-channeling. *Plasma Physics and Controlled Fusion*, 49(12B):B71, 2007.

[115] L Willingale, PM Nilson, AGR Thomas, et al. High-power, kilojoule laser interactions with near-critical density plasmaa). *Physics of Plasmas (1994-present)*, 18(5):056706, 2011.

[116] APL Robinson, RMGM Trines, J Polz, and M Kaluza. Absorption of circularly polarized laser pulses in near-critical plasmas. *Plasma Physics and Controlled Fusion*, 53(6):065019, 2011.

[117] CD Decker, WB Mori, K-C Tzeng, and T Katsouleas. The evolution of ultra-intense, short-pulse lasers in underdense plasmas. *Physics of Plasmas (1994-present)*, 3(5):2047–2056, 1996.

[118] SV Bulanov, IN Inovenkov, VI Kirsanov, NM Naumova, and AS Sakharov. Nonlinear depletion of ultrashort and relativistically strong laser pulses in an underdense plasma. *Physics of Fluids B: Plasma Physics (1989-1993)*, 4(7):1935–1942, 1992.

[119] Andrea Macchi, Francesco Ceccherini, Fulvio Cornolti, Satyabrata Kar, and Marco Borghesi. Electric field dynamics and ion acceleration in the self-channeling of a superintense laser pulse. *Plasma Physics and Controlled Fusion*, 51(2):024005, 2009.

[120] WB Mori, C Joshi, JM Dawson, DW Forslund, and JM Kindel. Evolution of self-focusing of intense electromagnetic waves in plasma. *Physical review letters*, 60(13):1298, 1988.

[121] SC Wilks, WL Kruer, M Tabak, and AB Langdon. Absorption of ultra-intense laser pulses. *Physical review letters*, 69(9):1383, 1992.

[122] F Sylla, Alessandro Flacco, S Kahaly, et al. Short intense laser pulse collapse in near-critical plasma. *Physical review letters*, 110(8):085001, 2013.

[123] Andrea Sgattoni, Pasquale Londrillo, Andrea Macchi, and Matteo Passoni. Laser ion acceleration using a solid target coupled with a low-density layer. *Physical Review E*, 85(3):036405, 2012.

[124] Matthew C Levy, Scott C Wilks, Max Tabak, Stephen B Libby, and Matthew G Baring. Petawatt laser absorption bounded. *Nature communications*, 5, 2014.

[125] JM Pitarke, VM Silkin, EV Chulkov, and PM Echenique. Theory of surface plasmons and surface-plasmon polaritons. *Reports on progress in physics*, 70(1):1, 2006.

[126] T Ceccotti, V Floquet, A Sgattoni, et al. Evidence of resonant surface-wave excitation in the relativistic regime through measurements of proton acceleration from grating targets. *Physical review letters*, 111(18):185001, 2013.

[127] V Floquet, O Klimo, J Psikal, et al. Micro-sphere layered targets efficiency in laser driven proton acceleration. *Journal of Applied Physics*, 114(8):083305, 2013.

[128] D Margarone, O Klimo, IJ Kim, et al. Enhanced tnsa acceleration with 0.1-1 pw lasers. In *SPIE Optics+ Optoelectronics*, pages 878023–878023. International Society for Optics and Photonics, 2013.

[129] SA Gaillard, T Kluge, KA Flippo, et al. Increased laser-accelerated proton energies via direct laser-light-pressure acceleration of electrons in microcone targetsa). *Physics of Plasmas (1994-present)*, 18(5):056710, 2011.

[130] M Passoni, A Zani, A Sgattoni, et al. Energetic ions at moderate laser intensities using foam-based multi-layered targets. *Plasma Physics and Controlled Fusion*, 56(4):045001, 2014.

[131] J Limpouch, J Psikal, AA Andreev, K Yu Platonov, and S Kawata. Enhanced laser ion acceleration from mass-limited targets. *Laser and Particle Beams*, 26(02):225–234, 2008.

[132] T Sokollik, Tim Paasch-Colberg, K Gorling, et al. Laser-driven ion acceleration using isolated mass-limited spheres. *New Journal of Physics*, 12(11):113013, 2010.

[133] Thomas Kluge, W Enghardt, SD Kraft, et al. Enhanced laser ion acceleration from mass-limited foils. *Physics of Plasmas (1994-present)*, 17(12):123103, 2010.

[134] Andrea Macchi, Federica Cattani, Tatiana V Liseykina, and Fulvio Cornolti. Laser acceleration of ion bunches at the front surface of overdense plasmas. *Physical review letters*, 94(16):165003, 2005.

[135] JFL Simmons and CR McInnes. Was marx right? or how efficient are laser driven interstellar spacecraft? *American journal of physics*, 61(3):205–207, 1993.

[136] I Jong Kim, Ki Hong Pae, Chul Min Kim, et al. Transition of proton energy scaling using an ultrathin target irradiated by linearly polarized femtosecond laser pulses. *Physical review letters*, 111(16):165003, 2013.

[137] Andreas Henig, Daniel Kiefer, K Markey, et al. Enhanced laser-driven ion acceleration in the relativistic transparency regime. *Physical review letters*, 103(4):045002, 2009.

[138] IW Choi, I J Kim, KH Pae, et al. Simultaneous generation of ions and high-order harmonics from thin conjugated polymer foil irradiated with ultrahigh contrast laser. *Applied Physics Letters*, 99(18):181501, 2011.

[139] I Jong Kim, Ki Hong Pae, Chul Min Kim, et al. Transition of proton energy scaling using an ultrathin target irradiated by linearly polarized femtosecond laser pulses. *Physical review letters*, 111(16):165003, 2013.

[140] Luís O Silva, Michael Marti, Jonathan R Davies, et al. Proton shock acceleration in laser-plasma interactions. *Physical review letters*, 92(1):015002, 2004.

[141] MS Wei, SPD Mangles, Z Najmudin, et al. Ion acceleration by collisionless shocks in high-intensity-laser–underdense-plasma interaction. *Physical review letters*, 93(15):155003, 2004.

[142] Dan Haberberger, Sergei Tochitsky, Frederico Fiuza, et al. Collisionless shocks in laser-produced plasma generate monoenergetic high-energy proton beams. *Nature Physics*, 8(1):95–99, 2012.

[143] L Yin, BJ Albright, KJ Bowers, et al. Three-dimensional dynamics of breakout afterburner ion acceleration using high-contrast short-pulse laser and nanoscale targets. *Physical review letters*, 107(4):045003, 2011.

[144] BJ Albright, L Yin, Kevin J Bowers, et al. Relativistic buneman instability in the laser breakout afterburner. *Physics of Plasmas (1994-present)*, 14(9):094502, 2007.

[145] L Yin, BJ Albright, BM Hegelich, et al. Monoenergetic and gev ion acceleration from the laser breakout afterburner using ultrathin targetsa). *Physics of Plasmas (1994-present)*, 14(5):056706, 2007.

[146] J Fuchs, Patrizio Antici, E dâĂŹHumieres, et al. Laser-driven proton scaling laws and new paths towards energy increase. *Nature physics*, 2(1):48–54, 2006.

[147] Lynne Robson, PT Simpson, Robert J Clarke, et al. Scaling of proton acceleration driven by petawatt-laser–plasma interactions. *Nature physics*, 3(1):58–62, 2007.

[148] P Mora. Plasma expansion into a vacuum. *Physical Review Letters*, 90(18):185002, 2003.

[149] Patrizio Antici, J Fuchs, E dâĂŹHumières, et al. Energetic protons generated by ultrahigh contrast laser pulses interacting with ultrathin targets. *Physics of Plasmas (1994-present)*, 14(3):030701, 2007.

[150] P Mora. Thin-foil expansion into a vacuum. *Physical Review E*, 72(5):056401, 2005.

[151] M Passoni and M Lontano. One-dimensional model of the electrostatic ion acceleration in the ultraintense laser–solid interaction. *Laser and Particle Beams*, 22(02):163–169, 2004.

[152] Maurizio Lontano and Matteo Passoni. Electrostatic field distribution at the sharp interface between high density matter and vacuum. *Physics of Plasmas (1994-present)*, 13(4):042102, 2006.

[153] S Kar, M Borghesi, SV Bulanov, et al. Plasma jets driven by ultraintense-laser interaction with thin foils. *Physical review letters*, 100(22):225004, 2008.

[154] K Quinn, PA Wilson, CA Cecchetti, et al. Laser-driven ultrafast field propagation on solid surfaces. *Physical review letters*, 102(19):194801, 2009.

[155] M Passoni and M Lontano. Theory of light-ion acceleration driven by a strong charge separation. *Physical review letters*, 101(11):115001, 2008.

[156] Matteo Passoni, Luca Bertagna, and Alessandro Zani. Target normal sheath acceleration: theory, comparison with experiments and future perspectives. *New Journal of Physics*, 12(4):045012, 2010.

[157] BJ Albright, L Yin, BM Hegelich, et al. Theory of laser acceleration of light-ion beams from interaction of ultrahigh-intensity lasers with layered targets. *Physical review letters*, 97(11):115002, 2006.

[158] AP L Robinson, AR Bell, and RJ Kingham. Effect of target composition on proton energy spectra in ultraintense laser-solid interactions. *Physical review letters*, 96(3):035005, 2006.

[159] Charles K Birdsall and A Bruce Langdon. *Plasma physics via computer simulation*. CRC Press, 2004.

[160] Anna Grassi, Luca Fedeli, Andrea Sgattoni, and Andrea Macchi. Vlasov simulation of laser-driven shock acceleration and ion turbulence. *Plasma Physics and Controlled Fusion*, 58(3):034021, 2016.

[161] Mickaël Melzani, Christophe Winisdoerffer, Rolf Walder, et al. Apar-t: code, validation, and physical interpretation of particle-in-cell results. *Astronomy & Astrophysics*, 558:A133, 2013.

[162] Andrea Sgattoni, Luca Fedeli, Stefano Sinigardi, et al. Optimising piccante–an open source particle-in-cell code for advanced simulations on tier-0 systems. *Preparatory PRACE white paper (arXiv:1503.02464)*, 2015.

[163] T Ceccotti, A Lévy, H Popescu, et al. Proton acceleration with high-intensity ultrahigh-contrast laser pulses. *Physical review letters*, 99(18):185002, 2007.

[164] M Borghesi and U Schramm. Summary of working group 2: Ion beams from plasmas. *Nuclear Instruments and Methods in Physics Research Section A: Accelerators, Spectrometers, Detectors and Associated Equipment*, 2016.

[165] A Zani, D Dellasega, V Russo, and M Passoni. Ultra-low density carbon foams produced by pulsed laser deposition. *Carbon*, 56:358–365, 2013.

[166] Yun-Qian Cui, Wei-Min Wang, Zheng-Ming Sheng, Yu-Tong Li, and Jie Zhang. Laser absorption and hot electron temperature scalings in laserâĂŞplasma interactions. *Plasma Physics and Controlled Fusion*, 55(8):085008, 2013.

[167] T Kluge, T Cowan, A Debus, et al. Electron temperature scaling in laser interaction with solids. *Physical review letters*, 107(20):205003, 2011.

[168] Alessandro Flacco, François Sylla, Mina Veltcheva, et al. Dependence on pulse duration and foil thickness in high-contrast-laser proton acceleration. *Physical Review E*, 81(3):036405, 2010.

[169] DB Zou, HB Zhuo, XH Yang, et al. Enhanced target normal sheath acceleration based on the laser relativistic self-focusing. *Physics of Plasmas (1994-present)*, 21(6):063103, 2014.

[170] Stepan S Bulanov, Valery Yu Bychenkov, Vladimir Chvykov, et al. Generation of gev protons from 1 pw laser interaction with near critical density targets. *Physics of Plasmas (1994-present)*, 17(4):043105, 2010.

[171] Yan Tay, Donghoon Kuk, Howard Milchberg, and Ki-Yong Kim. Interaction of high density, thin, gas jets with ultrashort laser pulses at 1 khz repetition rates. In *APS March Meeting Abstracts*, 2016.

[172] Michael H Helle, Daniel F Gordon, Dmitri Kaganovich, Anthony Zingale, and Antonio Ting. Accelerated protons from near critical density gaseous targets. In *ADVANCED ACCELERATOR CONCEPTS 2014: 16th Advanced Accelerator Concepts Workshop*, volume 1777, page 090004. AIP Publishing, 2016.

[173] IN Tsymbalov, KA Ivanov, SA Shulyapov, et al. Laser energy absorption and hot electrons generation in near-critical plasma at relativistic intensities. In *Laser Optics (LO), 2016 International Conference*, pages R5–4. IEEE, 2016.

[174] Ruowen Fu, Bo Zheng, Jie Liu, et al. The fabrication and characterization of carbon aerogels by gelation and supercritical drying in isopropanol. *Advanced Functional Materials*, 13(7):558–562, 2003.

[175] Wenjun Ma, Li Song, Rong Yang, et al. Directly synthesized strong, highly conducting, transparent single-walled carbon nanotube films. *Nano Letters*, 7(8):2307–2311, 2007.

[176] I Prencipe, A Sgattoni, D Dellasega, et al. Development of foam-based layered targets for laser-driven ion beam production. *Plasma Physics and Controlled Fusion*, 58(3):034019, 2016.

[177] A. Pazzaglia. Produzione e caratterizzazione di bersagli multistrato per l'accelerazione di ioni mediante laser superintensi. 2016.

[178] Tae Jun Yu, Seong Ku Lee, Jae Hee Sung, et al. Generation of high-contrast, 30 fs, 1.5 pw laser pulses from chirped-pulse amplification ti: sapphire laser. *Optics express*, 20(10):10807–10815, 2012.

[179] Tae Moon Jeong and Jongmin Lee. Femtosecond petawatt laser. *Annalen der Physik*, 526(3-4):157–172, 2014.

[180] D Jung, B J Albright, L Yin, et al. Beam profiles of proton and carbon ions in the relativistic transparency regime. *New Journal of Physics*, 15(12):123035, 2013.

[181] APL Robinson, RMGM Trines, J Polz, and M Kaluza. Absorption of circularly polarized laser pulses in near-critical plasmas. *Plasma Physics and Controlled Fusion*, 53(6):065019, 2011.

[182] CGR Geddes, Cs Toth, J Van Tilborg, et al. High-quality electron beams from a laser wakefield accelerator using plasma-channel guiding. *Nature*, 431(7008):538–541, 2004.

[183] M Passoni, A Sgattoni, I Prencipe, et al. Toward high-energy laser-driven ion beams: Nanostructured double-layer targets. *Physical Review Accelerators and Beams*, 19(6):061301, 2016.

Ringraziamenti

"Nella carbonara non ci va la cipolla" A. Einstein

Mi accorgo di aver le scatole così piene di questa tesi che persino scrivere queste ultime righe di ringraziamenti mi causa una spiacevole sensazione di fastidio che potrebbe essere riportata nella sezione "effetti collaterali" di un bugiardino di qualche farmaco. D'altra parte è noto che la sezione ringraziamenti è la sezione più letta di ogni tesi quindi non inserirla eliminerebbe una buona fetta di miei potenziali lettori.
Per prima cosa devo ringraziare Matteo, in primo luogo è perchè è il mio capo in secondo luogo perchè è riuscito a sopportarmi per altri tre anni il che non è per nulla un risultato da poco. Lo ringrazio soprattutto per il supporto umano quando ne avevo bisogno, supporto che non era dovuto visto che non è nell'insieme di compiti per i quali è pagato un professore del Politecnico.
Il secondo in lista è sicuramente il buon Luca Fedeli. Non è un'esagerazione dire che senza la sua presenza il mio dottorato non si sarebbe concluso positivamente come credo si concluderà. [1]
Ringrazio i miei genitori per avermi dato la possibilità di completare i

---

[1] Questa tesi è stata interamente pagata dalla sezione "troll del PIDDI" del Partito Democratico.

miei studi strappando le mie braccia all'agricoltura (braccia che tuttora reclama). Nella lista c'è anche mia sorella Caterina che è la prova che non tutti i figli sono pigri come me. Di contro lei dovrebbe ringraziarmi dal momento che se ora gioca in seria A di pallavolo è solamente grazie ai miei insegnamenti.
Un grazie è dovuto anche a tutti i colleghi del CESNEF, meglio noto come dipartimento d'ingegneria nucleare Lorenzo Cialfi (mettete like alla pagina di facebook) credo che nella futura vita lavorativa sarà difficile trovare persone altrettanto valide e allo stesso tempo ignoranti. Un grazie a Edo Bezossi che è stato visto comprando in piazzale Aspromonte e ora è già stato arrestato. Poi dovrà dimostrare ... intanto è in galera.
Altro grazie a tutto il gruppo di "Sabbabbato", vi voglio bene (tranne che a stefo) nonostante la vostra sovrabbondanza di melanina. Quando mi dottorerò "si spoccia" (scusa Lucia ma dovevo).
Siamo arrivati a te Fede. Come diceva Gesù o forse Ghandi "gli amici sono i parenti che ti scegli". Bhe, la frase parla da sola e fa capire molto bene che non sono per niente in grado di far scelte oculate. Come scrissi sul diario alla mia amichetta ai tempi delle medie "spero che rimarremo in contatto dopo gli esami, TVUKDB" (mai più vista d'allora).
L'ultimo spazio nei ringraziamenti è riservato a te Giulia perchè ... no ma veramente ti aspetti che scriva qualcosa? l'hai letta la prima pagina della tesi? E' dedicata a te, accontentati.

Scherzavo, come nella tesi magistrale l'ultimo spazio è dedicato a te Lorenzo del futuro. Non so se avrai inseguito i tuoi sogni, diventando la prima persona ad aver fatto il giro del Mondo in triciclo, quello di cui son certo è che non sarai mai così fico come sei ora. [2]

---

[2] Dispongo di una meravigliosa dimostrazione dell'ultimo teorema di Fermat, che non può essere contenuta nel margine troppo stretto della pagina